

Geostatistical Analysis of Permeability Data



Georgousakis Konstantinos

Petroleum Engineering M.Sc. Course
School of Mineral Resources Engineering
Technical University of Crete
Advisor : Prof. Dionissios T. Hristopulos

This dissertation is submitted for the degree of
Master of Science

January 2017

“Determining the proper parameters of the variogram is more like a form of art. This is why only a few people get involved with geostatistics.”

This thesis is dedicated to those who persist...

Acknowledgements

First and foremost I would like to express my gratitude to my advisor Prof. Dionissios Hristopoulos for the guidance he offered to me all throughout the writing of this thesis. His advice was always clarifying and welcoming. His willingness and cooperation proved priceless in this demanding task. In addition, I would like to thank all the professors participating in this Master Course. Their knowledge and mentoring provided me with a solid theoretical background in order to undertake this project.

Also, a special thanks goes to Vasiliki Agou for her useful advice on certain theoretical issues, as well as her priceless guidance concerning the software required for carrying out this thesis. Furthermore, I wish to thank Assoc. Prof. Tom Manzocchi of the UCD Earth Institute, as well as Mr Kees C.R. Geel of the TNO Earth for their information about the data required for this thesis and with which, a major step ahead was achieved.

Besides those, I would like to thank my friends for their continuous support, as well as my fellow students for all the help they have offered me so far and for making this academic year so much more enjoyable.

Last but not least, I want to express my sincerest gratitude to my family for all their support and understanding throughout this difficult and challenging year.

Technical University of Crete, 2017
Konstantinos Georgousakis

Abstract

Properties such as porosity and permeability are of utmost significance in petroleum industry. They are important parameters for both reservoir engineering and reservoir modelling, since they constitute the basis upon which hydrocarbon reserves, as well as hydrocarbon flow characteristics are determined. For that reason, accurate estimation of these properties has been the subject of continuous studies.

For the purposes of this thesis, the porosity and permeability data provided by the 10th SPE benchmark reservoir model were used. This model is part of the PUNQ Complex Model and is a highly heterogeneous model, consisting of two parts: A relatively permeable Tarbert formation on top and an Upper Ness formation at the bottom. The latter comprises of permeable anastomosed channels laid on a non-permeable background. The data were analysed using visualization, statistical and geostatistical techniques, in order to investigate the statistical properties and to subsequently quantify and evaluate their spatial correlation and variability.

The exploratory analysis was carried out using classical statistics (e.g., histograms, statistical moments, distribution fitting and scatter plots). However, the main results were derived using geostatistical methods. Geostatistical analysis included the calculation of various variograms (i.e., directional, anisotropic, omnidirectional and 3D variograms), and their subsequent fitting with appropriate theoretical variogram models. In addition to this analysis, an upscaling of the reservoir model was performed by implementing the Simplified Renormalization method to both porosity and permeability data.

Various conclusions were drawn from this project concerning the behaviour and spatial correlation of the reservoir, as well as the general implementation of the geostatistical methods. The most important outcome was the confirmation of the high heterogeneity and anisotropy characterizing the entire reservoir model. An equally significant observation was that results depend greatly on the number and locations of data included. More specifically, considering more data across the horizontal plane increases the interpretable information of variogram analysis, while considering more data along the vertical direction increases the variability. Finally, upscaling leads to coarse-grained versions of the reservoir model; such

reduced dimensionality models should be further evaluated by means of subsequent flow simulation.

Table of contents

List of figures	xi
List of tables	xv
1 Introduction	1
1.1 Objectives	4
1.2 Thesis Outline	4
1.3 Basic Concepts	4
1.3.1 Permeability	4
1.3.2 Porosity	5
1.3.3 Stochastic Processes	6
1.3.4 Geostatistics	6
2 Geostatistical Methods	9
2.1 Exploratory Data Analysis	9
2.1.1 Probability Density Function	10
2.1.2 Moments	10
2.1.3 Probability Distributions	13
2.2 Spatial Modelling	17
2.2.1 Experimental Variogram	20
2.2.2 Theoretical Variogram Model	23
2.3 Kriging	24
2.3.1 Simple Kriging	25
2.3.2 Ordinary Kriging	26
2.3.3 Universal Kriging	27
2.4 Upscaling	29
2.4.1 Simplified Renormalization	31

3	Data Description	37
3.1	Tenth SPE Model	37
3.1.1	PUNQ Project	38
3.1.2	Tarbert Formation	39
3.1.3	Upper Ness Formation	39
3.2	Visualisation of Data	40
3.2.1	Tarbert Formation	40
3.2.2	Upper Ness Formation	41
3.3	Exploratory Data Analysis	41
3.3.1	Tarbert Formation	42
3.3.2	Upper Ness Formation	45
4	Geostatistical Analysis	53
4.1	Variogram Analysis	53
4.1.1	Experimental Variogram	53
4.1.2	Theoretical Variogram Model	57
4.2	Upscaling	60
4.2.1	Tarbert Formation	60
4.2.2	Upper Ness Formation	66
5	Conclusions & Discussion	111
	References	115
	Appendix A Calculation Algorithms	123

List of figures

2.1	Indicative variogram	19
2.2	Variogram with scatterplots	32
2.3	Experimental variograms	33
2.4	Hole effect types	34
2.5	Theoretical variogram models	35
2.6	Simplified Renormalization	36
3.1	3D representation	41
3.2	Tarbert formation–layer 1	42
3.3	Tarbert formation–layer 17	43
3.4	Upper Ness formation–layer 1	44
3.5	Upper Ness formation–layer 20	45
3.6	Upper Ness formation–layer 35	46
3.7	Upper Ness formation–layer 50	47
3.8	Tarbert formation data distributions	48
3.9	Tarbert formation scatter plots	49
3.10	Upper Ness formation data distributions	50
3.11	Upper Ness formation scatter plots	51
4.1	Formation partition	55
4.2	Number of subsamples	72
4.3	Number of bins	72
4.4	Tarbert Phi marginal variograms	73
4.5	Tarbert PermX marginal variograms	73
4.6	Tarbert PermY marginal variograms	74
4.7	Tarbert PermZ marginal variograms	74
4.8	Tarbert formation anisotropic variograms–layer 1	75
4.9	Tarbert formation anisotropic variograms–layer 10	76

4.10	Tarbert formation anisotropic variograms–layer 20	77
4.11	Tarbert formation anisotropic variograms–layer 30	78
4.12	Tarbert formation anisotropic variograms–layer 35	79
4.13	Tarbert formation omnidirectionl variograms–layer 1	80
4.14	Tarbert formation omnidirectionl variograms–layer 10	80
4.15	Tarbert formation omnidirectionl variograms–layer 20	81
4.16	Tarbert formation omnidirectionl variograms–layer 30	81
4.17	Tarbert formation omnidirectionl variograms–layer 35	82
4.18	Tarbert formation 3D variograms–Subvolume 1	83
4.19	Tarbert formation 3D variograms–Subvolume 2	83
4.20	Tarbert formation 3D variograms–Subvolume 3	84
4.21	Tarbert formation 3D variograms–Subvolume 4	84
4.22	Upper Ness Phi marginal variograms	85
4.23	Upper Ness PermX marginal variograms	85
4.24	Upper Ness PermY marginal variograms	86
4.25	Upper Ness PermZ marginal variograms	86
4.26	Upper Ness formation anisotropic variograms–layer 1	87
4.27	Upper Ness formation anisotropic variograms–layer 10	88
4.28	Upper Ness formation anisotropic variograms–layer 20	89
4.29	Upper Ness formation anisotropic variograms–layer 30	90
4.30	Upper Ness formation anisotropic variograms–layer 40	91
4.31	Upper Ness formation anisotropic variograms–layer 50	92
4.32	Upper Ness formation omnidirectionl variograms–layer 1	93
4.33	Upper Ness formation omnidirectionl variograms–layer 10	93
4.34	Upper Ness formation omnidirectionl variograms–layer 20	94
4.35	Upper Ness formation omnidirectionl variograms–layer 30	94
4.36	Upper Ness formation omnidirectionl variograms–layer 40	95
4.37	Upper Ness formation omnidirectionl variograms–layer 50	95
4.38	Upper Ness formation 3D variograms–Subvolume 1	96
4.39	Upper Ness formation 3D variograms–Subvolume 2	96
4.40	Upper Ness formation 3D variograms–Subvolume 3	97
4.41	Upper Ness formation 3D variograms–Subvolume 4	97
4.42	Different fitted variogram models	98
4.43	Tarbert Formation fitted variograms	99
4.44	Upper Ness Formation fitted variograms	100
4.45	Tarbert formation 1 st iteration upscaling–3D images	101

4.46	Tarbert formation 1 st iteration upscaling–distributions	101
4.47	Tarbert formation 2 nd iteration upscaling–3D images	102
4.48	Tarbert formation 2 nd iteration upscaling–distributions	102
4.49	Tarbert formation 3 rd iteration upscaling–3D images	103
4.50	Tarbert formation 3 rd iteration upscaling–distributions	103
4.51	Tarbert formation 4 th iteration upscaling–3D images	104
4.52	Tarbert formation 4 th iteration upscaling–distributions	104
4.53	Tarbert formation 5 th iteration upscaling–3D images	105
4.54	Tarbert formation 5 th iteration upscaling–distributions	105
4.55	Upper Ness formation 1 st iteration upscaling–3D images	106
4.56	Upper Ness formation 1 st iteration upscaling–distributions	106
4.57	Upper Ness formation 2 nd iteration upscaling–3D images	107
4.58	Upper Ness formation 2 nd iteration upscaling–distributions	107
4.59	Upper Ness formation 3 rd iteration upscaling–3D images	108
4.60	Upper Ness formation 3 rd iteration upscaling–distributions	108
4.61	Upper Ness formation 4 th iteration upscaling–3D images	109
4.62	Upper Ness formation 4 th iteration upscaling–distributions	109
4.63	Upper Ness formation 5 th iteration upscaling–3D images	110
4.64	Upper Ness formation 5 th iteration upscaling–distributions	110

List of tables

3.1	Tarbert formation statistical parameters. Porosity appears in decimal representation and permeability is expressed in miliDarcies (mD).	44
3.2	Tarbert formation distribution parameters. The parentheses describe an alternative distribution fit. Porosity appears in decimal representation, permeability is measured in miliDarcies (mD) and data are analysed after applying logarithm.	45
3.3	Upper Ness formation statistical parameters. Porosity appears in decimal representation and permeability is expressed in miliDarcies (mD).	47
3.4	Upper Ness formation distribution parameters. Porosity appears in decimal representation, permeability is measured in miliDarcies (mD) and data are analysed after applying logarithm.	48
4.1	Summarizing table of R^2 values derived from the fitting of the 3D variogram of first Subvolume to a theoretical model, for the Tarbert formation.	58
4.2	Variogram modelling parameters of the first Subvolume of porosity and permeability for Tarbert formation.	58
4.3	Summarizing table of R^2 values derived from the fitting of the 3D variogram of the first Subvolume to a theoretical model, for the Upper Ness formation.	59
4.4	Variogram modelling parameters of the first Subvolume of porosity and permeability for Upper Ness formation.	59
4.5	Tarbert formation statistical parameters after the first iteration of upscaling. Porosity appears in decimal representation and permeability is expressed in miliDarcies (mD).	61
4.6	Tarbert formation distribution parameters after the first iteration of upscaling. The parentheses describe an alternative distribution fit. Porosity appears in decimal representation, permeability is measured in miliDarcies (mD) and data are analysed after applying logarithm.	61

4.7	Tarbert formation statistical parameters after the second iteration of upscaling. Porosity appears in decimal representation and permeability is expressed in miliDarcies (mD).	62
4.8	Tarbert formation distribution parameters after the second iteration of upscaling. The parentheses describe an alternative distribution fit. Porosity appears in decimal representation, permeability is measured in miliDarcies (mD) and data are analysed after applying logarithm.	62
4.9	Tarbert formation statistical parameters after the third iteration of upscaling. Porosity appears in decimal representation and permeability is expressed in miliDarcies (mD).	62
4.10	Tarbert formation distribution parameters after the third iteration of upscaling. The parentheses describe an alternative distribution fit. Porosity appears in decimal representation, permeability is measured in miliDarcies (mD) and data are analysed after applying logarithm.	63
4.11	Tarbert formation statistical parameters after the fourth iteration of upscaling. Porosity appears in decimal representation and permeability is expressed in miliDarcies (mD).	63
4.12	Tarbert formation distribution parameters after the fourth iteration of upscaling. The parentheses describe an alternative distribution fit. Porosity appears in decimal representation, permeability is measured in miliDarcies (mD) and data are analysed after applying logarithm.	63
4.13	Tarbert formation statistical parameters after the fifth iteration of upscaling. Porosity appears in decimal representation and permeability is expressed in miliDarcies (mD).	64
4.14	Tarbert formation distribution parameters after the fifth iteration of upscaling. The parentheses describe an alternative distribution fit. Porosity appears in decimal representation, permeability is measured in miliDarcies (mD) and data are analysed after applying logarithm.	64
4.15	Tarbert formation block values after the sixth iteration of upscaling. Porosity appears in decimal representation and permeability is expressed in miliDarcies (mD).	65
4.16	Tarbert formation block values after the seventh iteration of upscaling. Porosity appears in decimal representation and permeability is expressed in miliDarcies (mD).	65

4.17	Tarbert formation equivalent values after the eighth iteration of upscaling, combined with Wiener bounds. Porosity appears in decimal representation and permeability is expressed in miliDarcies (mD).	65
4.18	Upper Ness formation statistical parameters after the first iteration of upscaling. Porosity appears in decimal representation and permeability is expressed in miliDarcies (mD).	66
4.19	Upper Ness formation distribution parameters after the first iteration of upscaling. Porosity appears in decimal representation, permeability is measured in miliDarcies (mD) and data are analysed after applying logarithm.	66
4.20	Upper Ness formation statistical parameters after the second iteration of upscaling. Porosity appears in decimal representation and permeability is expressed in miliDarcies (mD).	67
4.21	Upper Ness formation distribution parameters after the second iteration of upscaling. Porosity appears in decimal representation, permeability is measured in miliDarcies (mD) and data are analysed after applying logarithm.	67
4.22	Upper Ness formation statistical parameters after the third iteration of upscaling. Porosity appears in decimal representation and permeability is expressed in miliDarcies (mD).	68
4.23	Upper Ness formation distribution parameters after the third iteration of upscaling. The parentheses describe an alternative distribution fit. Porosity appears in decimal representation, permeability is measured in miliDarcies (mD) and data are analysed after applying logarithm.	68
4.24	Upper Ness formation statistical parameters after the fourth iteration of upscaling. Porosity appears in decimal representation and permeability is expressed in miliDarcies (mD).	68
4.25	Upper Ness formation distribution parameters after the fourth iteration of upscaling. The parentheses describe an alternative distribution fit. Porosity appears in decimal representation, permeability is measured in miliDarcies (mD) and data are analysed after applying logarithm.	69
4.26	Upper Ness formation statistical parameters after the fifth iteration of upscaling. Porosity appears in decimal representation and permeability is expressed in miliDarcies (mD).	69
4.27	Upper Ness formation distribution parameters after the fifth iteration of upscaling. Porosity appears in decimal representation, permeability is measured in miliDarcies (mD) and data are analysed after applying logarithm.	70

4.28	Upper Ness formation block values after the sixth iteration of upscaling. Porosity appears in decimal representation and permeability is expressed in miliDarcies (mD).	70
4.29	Upper Ness formation block values after the seventh iteration of upscaling. Porosity appears in decimal representation and permeability is expressed in miliDarcies (mD).	70
4.30	Upper Ness formation equivalent values after the eighth iteration of upscaling, combined with Wiener bounds. Porosity appears in decimal representation and permeability is expressed in miliDarcies (mD).	71

Chapter 1

Introduction

One of the main objectives of the O&G industry is acquiring an accurate image of the underground reservoir, which includes the geometry, geology and formation attributes. The most significant parameters for the reservoir engineer are porosity and permeability and for this reason, their determination across the whole volume of the reservoir is the objective of continuous studies. Porosity and permeability are determined from core samples and lab measurements using known correlations and are subsequently used in order to model unsampled location values, by means of averaging and interpolation methods. To correctly extrapolate these values, the depositional environment has to be identified, utilize analog datasets and ultimately extrapolate the statistical distributions. Prediction of rock properties at unsampled locations is a difficult task for which, a number of concepts and assumptions is necessary (Pyrzcz and Deutsch, 2014).

Permeability is one of the most important parameters affecting reservoir performance (Ayan et al., 1994). A number of estimation methods for permeability exist, taking into consideration rock type and petrophysical properties like grain size, surface area and pore size (PetroWiki, 2015a), with one of the most fundamental methods being Darcy's Law. The Kozeny–Carman equation relies on the pressure drop of fluids passing through a medium and it constitutes the basis to other estimation models. Models based on grain size include Krumbein and Monk's equation, Berg's model and Van Baaren's model. Methods based on mineralogy are included in the studies of Herron, Panda and Lake, Bryant et al. and Cade et al. Based on surface area and water saturation, existing methods include Granberry and Keelan's chart, Timur's model, Dual Water model, Kukul and Simons equation for low-porosity systems and Nuclear Magnetic Resonance methods. Based on pore dimension, the equations of Swanson, Winland, Pittman, Katz and Thompson exist, which incorporate the relationship of permeability with capillary pressures and pore size, as well as the Flow

Zone Indicator suggested by Amaefule and Altunbay (PetroWiki, 2015b). An additional method utilizing the capillary pressures is the Leverett J-function (Leverett, 1941).

Few geologic processes are fully understood in order to allow the use of deterministic methods (Isaaks and Srivastava, 1989), thus making application of stochastic processes necessary. As Kamali et al. (2013) point out, there are several estimation methods, generally classified into classical and geostatistical. Classical methods utilize classical statistics but most of them do not exploit the spatial information in earth science datasets (Isaaks and Srivastava, 1989). On the other hand, geostatistical methods use the spatial structure of data in the environment to produce estimations. Three dimensional models is the best solution for combining all existing data. The use of such models allows for a more realistic treatment of the dependencies of different parameters and additionally, provides information on the spatial variability of uncertainty (Kamali et al., 2013).

Geostatistical methods are useful tools, which utilize the spatial correlation of data in order to produce complete results that can be further used in other simulation procedures. Numerous studies have been made applying geostatistical methods for the analysis of permeability data and modelling of fluid flow. Jennings et al. (2000) used geostatistics to study the permeability of hydrocarbon rich, heterogeneous Permian dolomitized shallow-water platform Carbonate Outcrops in Texas. A permeability map of the field is valuable, since it is used to optimize further field development (Moore and Wade, 2013). Recently, Amanipoor (2013) used petrophysical data, including permeability, to prepare the 3D model for the Bangestan oil reservoir in southwest of Iran. One of their notable conclusions is that the strong similarity between actual and estimated data confirms that geostatistical methods are appropriate tools for 3D modeling of petrophysical parameters in oil and gas reservoirs.

The study of Makse et al. (1996) presented a numerical model on permeability pattern formation in grain flow in wind-blown or fluvial sands. As they point out, efficient hydrocarbon recovery is influenced by the understanding of such spatial patterns. Related to that, Saemi et al. (2007) utilized artificial neural networks combined with genetic algorithm to estimate the permeability of the South Pars gas field in Persian Gulf.

Moving on to other methods, Oliver (1990) presented the results of averaging processes in permeability estimation using weighted averages of permeability and based on well-test data. Noetinger et al. (1996) proposed an averaging method relating the permeability provided by well test interpretation with the permeability map around the well, for 3D heterogeneous reservoirs. Later on, Babadagli (2006) estimated effective permeability of fractally distributed 2D fields using different averaging techniques, with the most accurate among his results being the geometric mean and power averaging techniques.

Bryant et al. (1993) worked on network models in order to replicate the microstructure of porous media and use these models to estimate and compare permeability values, as well as their spatial correlation. Ioannidis et al. (1996) conducted statistical analysis of porous microstructure in order to estimate reservoir permeability and derived an empirical equation as a function of porosity and correlation scale.

Ayan et al. (1994) examined the effects of anisotropy and heterogeneity on permeability of Triassic Sherwood sandstone reservoir. Sweet et al. (1996) presented the study of a heterogeneous low-permeability gas reservoir in Hyde field in southern North Sea, which included geostatistical, as well as upscaling techniques. Renard and de Marsily (1997) presented a review of equivalent permeability calculation methods, making a distinction between effective and block permeability estimation techniques, which can be further applied in upscaling procedures. Furthermore, the announcement of the 10th SPE Comparative Solution Project was an open invitation for permeability estimation studies of a highly heterogeneous model applying upscaling techniques. The projects that were turned in, as well as their results were collected and presented in the report of Christie and Blunt (2001). Moreover, Masihi et al. (2016) introduced methods to estimate the effective permeability of heterogeneous porous media based on percolation concepts, to be used for upscaling purposes. It is also significant to notice their classification of effective permeability estimation methods in deterministic versus stochastic, analytical versus numerical, exact versus approximate and local versus non-local methods.

Naturally, permeability estimation is not only useful in oil and gas exploitation but also in water resources applications. Desbarats (1987) attempted a numerical estimation of effective permeability in sand-shale formations, considering the cases of both spatially correlated and uncorrelated permeabilities. More recent studies followed, like Butler (2005) who examined three classes of methods for estimating hydraulic conductivity, a parameter which depends on permeability and the effect of its spatial variation in saturated flow systems. Torabi et al. (2008) demonstrated a method to estimate permeability on microscale and to map out permeability variations in deformation bands and similar geological structures. Mariethoz et al. (2010) proposed a direct sampling from a training image method to perform multiple-point geostatistical simulations to continuous variables. Last but not least, Dell'Arciprete et al. (2011) compared three different pixel-based geostatistical simulation methods commonly used for water and oil reservoir modelling.

1.1 Objectives

For the purposes of this thesis, geostatistical methods are implemented in order to understand and quantify the spatial structure of permeability and porosity data provided by the 10th SPE benchmark reservoir model. The first objective of this thesis is to properly visualize the provided data, analyse them from a statistical perspective and make a distinction between the different groups coexisting in the model. Another objective is to apply geostatistical methods like variography on different groups of data, in order to study their spatial correlation and after that, to treat the data accordingly, so as to prepare them for subsequent spatial modelling. The final objective is to carry out an upscaling of the model, in order to reduce the resolution of the information and study the behaviour of the model for each intermediate step.

1.2 Thesis Outline

The thesis is organized in the following manner. In the present Chapter, a summary of the available literature on permeability estimation is included, as well as a description of the basic concepts of the main properties and methods used in this study. In Chapter 2, a detailed description of the utilized statistical and geostatistical methods is presented. Subsequently, in Chapter 3, the data are described using visualization and statistical techniques and the results are presented in form of Figures and Tables. In Chapter 4, the geostatistical analysis is carried out, which constitutes of the experimental variogram analysis for various data groups of the model and the subsequent fitting of theoretical variogram models to the experimental data. Furthermore, upscaling procedures are applied to the model and the results are accompanied by the proper visualization and statistical analysis. All results are properly presented in form of Figures and Tables. Chapter 5 includes a discussion of the results, as well as the derived conclusions of this study. Finally, the algorithms utilized for the application of the various methods are found in Appendix A.

1.3 Basic Concepts

1.3.1 Permeability

Permeability in earth sciences is defined as a physical quantity which characterizes the medium, usually rocks or unconsolidated material, and affects the velocity of the fluids passing through it. This parameter is important in determining the flow characteristics of hydrocarbons in oil and gas reservoirs. Permeability is also an indicator of the pore throat

dimensions. It can be generally calculated in the lab using various solutions to the diffusion equation for unsteady flow conditions or as it is mostly known by applying Darcy's Law under steady state conditions (Bear, 1972). Also it can be measured by means of well logging procedures.

The factors affecting permeability are pore size, pore throat geometry and porosity. It is denoted by the letter k and is measured in m^2 (SI units), Darcy (D) or more commonly millidarcy (mD) (oilfield units). Permeability is neither a scalar, nor a vector. Pressure is applied triaxially and for each direction permeability can be measured, leading to a 3-by-3 symmetric tensor of second rank (Liakopoulos, 1965), which is necessary when modelling permeability in anisotropic media (Bear, 1972).

There are three distinct categories, absolute, effective and relative permeability. Absolute permeability refers to single phase fluid flow. Effective permeability characterizes the flow capacity of the matrix to a particular fluid when two or more phases are present. Relative permeability expresses the permeability of a fluid in multiphase flow over the absolute permeability of the medium and it can change with fluid saturation. Several models have been developed for relative permeability modelling, including the models of Brooks–Correy, Heterogeneous Rock, Chierici, Hysteresis, Carman–Kozeny, Network and Three–phase Relative Permeability models, as well as Honarpour et al. and Ibrahim correlations (PetroWiki, 2016c).

1.3.2 Porosity

Porosity or void fraction is determined as the percentage of the total bulk formation volume that can be occupied by fluids. It is a measure of the void spaces in the porous medium. Porosity does not provide information about the connectivity of the pores. It can be determined with lab measurements mostly or with well logging methods. The factors affecting porosity are mainly grain size and sorting, burial depth and degree of compaction. It is presented by the greek letter Φ and it is a scalar number, varying between 0 and 1, or as a percentage between 0 and 100%. Porosity as a system categorizes into primary, secondary, fracture, vuggy, effective or open, ineffective or closed and dual porosity. From the aspect of pore diameter it includes macroporosity, mesoporosity and microporosity (Anovitz and Cole, 2015; Wikipedia, 2016).

While it is different from permeability, the two parameters are strongly correlated. The various expressions relating permeability to porosity include the equations of Krumbein and Monk, Berg, Van Baaren, Timur, Sen et al., Kozeny–Carman, Winland and Katz and Thompson (Ma, 2015; PetroWiki, 2015a).

1.3.3 Stochastic Processes

Stochastic or random process is a probability model which describes phenomena that evolve over time. It characterizes a system whose spatial variability is characterized by random fluctuations. Its probabilistic counterpart is the deterministic process. In a stochastic process there exists a certain amount of uncertainty. Even if the initial conditions are constant, there are several directions in which the process may evolve (Dodge, 2006). A generalization of a stochastic process is the random field, where the variable is no longer a simple value but can be multidimensional vectors. In natural sciences these values are often spatially correlated, with the correlation decreasing with distance (Vanmarcke, 2010). Stochastic processes are utilized in modelling and simulation. They serve to capture heterogeneity, simulate facies and petrophysical properties, honour and integrate multiple data types and also to quantify and assess uncertainty (PetroWiki, 2016a).

Earth science phenomena involve complex processes, making them to appear as random. However, natural processes that form reservoirs are not the result of a random process (PetroWiki, 2016a; Statios, 2000). These random variations are the results of deterministic depositional processes, although highly non-linear and chaotic. Only a small portion of the variability is explained by random behavior and is described by the nugget effect (Gringarten and Deutsch, 1999).

1.3.4 Geostatistics

Earth science data are not randomly distributed in a spatial context (Yarus and Chambers, 2006) but exhibit connectivity to a certain degree. Similarity between two points is inversely proportional to their distance. Geostatistics is a branch of applied statistics and mathematics that includes a set of tools for assessing and modelling spatial variability. This spatial variability includes information about heterogeneity and directionality within datasets. A more simplistic definition is that geostatistics deals with spatially autocorrelated data (Bohling, 2005). Moreover, geostatistics provides methods to quantify and evaluate the reliability and uncertainty of the generated models (PetroWiki, 2016b).

The significant contribution of geostatistics in petroleum industry lies in the fact that it is utilized in the study and development of heterogeneous reservoirs and in hydrocarbon recovery optimization. It constitutes one of the many methodologies incorporated into reservoir characterization processes. One of its many advantages is the capability to incorporate 3D seismic data. Its output is usually used in fluid–flow simulations (PetroWiki, 2016b). The most valuable feature of geostatistics is the ability to estimate data at locations inaccessible for measurement (Hristopulos, 2011).

Geostatistics was originally used in the mining industry in the early 1950s, to fill in for the insufficiency of classical statistical methods. In 1970s and due to advances in computer industry, its use spread to other areas of earth sciences and in the mid-to-late 1980s it was extensively used in petroleum industry, with its acceptance steadily growing (PetroWiki, 2016b). Examples of geostatistics application are flow simulation improvement (Almeida, 1999), tunnelling applications (Saratsis, 2004), rock formation characterization (Xiroudakis, 2007), subsurface temperature distribution studies (Agemar et al., 2012) and precipitation studies (Agou, 2016).

Chapter 2

Geostatistical Methods

The methods included in geostatistical analysis constitute in a conceptual way, a generalization of classical statistics. The workflow in geostatistics consists of several steps which follow an iterative path. The first step is exploratory data analysis, which serves to ensure data integrity. The second step is spatial modelling, which includes the derivation of an experimental (semi)variogram and matching it with a theoretical variogram model. Next is the application of kriging, an interpolation procedure applied to predict values. Following is conditional simulation, which is utilized to produce practical reservoir models and reproduce the spatial relationship and heterogeneity of various petrophysical properties. The last step is uncertainty analysis, which measures the degree of difference between subsequent realizations (Yarus and Chambers, 2006).

Based on the evaluation of the uncertainty analysis results and the engineer's experience, the initial data can be treated accordingly and the workflow can be repeated to acquire more satisfying results. The uncertainty in the estimated results can be due to the low number of wells and their unsuitable distribution in order to build the model, as well as the unsuitable network of structural framework (Amanipoor, 2013). However, the main source of uncertainty in these procedures comes from the geological structure of the reservoir itself, the variability of petrophysical properties and the locations of the oil–water and gas–oil contacts (Kamali et al., 2013).

2.1 Exploratory Data Analysis

While it is not a specific part of geostatistical analysis, it is considered a prerequisite. Primary data analysis includes univariate analysis like the mean, median, standard deviation, skewness and kurtosis and multivariate analysis, in which the relationship between two or more variables is examined (Yarus and Chambers, 2006).

2.1.1 Probability Density Function

The probability density function or PDF of a continuous random variable is a function which represents the probability of a random variable taking values within an infinitesimal range. It can be further used to estimate the probability of the random variable to take values within a particular wider range. This probability is calculated by integrating the variable's PDF over the requested range. The PDF takes values from 0 up to 1 and the integral over the entire range of values is equal to the unity (Hazewinkel, 1994). Another function very often used in combination with the PDF is the cumulative distribution function or CDF, which represents the probability of the random variable taking values less than or equal to a specific value. The same concept applies when treating discrete random variables. Summarizing, the PDF as well as the CDF are expressed by the following formulas:

$$\text{PDF: } \Pr[a \leq X \leq b] = \int_a^b f_X(x) dx \quad (2.1)$$

$$\text{CDF: } F_X(x) = \int_{-\infty}^x f_X(u) du \quad (2.2)$$

It is obvious that random variables in earth sciences draw values from the domain of real numbers ($x \in \mathbb{R}$).

2.1.2 Moments

Statistical moments are deterministic functions used to express expectations over all possible states of a random field (Agou, 2016). In classical statistics, moments are used to determine position, spread and shape of the distributed data. In a probability distribution, the zeroth moment represents the total probability, the first moment is the mean, second moment is the variance, third moment is the skewness and fourth moment is the kurtosis. Higher order moments, i.e. beyond fourth order, are used for further description of shape parameters. This concept is related to the concept of moments in physics (Hazewinkel, 1994).

Mean

Synonymous to the expected value of a distribution, the mean value is defined as the *arithmetic average* of the studied sample. It is the first moment of a PDF and is considered a measure of the central tendency of the data characterized by said distribution. It is usually denoted by the greek letter μ . For any data set, the terms arithmetic mean, mathematical expectation and average are usually used in the same manner. The mean is equal to the sum

of all possible values of the random variable X , weighted by the respective probability of each value $P(x)$. The calculations for discrete as well as for continuous univariate variables obey the same rules and are described as follows (Feller, 1968):

$$\text{Discrete variables: } \mu = E[X] = x_1p_1 + x_2p_2 + \cdots + x_kp_k = \sum_{i=1}^{\infty} x_i p_i \quad (2.3)$$

$$\text{Continuous variables: } \mu = E[X] = \int_{-\infty}^{\infty} xf(x) dx \quad (2.4)$$

where, E denotes the expectation operator.

Several types of mean values exist, like the pythagorean means, which consist of the arithmetic, the geometric and the harmonic mean. Furthermore, the means of probability distributions, such as the ones described above. Moreover, the generalized means, which divide into the power mean and the f-mean, the weighted arithmetic, truncated, interquartile, function mean, mean of angles and cyclical quantities, Fréchet mean and a number of other different mean types.

In probability distributions, the mean is frequently confused with the mode or the median, since all of them can be referred to as average. Although these three terms coincide for symmetrical distributions, the same does not apply for skewed distributions. In that case, the mean is the arithmetic average of the values, as it was already defined. However, the median is the middle value of the studied range, given that the values are ranked with increasing order and the mode is the value with the highest probability of occurrence or the "most likely value" (Feller, 1968).

Variance

Defined as the square root of the standard deviation of a PDF, the variance serves to measure the spread of values around their mean. It is a second order moment of a PDF and is usually denoted by σ^2 , s^2 , or $\text{Var}(X)$. The variance of a random variable X is expressed as the expectation of the squared deviation of a random variable from its mean and is formulated as follows (Feller, 1968):

$$\sigma^2 = \text{Var}(X) = E[(X - \mu)^2] = E[(X - E[X])^2] = E[X^2] - (E[X])^2 \quad (2.5)$$

where, μ denotes the mean and E the expectation operator.

The significance of this moment lies in the fact that it is used along with the mean value, to characterize distributions of random variables. In addition, it is a parameter utilized

to compare different values and also the degree of correlation between them. Ultimately, variance is used to as an indicator of error between measurements.

Skewness

The skewness of a distribution characterizes its shape and measures the asymmetry about the mean. It is a statistical moment of third order and is denoted by γ_1 or $\text{Skew}(X)$. The asymmetry coefficient or coefficient of skewness can be either positive, negative or undefined. A positive skew results in the mode value leaning to the left and the right tail to be longer. On the other hand, a negative skew results in the mode closer to the right and a longer left tail. For the calculation of the skewness coefficient of a random variable X , the Pearson's moment coefficient formula is used (Hazewinkel, 1994; Kenney and Keeping, 1962):

$$\gamma_1 = \text{Skew}(X) = E \left[\left(\frac{X - \mu}{\sigma} \right)^3 \right] = \frac{\mu_3}{\sigma^3} = \frac{E[(X - \mu)^3]}{(E[(X - \mu)^2])^{3/2}} = \frac{\mu_3}{\mu_2^{3/2}} \quad (2.6)$$

where, μ denotes the mean, σ the standard deviation, μ_2 and μ_3 the second and third central moments of the distribution respectively and E the expectation operator.

Other methods to measure the asymmetry is the distance between the mean and the mode, also suggested by Pearson, and the equation of Bowley, which does not depend as much as Pearson's on the tails of the distribution.

A significant contribution of skewness is to compare actual data with the assumed model. Many models assume normal distribution, which implies zero skewness. Thus, any deviation from that model can be depicted on the distribution plot (Kenney and Keeping, 1962).

Kurtosis

Kurtosis of a distribution is also a shape characteristic and indicates how peaked or flat-topped the distribution is. However, kurtosis is more related to the length and height of the tails. It is a fourth order moment and is denoted by γ_2 or $\text{Kurt}(X)$. The sharpness and narrowness of the peak increase with increasing kurtosis, which can take either positive or negative values (Kenney and Keeping, 1962). To calculate kurtosis, the following formula is used:

$$\gamma_2 = \text{Kurt}[X] = \frac{\mu_4}{\sigma^4} = \frac{E[(X - \mu)^4]}{(E[(X - \mu)^2])^2} \quad (2.7)$$

where, μ_4 denotes the fourth central moment, σ the standard deviation, μ the mean and E the expectation operator.

Also, the kurtosis is bounded below by the squared skewness plus 1:

$$\frac{\mu_4}{\sigma^4} \geq \left(\frac{\mu_3}{\sigma^3}\right)^2 + 1 \quad (2.8)$$

It is obvious that the standard deviation significantly influences kurtosis, since it is raised to the fourth power. In that sense the most remote values from the mean are the most influential. Thus, kurtosis can be considered a measure of the outliers of a distribution.

2.1.3 Probability Distributions

Probability or frequency distributions are the primary statistical tool to analyse and illustrate raw data, since they constitute a useful form of tabulation. Rough data do not provide any clear clues about the studied data set, so they have to be organised into classes of appropriate size in order to display the corresponding frequency of each class (Kenney and Keeping, 1962). Characteristic parameters of any distribution are the PDF and CDF, as well as the different order moments, which are utilized to capture the location, spread and shape of the distribution.

Based on these parameters, the distribution can be fit to one of several theoretical distribution models, which consequently can be used to estimate future behaviour. Theoretical models have been developed for both discrete and continuous distributions. Common discrete distributions include the models of Bernoulli, binomial, discrete uniform, geometric, hypergeometric, Poisson, logarithmic and many more. On the other hand, common continuous distributions include the normal, log-normal, logarithmic, multimodal, beta, gamma, lambda, continuous uniform, exponential, binomial, extreme value, logistic, Pareto or power law, Nakagami, Rayleigh, Rician, Weibull, student's t-distribution and more. For the purposes of this thesis, only a few of them will be presented in detail.

The distribution function estimation is an interesting and important problem, as it appears in many real problems of various scientific fields such as seismology, geology, hydrology, environmental sciences, etc. In many cases, the distribution function appears to be in direct relationship with the risk or nature hazard. A rich list of scientists and projects involved with such studies are presented by Quintela-Del-Rio and Estevez-Perez (2012).

Normal Distribution

The normal or Gaussian distribution or "bell curve" is a very frequently occurring continuous distribution, which belongs to the parametric family. It is very common in natural sciences, making it one of the most important frequency curves. The curve consists of a single peak,

which is bell shaped and is symmetrical about the mean. It depends on the mean μ and the standard deviation σ , is usually denoted by $N(\mu, \sigma)$ and is represented by the following PDF (Ang and Tang, 1975; Kenney and Keeping, 1962):

$$f_X(x) = \frac{1}{\sigma\sqrt{2\pi}} e^{-\frac{(x-\mu)^2}{2\sigma^2}} \quad (2.9)$$

It's simplest case, the standard normal distribution, is a distribution with $\mu = 0$ and $\sigma = 1$, denoted by $N(0, 1)$ and is described by the PDF:

$$f_S(s) = \frac{1}{\sqrt{2\pi}} e^{-\frac{s^2}{2}} \quad (2.10)$$

The expected value of the distribution, i.e. the mean, and the variance are presented bellow. Odd central moments are equal to zero due to symmetry and even central moments are given by the following formula. As a result, the skewness and kurtosis of the distribution can be calculated using Equations 2.6 and 2.7 (Walck, 2007):

$$\text{Even central moments: } \mu_{2r} = \frac{(2r)!}{2^r r!} \sigma^{2r} = (2r-1)!! \sigma^{2r}, \text{ for } r \geq 1 \quad (2.11)$$

$$\text{Mean=Median=Mode: } \mu = E[X] = \mu_1;$$

$$\text{Variance: } \sigma^2 = \mu_2; \mu_3 = 0; \mu_4 = 3\sigma^4 \quad (2.12)$$

$$\text{Skewness: } \gamma_1 = \frac{\mu_3}{\sigma^3} = 0; \text{ Kurtosis: } \gamma_2 = \frac{\mu_4}{\sigma^4} = 3 \quad (2.13)$$

It is very common to assume that a physical phenomenon follows the normal distribution, when the available data is insufficient for a more thorough analysis. In nature, many macroscopic phenomena are produced by the combined effect of numerous microscopic processes, which brings up the Gaussian random variable (Leon-Garcia, 2008). In a way, all manner of things appear to be distributed normally. The reason so many variables in nature tend to be distributed normally is due to the *Central Limit Theorem*. However, this theorem explains only the summation of random variables. The main reason that distinguishes the specific distribution is that out of all distributions with mean μ , variance σ^2 and support over all of \mathbb{R} , the normal distribution has the maximum entropy (Lyon, 2014).

The normal distribution is applied, among other cases, in gambling problems and error representation, as well as in biology, education and sociology (Kenney and Keeping, 1962),

in engineering applications (Ang and Tang, 1975), Monte Carlo simulations (Hastings, 1970), multivariate statistics problems (Azzalini and Capitanio, 1999), optimization procedures (Stewart, 1989), economics and marketing research (McDaniel and Gates, 2012) and many more.

Logarithmic Normal Distribution

Commonly referred to as the log-normal distribution, it characterizes the distribution of a random variable whose natural logarithm, $\ln X$, is normally distributed. The random variable can take only non-negative real values and the distribution displays similar properties and limitations to the normal distribution, in the logarithm domain. It depends on the mean $\lambda = E[\ln X]$ and standard deviation $\zeta = \sqrt{\text{Var}(\ln X)}$, is usually denoted by $N(\lambda, \zeta)$ and is represented by the following PDF (Ang and Tang, 1975):

$$f_X(x) = \frac{1}{\zeta x \sqrt{2\pi}} e^{-\frac{(\ln x - \lambda)^2}{2\zeta^2}} \quad (2.14)$$

The moments of the distribution are determined using the following formulas:

$$\text{Mean: } \mu = e^{(\lambda + \zeta^2/2)} \quad (2.15)$$

$$\text{Variance: } \sigma^2 = \text{Var}(X) = e^{\zeta^2} - 1 \quad (2.16)$$

This distribution has a wide range of applications, for example in material resistivity, precipitation studies or project management, fields of study which deal with positive variables and which are often expressed by log-normal distributions.

Multimodal Distribution

This non-parametric distribution is the result of combining multiple normal distributions with different modes and standard deviations. The desired values can be obtained using the *kernel estimator*. Each distinctive peak represents a different group of the population, which consequently indicates population heterogeneity. This model imposes minimal assumptions on the data and as a result the PDF provides a more representative display. It is used when a parametric distribution cannot properly describe the data or when assumptions should be avoided (Zhu, 2005). The simplest form is the bimodal non-parametric distribution, which consists of only two peaks. However, the kernel estimator can also be used for data that are normally distributed.

The form of the PDF depends mainly on the kernel function and the bandwidth parameter. It can be modelled using the Rosenblatt–Parzen kernel estimator (Parzen, 1962), resulting in the following function:

$$\hat{f}_h(x) = \frac{1}{nh} \sum_{i=1}^n K\left(\frac{x-x_i}{h}\right) \quad (2.17)$$

where, n denotes the sample size, $K(u)$ the kernel smoothing function and h the bandwidth.

Some common choices for the kernel smoothing function are provided by Silverman (1986):

$$\text{Epanechnikov: } K(u) = \max\left[0, \frac{3}{4} \left(1 - \frac{1}{5}u^2\right) 5^{-\frac{1}{2}}\right] \quad (2.18)$$

$$\text{Triangular: } K(u) = \max[0, 1 - ||u||] \quad (2.19)$$

$$\text{Gaussian: } K(u) = \frac{1}{\sqrt{2\pi}} e^{-\frac{u^2}{2}} \quad (2.20)$$

In order to determine the numerical moments of the distribution, the following functions can be used (Hansen, 2009):

$$\text{j-th moment of kernel: } \kappa_j(k) = \int_{-\infty}^{\infty} u^j k(u) du ; u = \frac{x-x_i}{h} \quad (2.21)$$

$$\text{Mean: } \mu = E[X] = \int_{-\infty}^{\infty} x \hat{f}(x) dx = \frac{1}{n} \sum_{i=1}^n x_i \quad (2.22)$$

where, the mean of the PDF is the same as the sample mean.

$$\begin{aligned} \text{Variance: } \sigma^2 &= E[X^2] - (E[X])^2 = \int_{-\infty}^{\infty} x^2 \hat{f}(x) dx - \left(\int_{-\infty}^{\infty} x \hat{f}(x) dx\right)^2 \\ &= \hat{\sigma}^2 + h^2 \kappa_2(k) \end{aligned} \quad (2.23)$$

where, $\hat{\sigma}^2$ denotes the sample variance.

Galtung (1968) introduced a classification system for these distributions, which takes into consideration the position and number of peaks. Zhu (2005) collected and presented a number of multimodality tests that can be found in the statistical literature. Furthermore,

Pyrzcz and Deutsch (2014) made an important observation that, a bimodal histogram does not imply non-stationary data, rather than it means that the data should be separated into two groups under the condition that they display distinct statistical and geological properties.

Multimodal distributions are widely applied and are indicatively used in economics (Zhu, 2005), in earthquake and hydrology studies (Quintela-Del-Rio and Estevez-Perez, 2012), in traffic monitoring, visual surveillance and object tracking and recognition (Elgammal et al., 2002), in DNA data studies (Basturk et al., 2012) and in ecology and agriculture (Xu et al., 2010).

2.2 Spatial Modelling

The modelling of spatial information is achieved with variography, or structural analysis, whose main purpose is the identification and quantification of two-point correlations of the data. This information is in turn used for interpolation or simulation, in order to preserve the directions and scales of continuity. The inputs for this analysis are a grid and a set of control points or in the case of geological applications, well locations. In other words, the required information for this analysis are the data at the points of interest and their location in a spatial context. In a way, variogram analysis is a distance and directional weighting problem (Yarus and Chambers, 2006). The results of variography are reliable in large media, due to the fact that the *ergodic hypothesis*, i.e. the equivalence between ensemble and spatial averages, is justified for very large data sets, i.e. large initial population (Paleologos et al., 1996).

The primary tool used in variography is the variogram, or more accurately *semivariogram*, although the latter term tends to disappear from the literature. Variography as a method itself, is the iterative procedure of calculating, interpreting and modelling variograms. The variogram describes the geological continuity of variables within relatively homogeneous layers (Amanipoor, 2013) and it is the most common measure of spatial correlation used for porosity and permeability modelling (Pyrzcz and Deutsch, 2014). Preferred by geostatisticians, the variogram tends to filter the influence of a spatially varying mean, by averaging squared differences of the variable. In addition, the variogram can be defined in some cases that the covariance function cannot. This is due to the *intrinsic hypothesis*, a weaker form of second-order stationarity of the variable (Bohling, 2005).

The variogram curve is a plot of variance as a function of distance. It is characterized by three important components, nugget, sill and range, all of which contribute to deeper understanding of the data. The three components are described in detail in the following paragraphs, while their visual representation is displayed in Figure 2.1. In addition, an accurate illustration of the correlation instances at different lag distances is described in

Figure 2.2. These parameters are essential since the variogram can only be modelled utilizing these three values (Pyrzcz and Deutsch, 2014).

Nugget

Theoretically at zero separation (lag) distance, the variogram value is zero. However, the existence of nugget effect or simply nugget, indicates the presence of noise, i.e. random and uncorrelated data, at all lag distances. Numerically, the point that the variogram intersects the y-axis of the graph is equal to the nugget. Below that point the data cannot be interpreted and thus, provide no useful information (Yarus and Chambers, 2006). Main causes of this effect are geologic features like lithology, sedimentary environments and tectonic structures (Amanipoor, 2013), as well as measurement errors (Pyrzcz and Deutsch, 2014).

Usually it characterizes feature scales smaller than the sampling interval. In geological applications, most variables in sedimentary environments are locally continuous, thus the nugget effect is usually limited up to about 30% (Pyrzcz and Deutsch, 2014; Yarus and Chambers, 2006). Furthermore, another useful term is the *relative nugget effect*, which is defined as the nugget (C_0) divided by the sill (C) (Amanipoor, 2013).

Sill

It is the inflection point of the curve at which the variogram flattens, i.e. reaches a plateau. The value of the sill corresponds to zero correlation between data points, which can be also realized in Figure 2.2. It is equal to the theoretical true variance of the studied sample, which also makes it an additional validation criterion for the subsequent variogram modelling (Yarus and Chambers, 2006). The significance of this parameter lies in the fact that the behaviour of the variogram curve relatively to the sill, indicates the existence of trends in the data, which will have to be treated accordingly and which is also illustrated in Figure 2.3. One final remark is that in case of non-stationary data the variogram never reaches the sill.

Range

Correlation range or scale, describes the distance at which the variogram reaches the sill. Up to that distance, the relationship with the variance is predictable. Points at distances greater than the range have practically no effect on estimation. The range typically depends on direction, with the horizontal directions displaying greater range due to increased continuity. However, range alone is not that important, as the total shape of the variogram (Amanipoor, 2013; Yarus and Chambers, 2006).

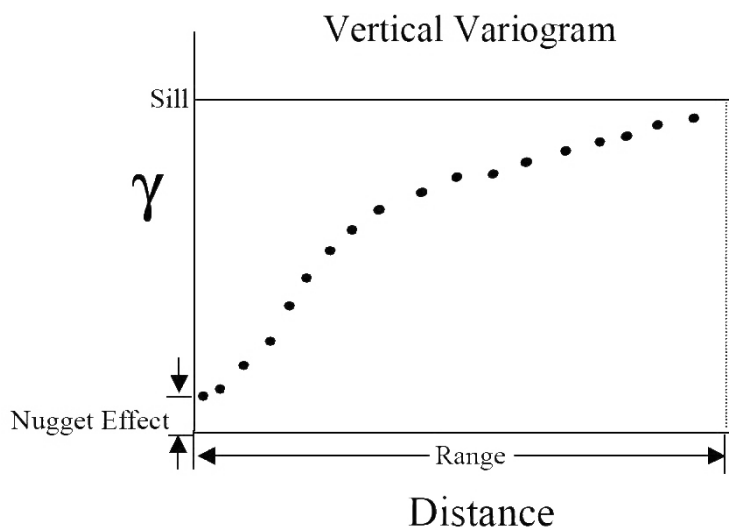


Fig. 2.1 Indicative vertical variogram plot describing the nugget, sill and range. Figure retrieved from Statios (2000).

Additional parameters contributing to its final shape, are the direction of the variogram and isotropy of the medium. While they are not required for variogram modelling, they affect its shape and characteristics.

Directionality

Depending on the direction of the lag distances, the variogram is classified into categories. This classification is important because information, and thus variogram properties, usually change for different directions. Typically one variogram at a time is considered, which is computed for all lags and all directions, irrespective of both azimuth and altitude, i.e. a *3D variogram*. The 3D variogram is the most useful tool in geological applications, since it contains information irrespective of direction and can subsequently be used for building the 3D model of the required formation.

Restricted by direction, data pairs can be selected in such a manner as to have a particular orientation, thus producing the *directional variogram*. In the case that the data points lie on a single horizontal or vertical path, then the horizontal or vertical variogram is produced respectively. A disadvantage of horizontal variograms is that horizontal wells rarely recognise the stratigraphic "time lines" (Pyrzcz and Deutsch, 2014). Furthermore, considering all possible pairs, irrespective of azimuth, results in the *omnidirectional variogram*. Notice that the omnidirectional variogram does not imply the same behaviour in all directions. Nowadays, computer software has integrated the calculation of the *variogram map*, depicting

the variance of all azimuths. It is not a geological map, but a polar graph of variance and azimuth along different lag increments (Yarus and Chambers, 2006).

Isotropy

Isotropy is a property of continuous materials, which characterizes the behaviour of an attribute with respect to different orientations. An attribute displaying the same behaviour along all different directions is a feature of isotropic materials. On the other hand, varying behaviour along different directions, characterizes an anisotropic material. In geological applications, the main reasons behind anisotropy are layering, faulting and layer inclination. Anisotropy can increase the nugget effect and also make the final variogram hard to interpret.

Different range in various parameters (Amanipoor, 2013) and directional dependency of range (Ayan et al., 1994) establishes anisotropy. This leads to the realisation that the top view of an isotropic variogram will be round, while of an anisotropic will be an ellipsoid. In that sense, the variograms of two different directions for the same data sample will not coincide. Examples of anisotropic behaviour are displayed in Figure 2.4 for regular and irregular strata.

A similar concept to isotropy is homogeneity, where the material is continuous and isotropic along its total volume. On the other hand, a heterogeneous material is only locally homogeneous while the total volume is not. Heterogeneity can also be determined as positional dependency of results (Ayan et al., 1994). A common feature of hydrocarbon reservoirs and other geological formations is high heterogeneity, caused by the complex sedimentation processes and post-sedimentary events (Masihi et al., 2016). Examples of such behaviour can be seen in Figure 2.4 by observing the different lenses configuration.

2.2.1 Experimental Variogram

Data points are classified in a variety of separation distances called lags or lag distances, and being denoted by h . For a given lag, the results of each pair are summed up and averaged and then plotted as variance against mean lag distance. This curve is called variogram and one half of the variogram is the so called experimental *semivariogram*, denoted by $\hat{\gamma}(h)$. However, the word "variogram" is mostly used when referring to the semivariogram (Pyrzcz and Deutsch, 2014; Yarush and Chambers, 2006). The variogram generated by using experimental data retrieved from samples is called the experimental variogram and its function is described in Equation 2.25.

The first step in estimating the experimental variogram function is to determine the lag distance. For directional variograms this can be decided based on the geostatistician's experience. However, when the 3D variogram is required, the following formula can be used

to determine the rescaled lag distance (Pyrcz and Deutsch, 2014):

$$h = \sqrt{\left(\frac{h_{vert}}{a_{vert}}\right)^2 + \left(\frac{h_{h-major}}{a_{h-major}}\right)^2 + \left(\frac{h_{h-minor}}{a_{h-minor}}\right)^2} \quad (2.24)$$

where, h_i are the three principal components of the distance vector and a_i are the distance range parameters for the vertical, major horizontal and minor horizontal direction respectively. The range parameters may vary for different nested structures and are calculated or iteratively adjusted, in order to fit all directional sample variograms.

The next step is to estimate the function of the experimental variogram (Pyrcz and Deutsch, 2014):

$$\hat{\gamma}(h) = \frac{1}{2N(h)} \sum_{N(h)} [z(u) - z(u+h)]^2 \quad (2.25)$$

where, $N(h)$ denotes the number of pairs for lag h , $z(u)$ the random function of random variable Z of interest and u the coordinate location vector.

The generated experimental variogram is characterized by a certain nugget, range and sill, as well as a certain shape. These are the parameters that will be used for subsequent interpretation. As already described, directional dependence of range, indicates anisotropy. Furthermore, the shape of the variogram in relation to the sill provides valuable information on the possibility of an existing pattern or trend. Indicators of geological variability include the nugget effect, geometric anisotropy, cyclicity, large-scale trends and zonal anisotropy (Pyrcz and Deutsch, 2014). Some of these trends are represented in Figure 2.3.

Nugget Effect

The nugget effect contains information about data at points closer than the smallest experimental lag. Any error in measured values, or at the location of study, as well as sparse and uncorrelated data, contribute to an increased nugget effect. This effect was thoroughly presented during the description of variogram parameters in Section 2.2.

Geometric Anisotropy

Geometric anisotropy is accompanied by a variogram with similar shape for the vertical and horizontal direction. This variogram behaviour is justified as such. Depositional processes include spatial correlation of petrophysical properties. The correlation magnitude decreases with lag distance until a distance with no obvious correlation exists, i.e. the range. The length scale of correlation is direction dependent. Obviously, due to layering of depositions, the

vertical range is typically much smaller than the horizontal. Despite the fact that range is direction dependent, the decrease pattern in correlation is often similar in different directions, which can be explained by Walther's Law of Facies.

Cyclicality

Cyclicality or hole effect, is observed when cyclic behaviour is captured by the variogram. Depositional procedures usually repeat over geological time, leading to repetitive variations of petrophysical properties. In that case, there will be an alternating positive and negative correlation on the variogram, with increasing lag distance. Usually, the cyclic behaviour dampens out over large distances, due to the scale of the geologic cycles (Pyrz and Deutsch, 2014). While porosity and lithology are the main reasons behind hole effect, the increasing number of lags can also contribute to its increase (Amanipoor, 2013). It can also be linked to insufficient data. Extensive examples of this trend can be seen in Figure 2.4.

Large Scale Trends

Upward or downward coarsening vertical trends are an indicative example of this category. In this case, the variogram reaches and surpasses the sill, implying that spatial correlation, even if negative, never ceases to exist.

Zonal Anisotropy

Constitutes a subcategory of geometric anisotropy in which, the correlation range in a certain direction surpasses the size of the formation. As a result, the variogram never reaches the sill. Zonal anisotropy is divided into two cases, based on direction. Areal trends, which cause the vertical variogram to never deplete the correlation along the vertical direction, and stratigraphic layering, which affects the variogram along the horizontal direction, usually for smaller scale features (Gringarten and Deutsch, 1999; Pyrcz and Deutsch, 2014).

All of these cases are involved in the geological interpretation of the variogram, which will be used in variogram modelling. Usually, they appear in combination of more than one. Some general guidelines for variogram interpretation include the exclusion of noisy results and the utilization of a proper variogram for all distances and directions, thus a 3D variogram. Also, any trends have to be removed, the variogram analysis will be performed using the residual data and the trend will be added back to the estimated values.

The significant problem in variogram interpretation is the lack of data, so that a reliable variogram can be generated. To fill this information gap, data from analog formations are

used, i.e. from reservoirs with similar depositional settings (Pyrcz and Deutsch, 2014). Summarizing, the experimental variogram has to be well understood, before it can be modelled appropriately.

2.2.2 Theoretical Variogram Model

Following after the calculation and treatment of the experimental variogram, is the variogram modelling, which produces a properly fit variogram model, ready to be used in further geostatistical analysis. The experimental variogram alone is insufficient for this analysis and has to be fit to an appropriate theoretical model (Amanipoor, 2013). The goal of this procedure is to accurately capture the nugget, range and sill, as well as the shape, by using specific functions. The most common are the spherical, exponential, Gaussian, linear and power functions. There are additional modelling functions, but these are the only models that ensure mathematical stability during calculations (Isaaks and Srivastava, 1989). These functions have the property of positive definiteness, which ensures that ultimately the kriging equations can be solved (Gringarten and Deutsch, 1999). They are described in the following equations (Pyrcz and Deutsch, 2014) and their graphical representation appears in Figure 2.5.

Nugget Effect Model

This models the pure nugget model, in which there is no distinctive succession of the correlation values. It is described by the function:

$$\Gamma(h) = \begin{cases} 0 & \text{if } h = 0 \\ 1 & \text{if } h > 0 \end{cases} \quad (2.26)$$

Spherical Model

Increases in a linear function and reaches a sill of 1 at a range of 1. Although the curve rises linearly, the slope is not that steep. It is described by the function:

$$\Gamma(h) = \text{Sph}(h) = \begin{cases} [1.5h - 0.5h^3] & \text{if } h \leq 1 \\ 1 & \text{if } h \geq 1 \end{cases} \quad (2.27)$$

Exponential Model

Similar to the spherical, with the difference that the curve rises more abruptly and reaches the sill asymptotically. It is described by the function:

$$\Gamma(h) = \text{Exp}(h) = 1 - e^{-3h} \quad (2.28)$$

Gaussian Model

Has a parabolic shape at short distances. It is described by the function:

$$\Gamma(h) = \text{Gau}(h) = 1 - e^{-3h} \quad (2.29)$$

Hole Effect Model

It is applied only for a single direction. However, it is rarely used. It is described by the function:

$$H_{\alpha}(h) = 1.0 - \cos(h\pi) \quad (2.30)$$

Dampened Hole Effect Model

The exponential term captures more properly the different distance scale. It also functions only for a single direction, but it is used more frequently than the Hole Effect model. It is described by the function:

$$DH_{d,\alpha}(h) = 1.0 - \exp\left(\frac{-3h\alpha}{d}\right) \cos(h\alpha) \quad (2.31)$$

Power Law Model

This model is characteristic of trends and fractal type behaviour. It is described by the function:

$$\Gamma(h) = h^{\omega} \text{ where } 0 < \omega \leq 2 \quad (2.32)$$

2.3 Kriging

After the appropriate theoretical variogram is determined and fit to experimental data, kriging can commence. Kriging can be considered as a form of generalized linear regression, aiming

to the generation of an optimal spatial estimator in a minimum mean–square prediction error sense (Olea, 2009). Simply put, it is a method to reproduce the full volume of the formation and create a map of predicted values, using data dependence and measurements at set locations. It is the primary interpolation method used in geostatistics and functions by utilizing more than one parameter simultaneously to estimate values of a random variable over a spatial region (Yarus and Chambers, 2006). A significant observation is that each new variable presented to the model calls for variogram analysis and modelling once again (Isaaks and Srivastava, 1989). As already explained, any existing trend will have to be removed prior to the procedure and will be ultimately added back after kriging is performed.

The main concept is to minimize the expected squared error between the true value $z(u)$ and the estimated value $z^*(u)$ at a certain location. This optimization is achieved by applying regression on the weight factors of the estimation parameters (Pyrz and Deutsch, 2014). However, geostatistics are used to estimate values at locations that cannot be reached and where the true values are unknown. For this reason, for the final validation of the model, only a certain number of known locations are used to perform the variogram analysis and kriging and subsequently, the estimated values are compared to the true values at the rest of the known locations. The method is most effective when applied inside the convex hull determined by the peripheral data (Olea, 2009).

Various methods have been developed, with most of them being expressed by linear relationships and considering weight factors for each data point. The main categories and respective calculation formulas are described below (Olea, 2009):

2.3.1 Simple Kriging

Consists the primary form of kriging. In this case, a constant and known mean is assumed. It comprises a system of linear equations, used to optimize the weight factors λ . The estimate $z_{SK}^*(s_0)$ at a certain location s_0 is calculated by the following formula:

$$z_{SK}^*(s_0) = m + \sum_{i=1}^n \lambda_i (z(s_i) - m) \quad (2.33)$$

where, s_i denotes the location of measurement i , n the number of observations, m the mean of $Z(s)$ and λ_i the weight factor.

The weight factors are scalar numbers, which are determined through an iterative optimization procedure, using the following system of equations, the so called *normal system of*

equations:

$$\left. \begin{aligned} \sum_{i=1}^k \lambda_i \text{Cov}(s_i, s_1) &= \text{Cov}(s_0, s_1) \\ \sum_{i=1}^k \lambda_i \text{Cov}(s_i, s_2) &= \text{Cov}(s_0, s_2) \\ &\vdots \\ \sum_{i=1}^k \lambda_i \text{Cov}(s_i, s_k) &= \text{Cov}(s_0, s_k) \end{aligned} \right\} \quad (2.34)$$

$$\begin{bmatrix} \text{Cov}(s_1, s_1) & \cdots & \text{Cov}(s_k, s_1) \\ \vdots & \ddots & \vdots \\ \text{Cov}(s_1, s_k) & \cdots & \text{Cov}(s_k, s_k) \end{bmatrix} \begin{bmatrix} \lambda_1 \\ \vdots \\ \lambda_k \end{bmatrix} = \begin{bmatrix} \text{Cov}(s_0, s_1) \\ \vdots \\ \text{Cov}(s_0, s_k) \end{bmatrix}$$

where, λ_i denotes the weight of measurement at the location of interest s_i and $\text{Cov}(s_i, s_j)$ the covariance value between measurements at different locations.

After determining the respective weights, the minimum error variance is calculated by the following formula, considering the necessary assumptions:

$$\sigma^2(s_0) = \text{Cov}(s_0, s_0) - \sum_{i=1}^k \lambda_i \text{Cov}(s_0, s_i) \quad (2.35)$$

The procedure is repeated until the minimum error variance associated with the estimation of $z_{SK}^*(s_0)$ is achieved. Only then can the weight factors be used in estimation. In order to be acceptable, the variance function of Equation 2.35 has to be positive definite.

Simple kriging is characterized by a set of properties, like nonconvexity, screen effect and global unbiasedness. It is also considered an exact interpolator, namely the error variance is zero. It is intolerant to duplicated sites and independent of the coordinate system used (Olea, 2009).

2.3.2 Ordinary Kriging

If the weights of simple kriging sum up to the unity, the estimator is independent of the mean value. This applies to samples with constant but unknown mean and gives rise to an improved form of simple kriging, the ordinary kriging. The estimate $z_{OK}^*(s_0)$ of this method at the location s_0 is given by:

$$z_{OK}^*(s_0) = \sum_{i=1}^n \lambda_i z(s_i) \quad (2.36)$$

where, s_i denotes the location of measurement i , n the number of observations and λ_i the weight factor.

The normal system of equations for optimal weights, assuming stationarity:

$$\left. \begin{aligned} \sum_{i=1}^k \lambda_i \text{Cov}(s_i, s_1) + \mu &= \text{Cov}(s_0, s_1) \\ &\vdots \\ \sum_{i=1}^k \lambda_i \text{Cov}(s_i, s_k) + \mu &= \text{Cov}(s_0, s_k) \\ \sum_{i=1}^k \lambda_i &= 1 \end{aligned} \right\} \quad (2.37)$$

$$\begin{bmatrix} \text{Cov}(s_1, s_1) & \cdots & \text{Cov}(s_k, s_1) & 1 \\ \vdots & \ddots & \vdots & \vdots \\ \text{Cov}(s_1, s_k) & \cdots & \text{Cov}(s_k, s_k) & 1 \\ 1 & \cdots & 1 & 0 \end{bmatrix} \begin{bmatrix} \lambda_1 \\ \vdots \\ \lambda_k \\ \mu \end{bmatrix} = \begin{bmatrix} \text{Cov}(s_0, s_1) \\ \vdots \\ \text{Cov}(s_0, s_k) \\ 1 \end{bmatrix}$$

where, λ_i denotes the weight of measurement at the location of interest s_i , $\text{Cov}(s_i, s_j)$ the covariance value between measurements at different locations and μ is the Lagrange multiplier, which is a constant used to optimize multi-variable functions.

The minimum error variance:

$$\sigma^2(s_0) = \text{Cov}(s_0, s_0) - \sum_{i=1}^k \lambda_i \text{Cov}(s_0, s_i) - \mu \quad (2.38)$$

The procedure is repeated until the minimum error variance associated with the estimation of $z_{OK}^*(s_0)$ is achieved.

This method has the same properties as simple kriging and additionally, the estimate error variance for ordinary kriging is greater or equal to that of simple kriging. Also, the observations used for estimation should lie within a close search neighbourhood, while a proper number of observations used is considered from 3 to 25 (Olea, 2009).

2.3.3 Universal Kriging

This method, also known as *kriging with trend*, constitutes a full generalization of simple kriging, as well as a further improvement of ordinary kriging. It can be applied with a neither constant, nor known mean value. However, universal kriging should be used with caution since increasing model complexity influences estimation uncertainty.

An important note is that, this method is applied on the residual function $Y(s)$, once the trend $m_z(s)$ is removed from the random function $Z(s)$, namely:

$$\text{Residual function: } Y(s) = Z(s) - m_z(s) \quad (2.39)$$

$$\text{Trend or drift function: } m_z(s) = a_0 + \sum_{i=1}^n a_i f_i \quad (2.40)$$

where, f_i denotes the trend function and a_i the trend coefficients.

The normal system of equations for optimal weights, is the following. Due to high complexity it is presented in tabular form:

$$\begin{aligned} \mathbf{K} &= \begin{bmatrix} \text{Cov}_Y(s_1, s_1) & \dots & \text{Cov}_Y(s_k, s_1) & 1 & f_1(s_1) & \dots & f_n(s_1) \\ \vdots & \ddots & \vdots & \vdots & \vdots & \ddots & \vdots \\ \text{Cov}_Y(s_1, s_k) & \dots & \text{Cov}_Y(s_k, s_k) & 1 & f_1(s_k) & \dots & f_n(s_k) \\ 1 & \dots & 1 & 0 & 0 & \dots & 0 \\ f_1(s_1) & \dots & f_1(s_k) & 0 & 0 & \dots & 0 \\ \vdots & \ddots & \vdots & \vdots & \vdots & \ddots & \vdots \\ f_n(s_1) & \dots & f_n(s_k) & 0 & 0 & \dots & 0 \end{bmatrix} \\ \mathbf{k} &= [\text{Cov}_Y(s_0, s_1) \quad \dots \quad \text{Cov}_Y(s_0, s_k) \quad 1 \quad f_1(s_0) \quad \dots \quad f_n(s_0)]^T \\ \mathbf{x} &= [\lambda_1 \quad \dots \quad \lambda_k \quad -\mu_0 \quad -\mu_1 \quad \dots \quad -\mu_n]^T \\ \mathbf{Z} &= [Z(s_1) \quad \dots \quad Z(s_k) \quad 0 \quad 0 \quad \dots \quad 0]^T \end{aligned} \quad (2.41)$$

$$\text{Normal equations: } \mathbf{K}\mathbf{x} = \mathbf{k} \quad (2.42)$$

$$\text{Estimator: } Z_{UK}^* = \mathbf{Z}^T \mathbf{x} \quad (2.43)$$

$$\text{Estimation variance: } \sigma_{UK}^2 = \text{Cov}_Y(0) - \mathbf{k}^T \mathbf{x} \quad (2.44)$$

Other estimation methods are Lognormal Kriging, Multigaussian Kriging and Indicator Kriging, which are simply one of the aforementioned forms applied to appropriately transformed data. Furthermore, Block Kriging, Cokriging, Crossvalidation, Sequential Gaussian Simulation, Simulated Annealing, Filter Simulation, Cluster Analysis and more (Olea, 2009; Pyrcz and Deutsch, 2014).

2.4 Upscaling

Although it is not considered a mandatory part of geostatistical analysis, upscaling or model scaling, is an averaging technique commonly used in combination with geostatistical procedures. A simple definition for upscaling considers it as a procedure to shift from a fine grid scale to a larger, coarse grid scale (Renard and de Marsily, 1997). As Farmer (2002) points out, the upscaling problem is expressed by the need to calculate equivalent point permeabilities without small scale heterogeneities, so that the solution of the coarse scale problem reaches the solution of the fine scale problem. This technique is necessary in order to move from fine grid data scale, to model scale and subsequently to flow grid scale. The main reason for upscaling a model is to reduce the computational time and resources of flow simulation, which is often significantly demanding, considering the high complexity of the geological model and simulation methods. Additional applications of upscaling are to compress model information, i.e. reduce a 3D model to a 2D map or generate a large scale model (Pyrzcz and Deutsch, 2014). Depending on the degree of scaling, two types of permeability can be obtained. *Block* or upscaled *permeability*, which resembles the equivalent permeability of a finite size block and *equivalent permeability*, which is a single value corresponding to the whole model.

Upscaling is applied to facies, porosity, saturation and permeability data. Saturation and porosity are sufficiently averaged using an arithmetic mean. However, since permeability is connected to the direction of flow, an arithmetic average does not suffice in this case and thus, a number of upscaling methods have been derived to deal with this issue. The simplest permeability averaging techniques are arithmetic averaging, which is suited for cells parallel to the flow, harmonic averaging, for cells in series relative to the flow and geometric averaging, which applies to white-noise random media (Pyrzcz and Deutsch, 2014). Detailed reviews and comparison studies of upscaling methods for permeability are presented in the studies of Renard and de Marsily (1997) and Farmer (2002). These methods fall into the following main categories.

First and foremost, *inequalities for equivalent permeability* have been derived in the form of upper and lower bounds. Such inequalities include the Wiener, Hashim and Shtrikman, Cardwell and Parsons, Matheron and Ene bounds. Fundamentally, the Wiener bounds state that equivalent permeability is bounded below by the harmonic mean and above by the arithmetic mean of the studied data. The other methods constitute alterations of this fundamental inequality, while taking into consideration isotropy, homogeneity, number of phases or even direction of successive averaging. Although these methods are fast, they restrict mostly to uniform flow.

Heuristic methods include Sampling, a basic technique which is very common in petroleum industry (Renard and de Marsily, 1997), and according to which, a block is assigned the permeability measured at its center. The averaging means and power averaging methods suggest that permeability is equal to a weighted average of the aforementioned bounds and apply this method to two or three dimension models. Finally, the flexible grid method, where the size of the large scale grid is modified as a function of a certain parameter, for example permeability variance. This way, the error of scaling can be minimized. These methods are very fast and display no significant application restrictions.

Moving on to *deterministic methods*, which require the assumption that the permeability field and the boundary conditions are known. For simple permeability fields the analytical solution of the diffusion equation is sufficient and specifically for uniform flow in stratified media, it proves that arithmetic average is used for flow parallel to the strata, while harmonic average for flow perpendicular to the strata (Pyrzcz and Deutsch, 2014; Renard and de Marsily, 1997). Furthermore, percolation theory treats the problem from a statistical aspect, dividing the model into permeable and non-permeable cells, while at the same time introducing the threshold permeability, a permeability value for which, the blocks with higher permeability form clusters connecting the two opposite sides of the model (Masihi et al., 2016). The theory of effective media dictates that a heterogeneous medium consisting of neighbouring homogeneous blocks can be substituted by a single inclusion with a certain permeability value. The streamline method is used in binary sand-clay systems and determines equivalent permeability by measuring the pressure losses due to the tortuous flow along the sand matrix. Renormalization methods are approximate calculations of equivalent permeability, based on repetitive series of successive unifications. Desirably, the ultimate goal is to acquire a single block value. Additional methods include the numerical solution of the diffusion equation, which includes the solution of partial differential equations using local and non-local methods, and homogeneous-equation methods, which use mathematics to derive equations on the higher scale based on equations of the given scale. Deterministic methods offer a wide field of applications and their speed vary according to the applied method.

Last but not least, *stochastic methods* consider the variables of interest as randomly varying in space, thus making these methods a way to deal with the uncertainty accompanying the partial knowledge of the model (Renard and de Marsily, 1997). These methods include the rule of geometric averaging, which is considered one of the few exact solutions, approximated analytical results and conjectures, and block permeability estimation methods, which make use of the expectation, covariance and cross-variance of block and local permeability. Other methods include the spectral method, perturbation method, field theory, Monte Carlo method and more. These methods apply mostly to uniform flow and offer a fair solution speed.

2.4.1 Simplified Renormalization

Renormalization originates from statistical physics, however its application was expanded to the calculation of equivalent permeability. This method is based on the averaging of permeability values and unification of blocks in an iterative manner. Starting from a given grid, a coarser discretized grid is acquired, repeating until the desired size is reached or until an ultimate single value, equivalent for the whole model is determined. Since there is no exact formulation, the solutions are considered approximate. Although renormalization is simple and popular, it often underestimates permeability (Renard and de Marsily, 1997). Several forms of this method have been derived, however for the purposes of this thesis only a certain one will be described.

Renard et al. (1997) proposed the method of Simplified Renormalization, according to which, the upscaling is carried out through successive grouping of two cells. Should these cells be in parallel to the flow direction, the arithmetic average is used, otherwise if they are in series with respect to the flow direction, the harmonic average is used. Simply put, if the flow vector penetrates the interface of two cells, they are harmonically averaged. The two types of average are represented in Equations 2.45 and 2.46. At every iteration, the direction of averaging changes, while the order is always kept constant, for example the first averaging is done along X-direction, then Y and finally Z, with the same order at every iteration. It is self-evident that depending of the choice of averaging succession, the final result can be different. A summarizing image of the described method for a two dimensional plane appears in Figure 2.6.

$$\text{Arithmetic Average: } \mu_a = \frac{1}{n} \sum_{i=1}^n x_i \quad (2.45)$$

$$\text{Harmonic Average: } \mu_h = \frac{1}{\frac{1}{n} \sum_{i=1}^n \frac{1}{x_i}} \quad (2.46)$$

where, x_i denotes the random variable and n the population.

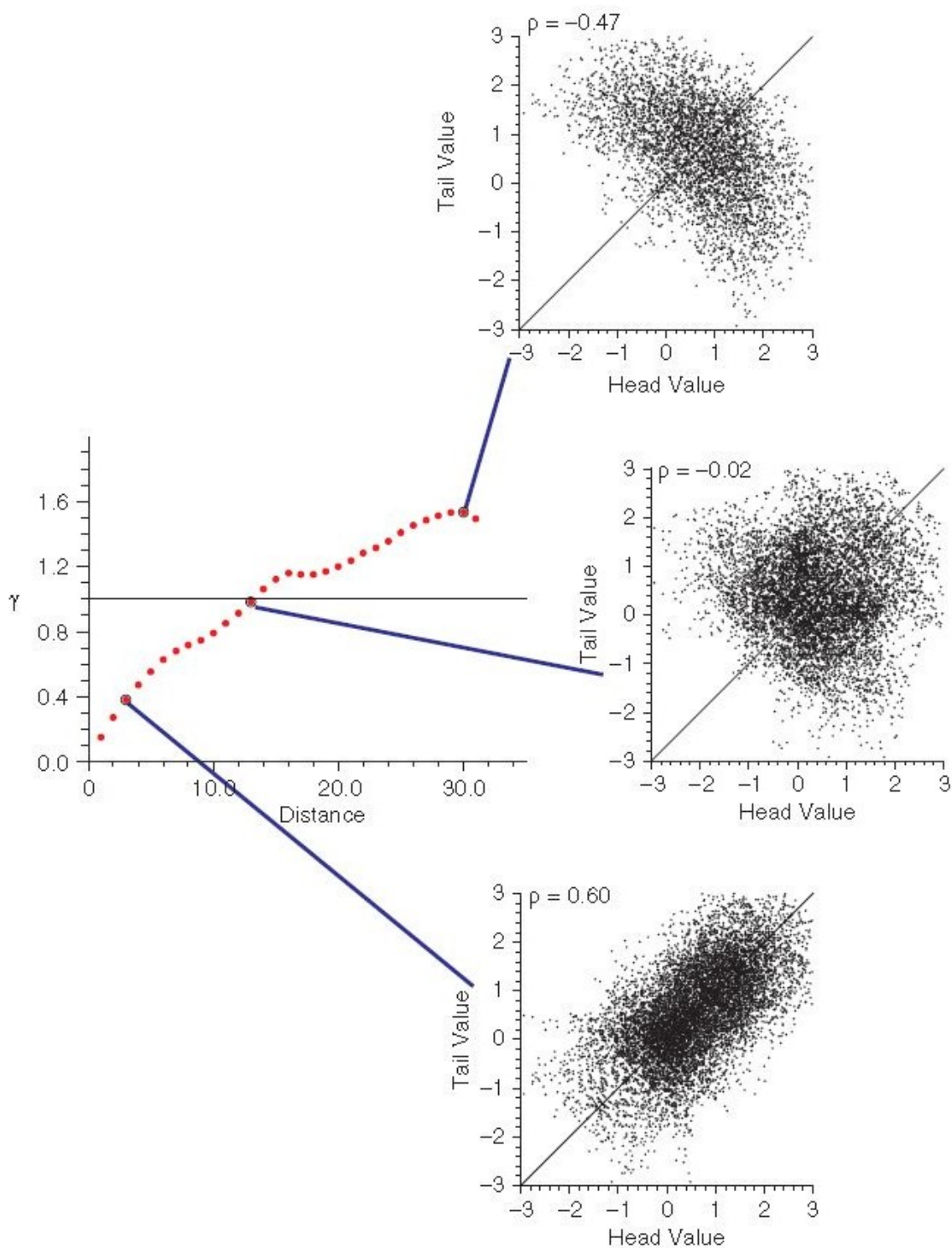


Fig. 2.2 The variogram describes the correlation instances at different lag distances, using the respective scatterplots corresponding to three lag vectors on a typical variogram. Correlation is denoted by ρ . Note that below the sill correlation is positive, while above the sill it is negative. Figure retrieved from Pyrcz and Deutsch (2014).

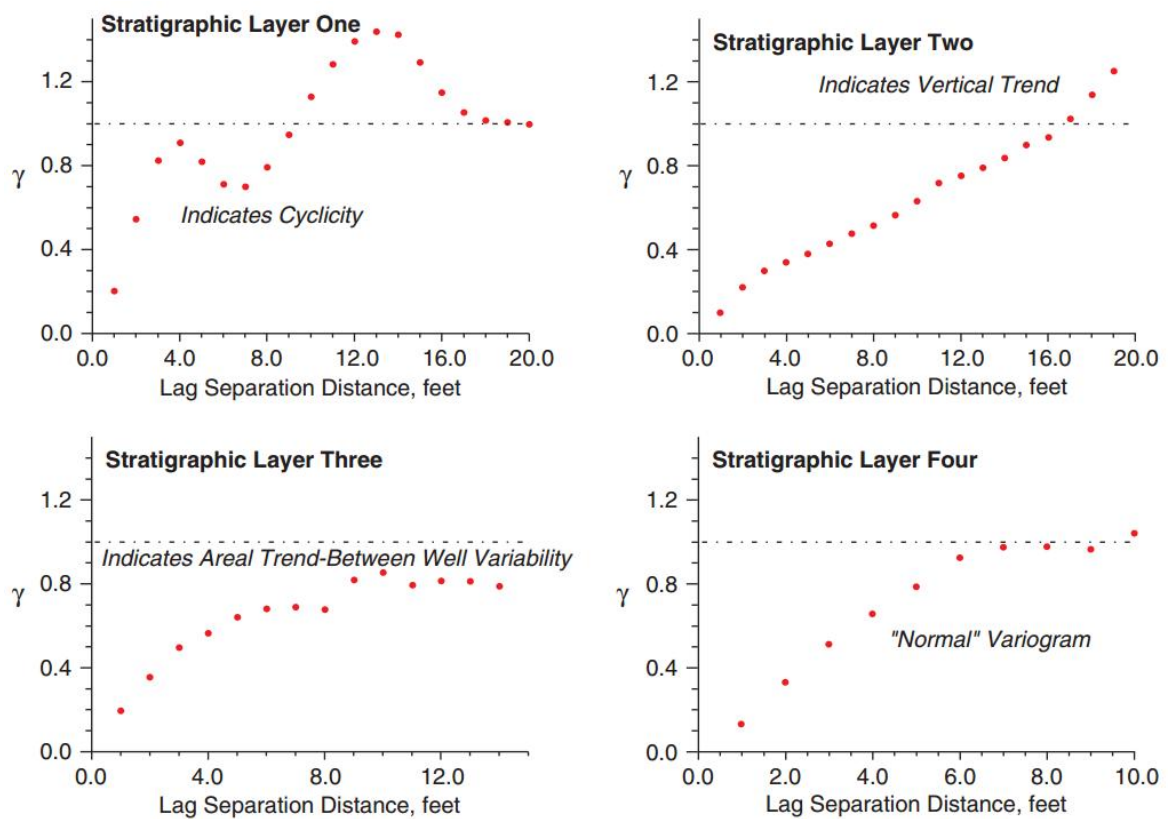


Fig. 2.3 Experimental variograms displaying different types of trends. Dash-dotted horizontal line represents the sill. Variance values are normalized. Figure retrieved from Pyrcz and Deutsch (2014).

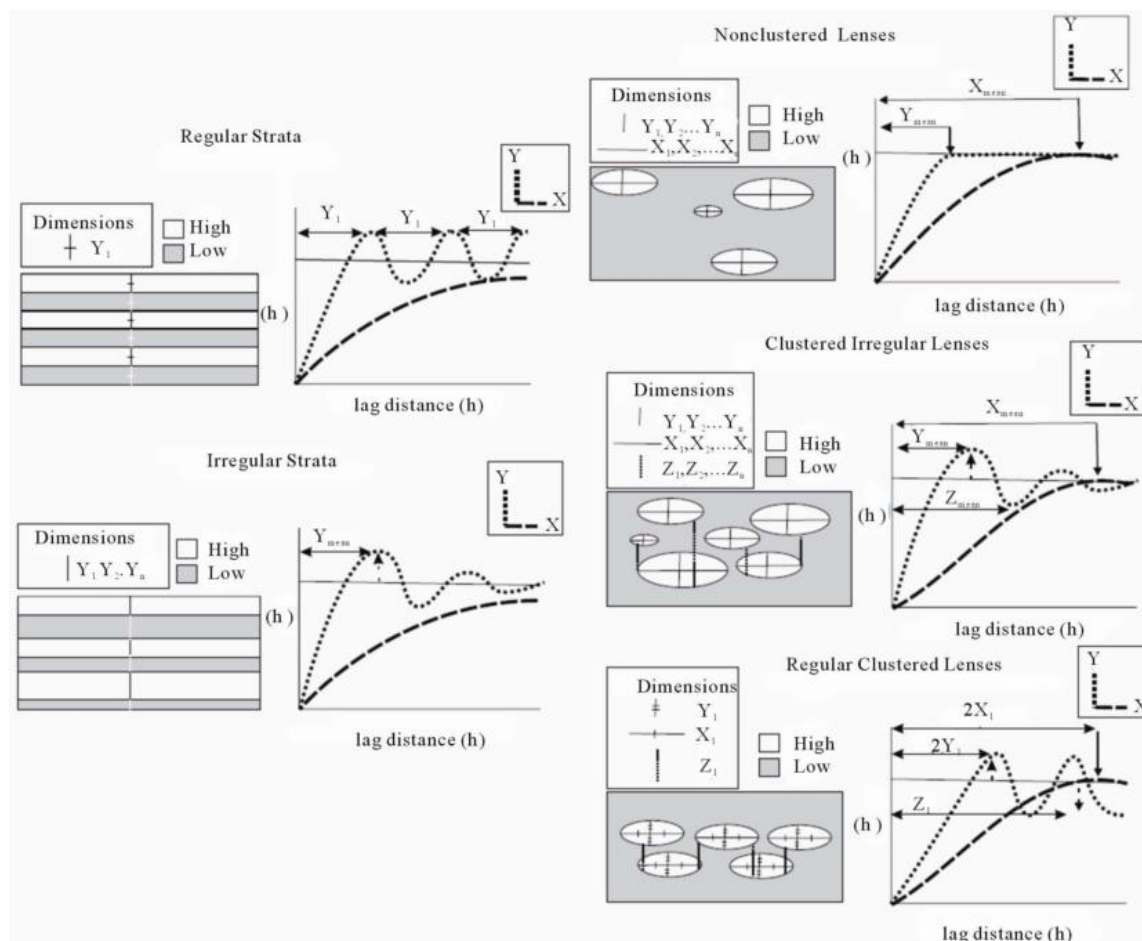


Fig. 2.4 variograms displaying different hole effect types for different geological formations. Dashed line represents the variogram of the X-direction, dotted line represents the variogram of Y-direction, solid horizontal line represents the sill. White areas represent high values of the attribute of interest and grey areas represent low values. Figure retrieved from Amanipoor (2013).

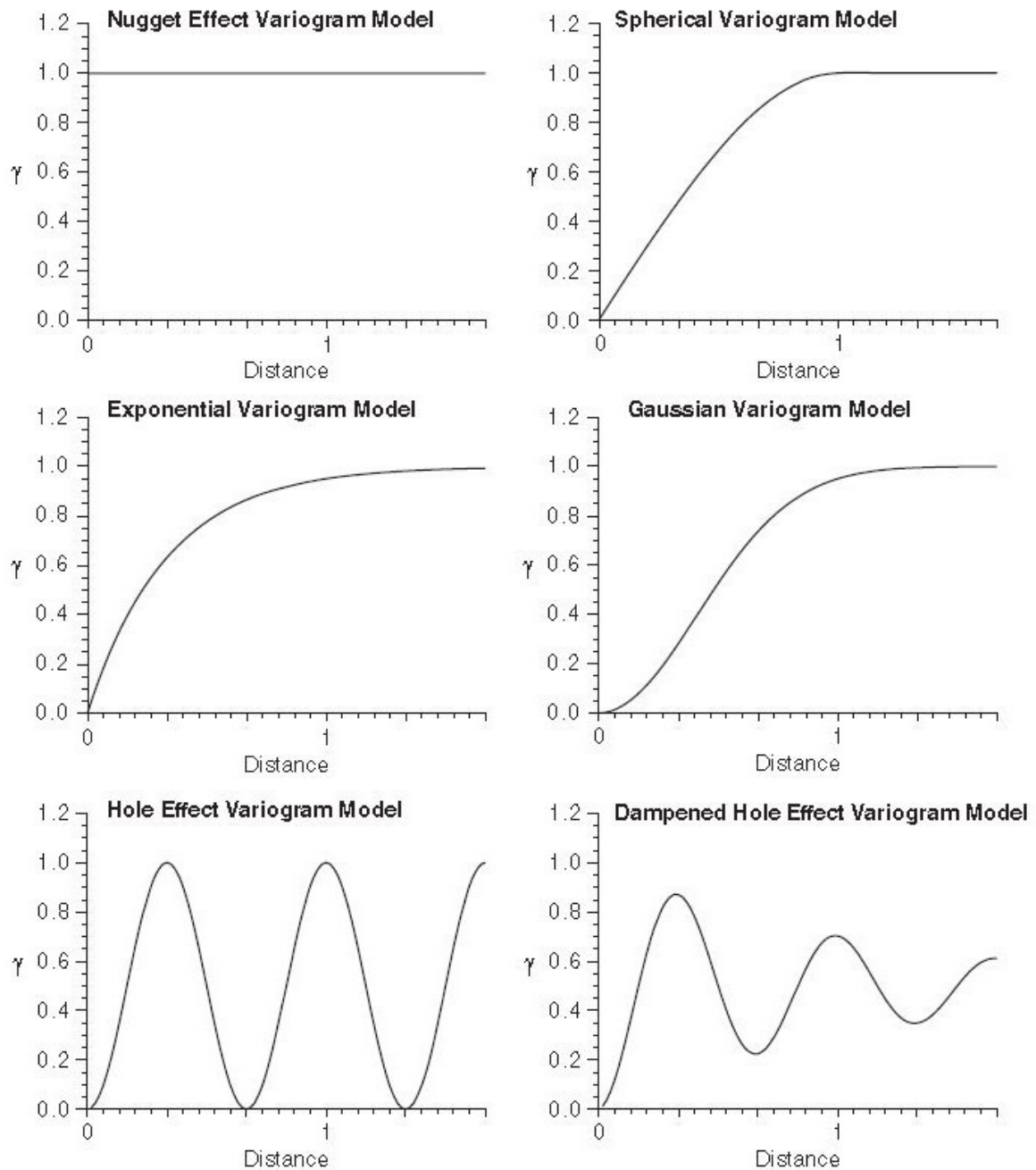


Fig. 2.5 Different types of theoretical variogram models. Variance values are normalized. Figure retrieved from Pyrcz and Deutsch (2014).

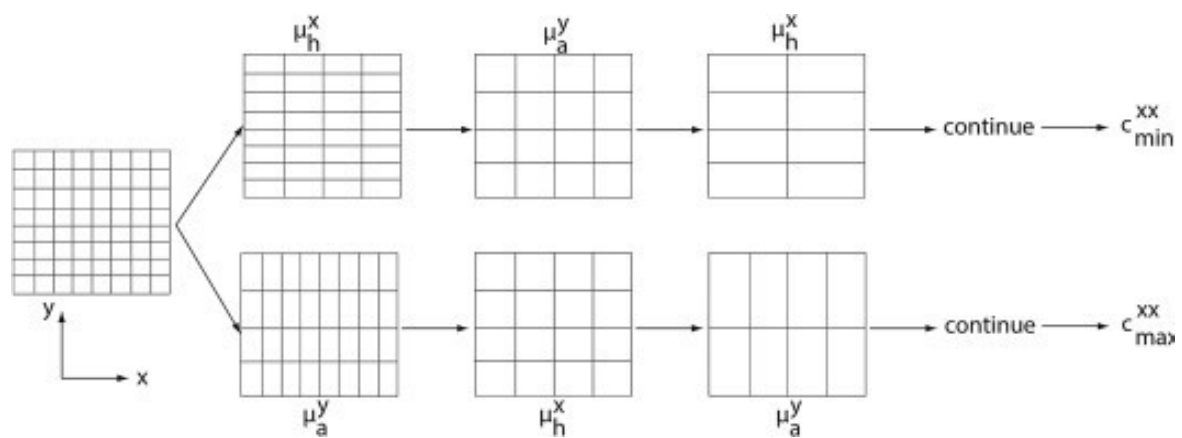


Fig. 2.6 Visualization of the Simplified Renormalization upscaling method, applied on a 2D plane. The image also describes how equivalent permeability depends on successive averaging order. Figure retrieved from Mahmud et al. (2015).

Chapter 3

Data Description

The primary step to geostatistical studies is data description and analysis. This procedure allows for a clear and complete view of the problem at hand. Data description includes visualization of data using color indices with either 2D surfaces like contour or section plots, or 3D models with the ability to navigate through the different layers. Moreover, histogram and data distribution plots, as well as respective statistical moments determination contribute to better understanding of the data.

For the purposes of this thesis, the 10th SPE benchmark reservoir model was used. The available dataset of the model is divided into four groups, one for porosity values, hereinafter referred to as *Phi*, and three for permeability, one for each principal direction, hereinafter referred to as *PermX*, *PermY* and *PermZ*. Porosity values range from 0–0.5 or 0–50%, while permeability values range from 6.65e-08–20000mD. Due to the nature of permeability as a petrophysical property, data are better treated and understood after applying logarithm. This specific treatment method is justified in Subsection 3.1.1. Moreover, the model consists of two distinct formations and as such, each formation is studied separately.

3.1 Tenth SPE Model

The 10th SPE benchmark reservoir model is a fine grid geological model, originally created as part of the PUNQ project and was initially meant to be used in upscaling projects. The model has a simple orthogonal geometry, with no top structure or faults being present. The model dimensions are 1200ft–by–2200ft–by–170ft, while a single fine scale cell has dimensions 20ft–by–10ft–by–2ft. In total, the fine scale grid has a size of 60–by–220–by–85 cells (1122000 cells). The coordinate system is orthogonal, with X for width, Y for length and Z for height of the model. The top 70ft (35 layers– 462000 cells), represent a Tarbert formation,

while the bottom 100ft (50 layers– 660000 cells), represent an Upper Ness formation (SPE, 2000).

Permeability shows large variation of about 8–12 orders of magnitude, with significant differences in the distribution types between the upper and lower layers. It is notable that no single statistical moment, like the arithmetic, harmonic or geometric average, is able to represent the effective permeability of the different layers. However, the latter is bounded by the arithmetic and harmonic means of the permeability distribution function (Masihi et al., 2016).

3.1.1 PUNQ Project

The model is a part of the PUNQ Complex Model, a half synthetic made up field. The Model's structure is based on Beatrice Field near the north east coast of Scotland, it was designed as a stratigraphic analogue of a Brent-type field and its properties were generated by algorithms developed by Norwegian Computing Center. The Brent sequence resembles the ones found in most North Sea UKCS fields and has a total thickness of 656ft (200m) plus some additional feet occupied by underlying and overlying shales. The Brent group is divided in five formations from bottom to top, the Broom, Rannoch, Etive, Ness and Tarbert formation (Vollset and Dore, 1984). Subsequently, the Ness formation is divided into three distinct parts, lower, middle and upper. The division of the Brent group into five formations reflects the regressive–transgressive cycle. An important note is that the 3D geomodel was based on well observations (Bos and project team, 1999).

The code used for the subsequent stochastic simulation of porosity and permeability, constitutes a subset of the GRUS project (Lia et al., 1997). The stochastic model treated each zone separately. Porosity was modelled by Gaussian random fields with trends in expectation, while for permeability, log–Gaussian fields with log–transformed data were used. In particular, they were generated by sequential Gaussian co–simulation and back–transformation of the associated normal score values. Furthermore, heterogeneous layers were also derived from Gaussian random fields. Only vertical trends were used, describing the change of the mean value as a function of depth, while horizontal correlation was chosen by experience. In order to simulate the fluvial formation lithology, a marked point process was used to distribute the channel systems. The channels were distributed until global criteria, like the net–to–gross ratio, were satisfied (Bos and project team, 1999).

3.1.2 Tarbert Formation

This formation represents a prograding near-shore environment, coarsening upward, offlapping sequence (Christie and Blunt, 2001; SPE, 2000), possibly in part reworked delta plain deposits. The sedimentary sequence is similar to the Rannoch and Etive formations but with a different depositional setting. It consists of grey to brown relatively massive fine to medium grained sandstone with subordinate thin siltstone, shale and coal beds and some calcareous bands. The base of the formation lies at the top of the last fining upward unit of the Ness formation, which is either an argillaceous bed or a coal bed. The geological age is Bajocian to Bathonian. (Vollset and Dore, 1984).

As far as flow properties are concerned, the formation divides practically into permeable sand facies and low-permeable shale and coal facies. The main two lithologies are barrier sands and lagoonal clays, in about equal proportions. No significant trends are present, although indications of lateral trends are evident. The formation has a thickness of about 115ft (35m). Porosity is assumed to follow a normal distribution with typical values around 25–30%, while permeability follows a log-normal distribution with values around 1–10 Darcies respectively. Further information on the modelling formulation of porosity and permeability distributions can be found in the final report of the PUNQ Complex Model project (Bos and project team, 1999).

3.1.3 Upper Ness Formation

The Ness formation is described as a fluvial system made of well sorted highly permeable long correlation anastomosed sandstone channels, imposed on a low-permeable background of shales and coal (Masihi et al., 2016). It consists of a heterolithic sequence of interbedded very fine to medium sandstones, shales, mudstones, siltstones and coals, deposited in a delta-top setting and includes a wide range of subgroups, like lagoonal muds, distributory channels, levees, mouth bars and lagoonal shoals. The formation is divided in three parts, a lower interbedded unit called the Lower Ness, the middle part called Mid-Ness shale and an upper sandstone unit called the Upper Ness. Only the Lower and Upper Ness parts are considered as appropriate reservoir units. The Ness formation represents the last part of the primary phase of northward progradation of the Brent delta and the onset of its retrogradation. Finally, the geological age of the formation is Bajocian (Glennie, 1998; Vollset and Dore, 1984).

Common features of this formation are coarsening and fining upward sequences, as well as small scale cross-bedding, horizontal bedding and synsedimentary deformation. The shales are silty, fissile and frequently pyritic, while there are also some indications of marine

influence. The upper contact with the massive cleaner sandstone of the overlying Tarbert formation may consist a minor disconformity (Vollset and Dore, 1984). Due to the high heterogeneity of the formation, it can be characterized as a labyrinth type reservoir. All three parts of the formation have a total thickness of 328ft (100m). The Mid-Ness shale is an impermeable layer about 33ft (10m) thick, lying approximately in the middle of the total thickness of the formation. Typical porosity values for the channels are about 20–30% and permeability values about 1–2 Darcies, while the background has low and insignificant flow properties, as explained previously. Thorough information on the modelling procedure of porosity and permeability distributions can be found in the final report of the PUNQ Complex Model project (Bos and project team, 1999).

3.2 Visualisation of Data

Using the program *Slice-o-Matic* in *Matlab* environment (Ludlam, 2001), several images of the model were captured for different layers and are presented in the following Figures. Due to the program's notation X and Y axis refer to the length and width of the model respectively, as opposed to the general notation of this thesis. In all data groups the heterogeneity of the Tarbert formation, as well as the anastomosed channels of the Upper Ness formation are clearly visible. Furthermore, the resulting images for all data groups are similar in shape and structure, whereas permeability on X and Y direction are almost identical. Another important observation is that the channel width and occupied area decreases with increasing layer height. In addition, the position of the channels is not fixed, but varies for each layer. A 3D perspective for each one of the four properties is presented in Figures 3.1a through 3.1d. Low values are denoted by blue color, increasing to red color. The individual formation layers are further described in the following Subsections.

3.2.1 Tarbert Formation

The heterogeneous structure of the Tarbert formation is visible throughout the whole height of the formation. Generally, there is a big variation in porosity and permeability both in value and in spatial distribution. An important notice is that low and high porosity areas coincide with low and high permeability areas respectively. Indicatively, layers 1 and 17 appear in Figures 3.2 and 3.3. Layer 35, which is the top of the formation, appears in Figure 3.1. Low values are denoted by blue color, increasing to red color.

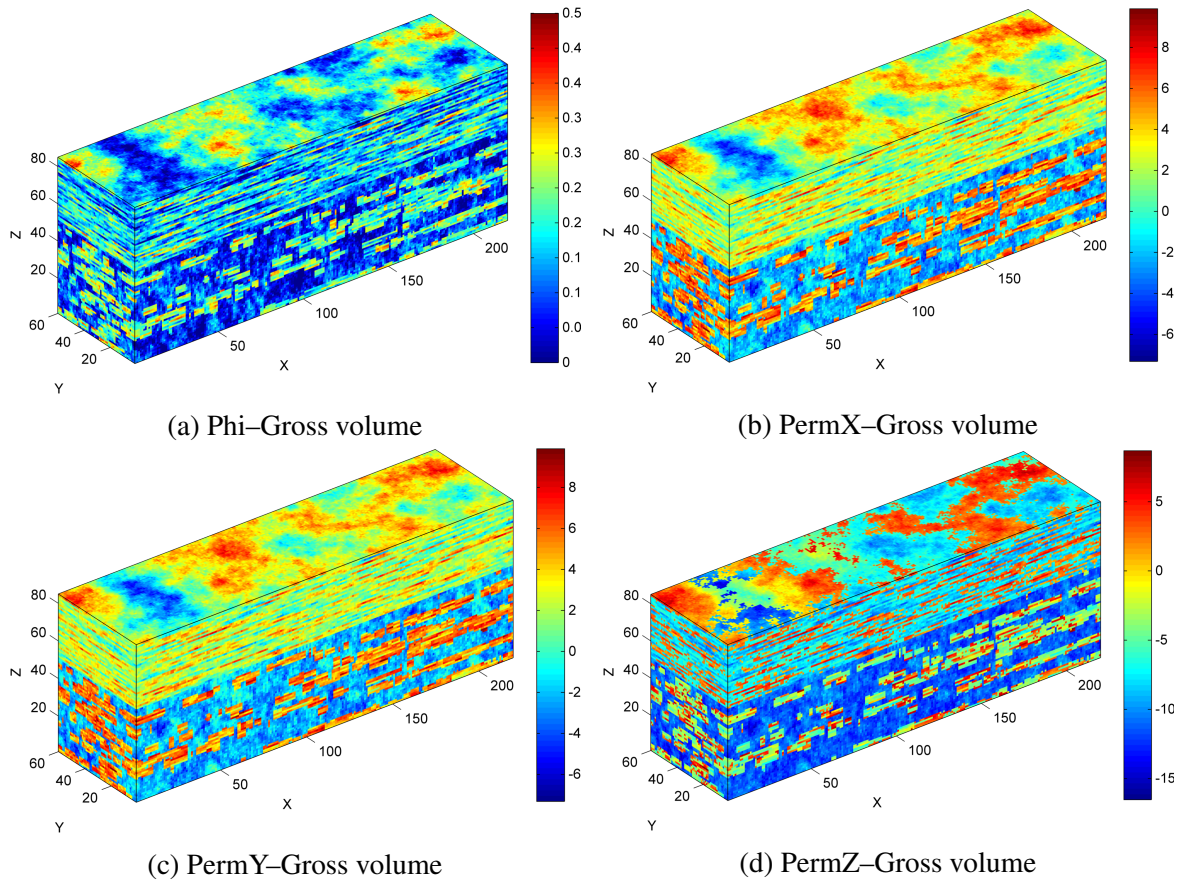


Fig. 3.1 Visualisation of the 3D perspective of porosity and permeability data.

3.2.2 Upper Ness Formation

The variation of channel distribution is clear throughout the height of the formation. The channels extend parallel to the length of the model and their structure changes on each layer. As height increases, the channels occupy even less area of the respective layer. The permeability of X and Y direction are almost identical for this formation as well. Indicatively, layers 1, 20, 35 and 50 appear in Figures 3.4 through 3.7. Low values are denoted by blue color, increasing to red color.

3.3 Exploratory Data Analysis

For each formation, the statistical moments for porosity and permeability values were calculated. Subsequently histograms were constructed and the best fit probability distribution was determined, using the *Distribution Fitting Tool* in *Matlab* environment. Finally, scatter plots using porosity and permeability data were built, in order to acquire an image of the

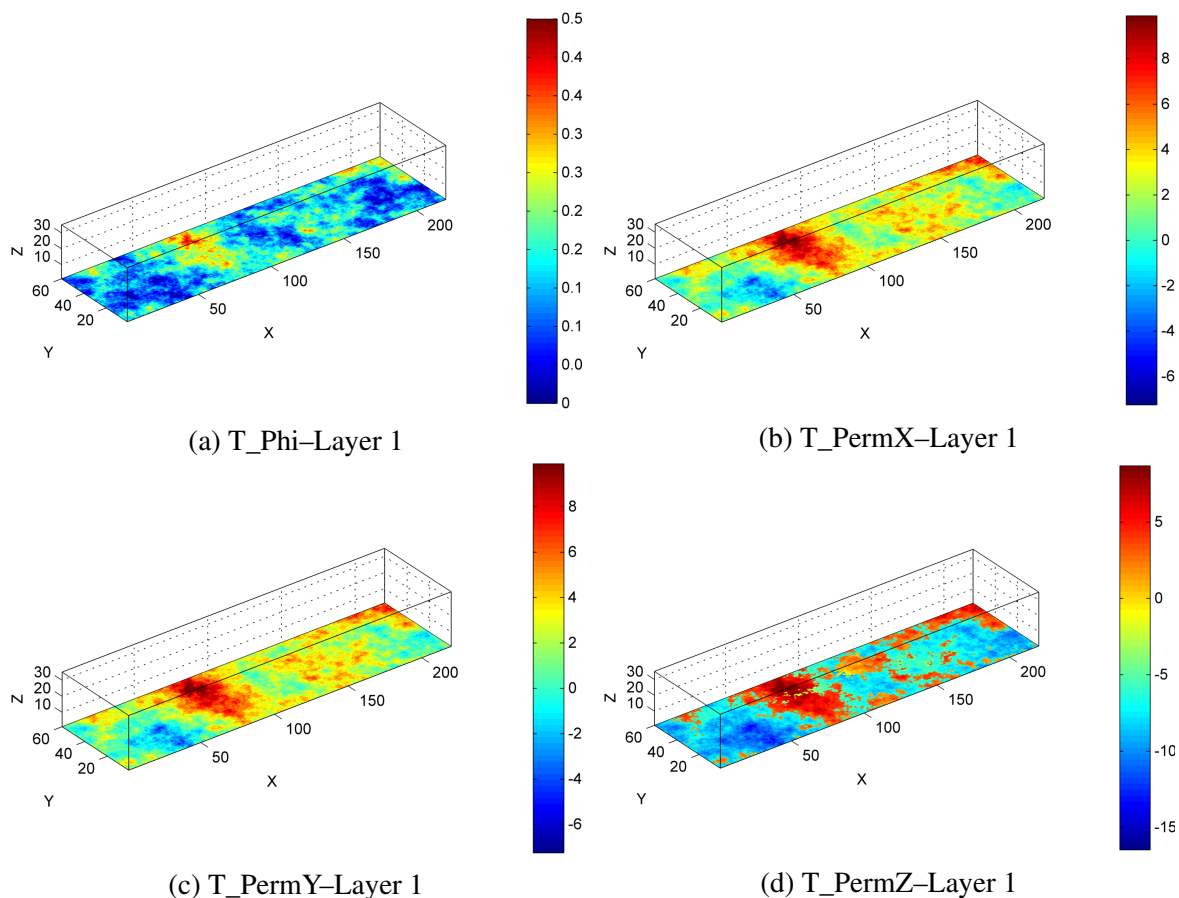


Fig. 3.2 Visualisation of porosity and permeability data of the first (bottom) layer of the Tarbert formation.

correlation between each pair of properties. The results are summarized in the form of Tables and Figures. It is important to constantly keep in mind that permeability data were used only after applying logarithm to the original data, unless it is specifically stated otherwise.

3.3.1 Tarbert Formation

To begin with, the statistical moments were calculated and are presented in Table 3.1. Porosity appears in decimal representation and permeability is expressed in miliDarcies (mD). After that, the construction of the histogram and fitting with the proper distribution function was carried out. The respective histograms are represented in Figures 3.8a through 3.8d, while the numerical results of the fitting appear in Table 3.2. Finally, the respective scatter plots are presented in Figures 3.9a through 3.9c.

According to Table 3.2, porosity follows a normal distribution, while permeability follows a log-normal distribution, considering that logarithm has already been applied to permeability

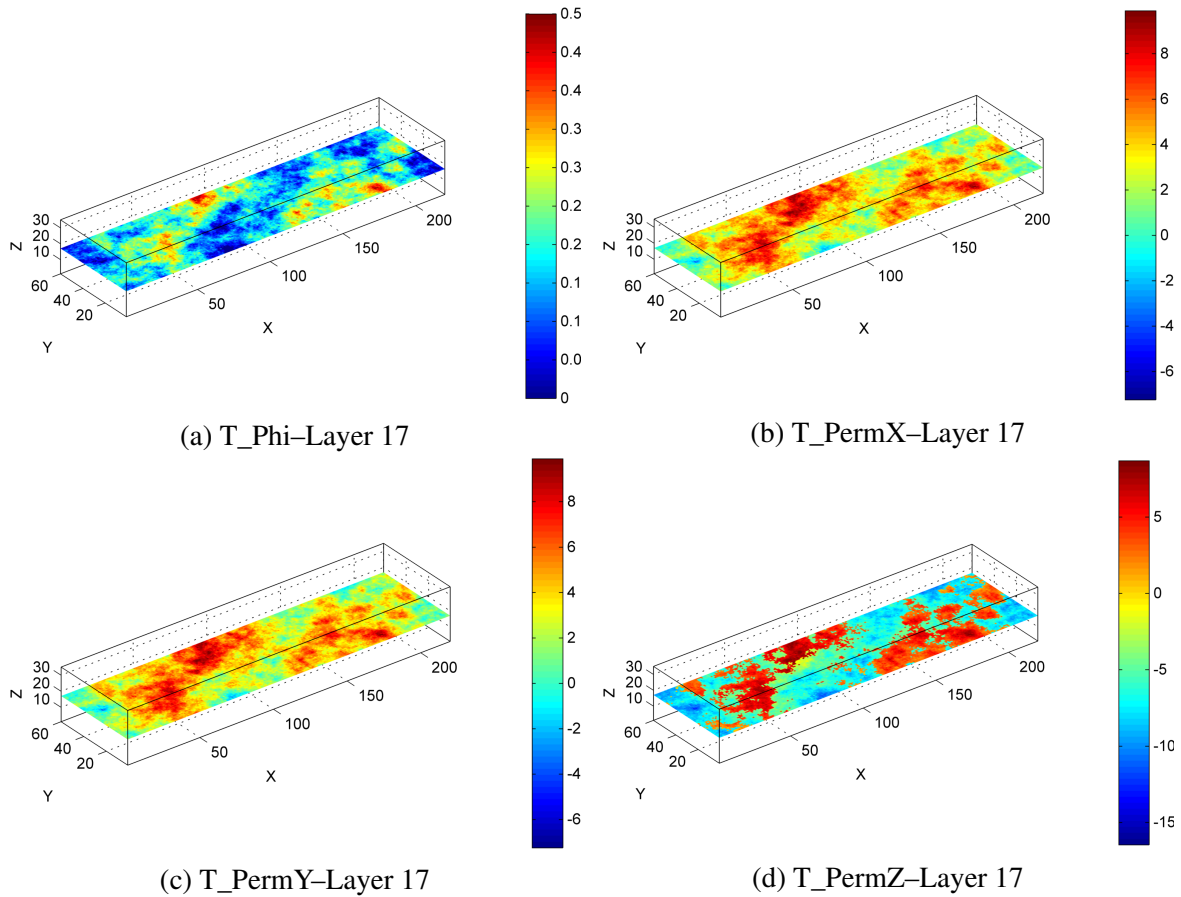


Fig. 3.3 Visualisation of porosity and permeability data of the 17th layer of the Tarbert formation.

data. These observations fall in line with the PUNQ project modelling principles, described in Subsection 3.1.1. The multimodal non-parametric distribution appears to be a better fit to the Phi, PermX and PermY data, as displayed in Figure 3.8. A sufficient explanation is that, as described in the previous chapter, the multimodal distribution constitutes a combination of multiple normal distributions and in addition, it is best applied to discrete data. Thus, the data are still characterized by a normal and log-normal distribution respectively.

Permeability in Z-direction is characterized by a bimodal distribution. This suggests the existence of two distinct data groups with different degree of permeability, which can also be realized to a certain degree by observing the layer plots of the Tarbert formation. This behaviour is justified by the fact that sediments are usually distributed in a bimodal fashion and in addition to that, that layering leads to expect a bimodal distribution (Lake et al., 1991). Moreover, the lithology of the formation, which comprises of permeable and non-permeable facies, can also explain the bimodal distribution.

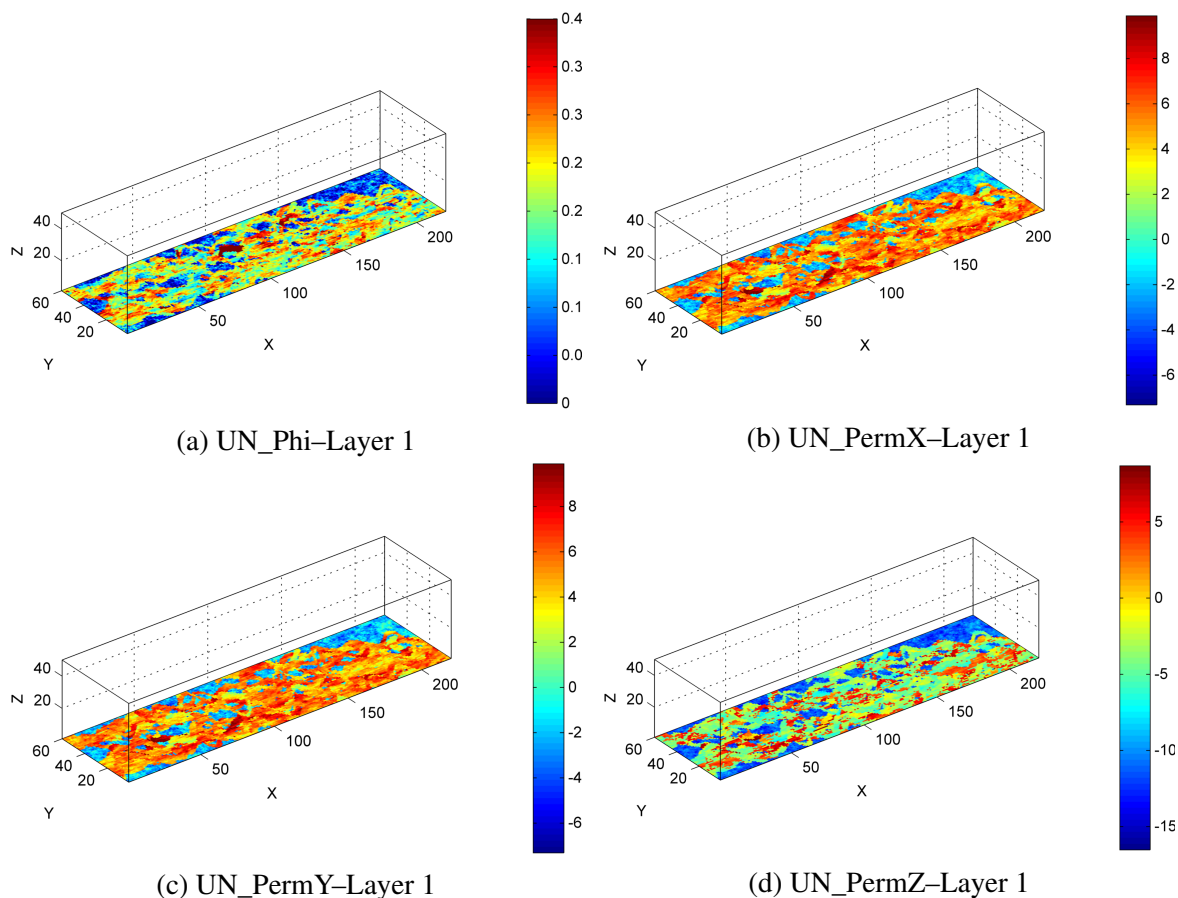


Fig. 3.4 Visualisation of porosity and permeability data of the first (bottom) layer of the Upper Ness formation.

The respective scatter plots indicate a positive strong relationship between porosity and permeability data, considering the shape of the data clusters, which tends to align with the diagonal (Rumsey, 2016). The scatter plot between porosity and permeability of Z-direction, appearing in Figure 3.9c, provides an additional indication about the two distinct data clusters, which cause the bimodal distribution of PermZ data.

Table 3.1 Tarbert formation statistical parameters. Porosity appears in decimal representation and permeability is expressed in miliDarcies (mD).

Data	Min	Max	Mean	Median	Mode	Variance	Skewness	Kurtosis
T_phi	0.0	0.5	0.19	0.19	0.0	0.0065	0.042	2.78
T_permX	7.13e-04	20000	356.49	25.38	20000	2.55e+06	9.139	99.5
T_permY	7.13e-04	20000	356.49	25.38	20000	2.55e+06	9.139	99.5
T_permZ	7.13e-08	6000	94.09	0.0042	6000	2.21e+05	9.407	104.81

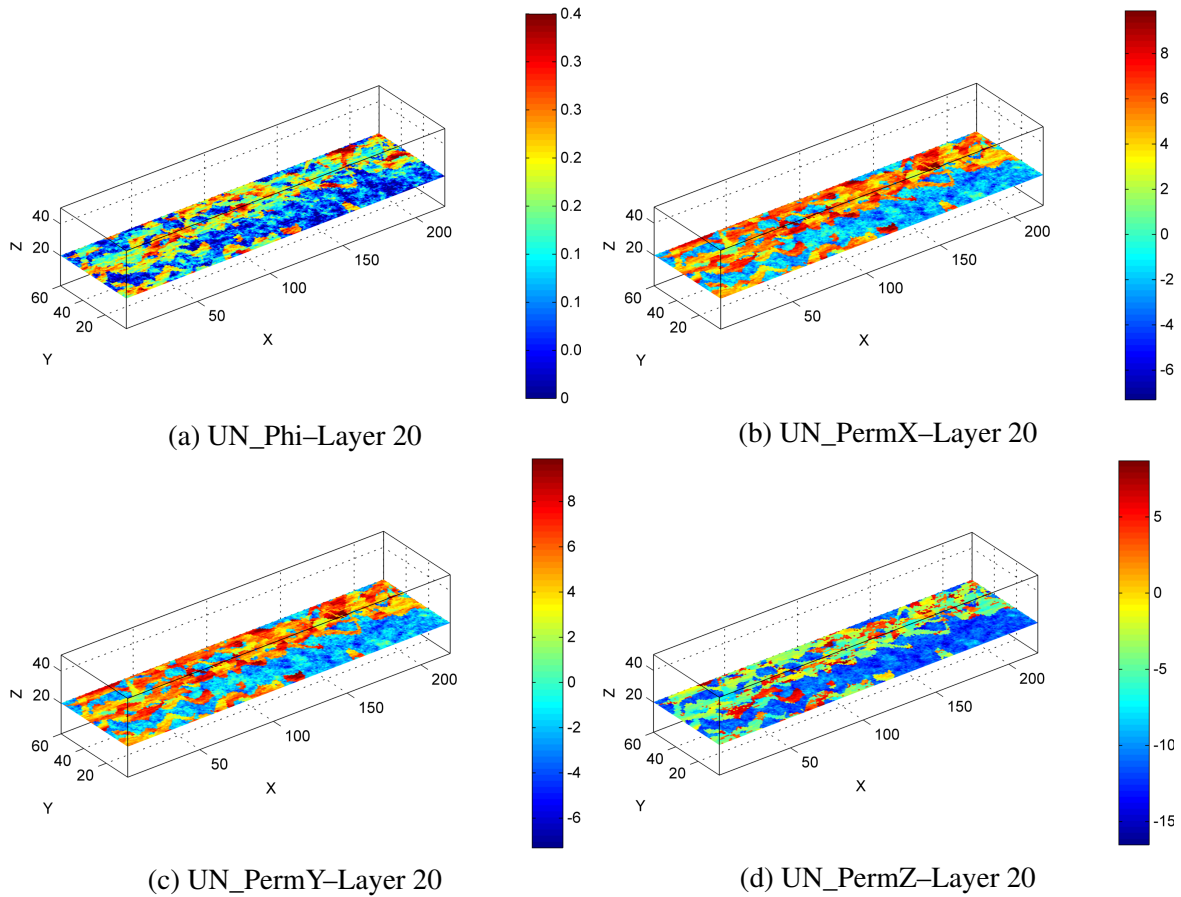


Fig. 3.5 Visualisation of porosity and permeability data of the 20th layer of the Upper Ness formation.

Table 3.2 Tarbert formation distribution parameters. The parentheses describe an alternative distribution fit. Porosity appears in decimal representation, permeability is measured in miliDarcies (mD) and data are analysed after applying logarithm.

Data	Distribution Type	Parameters
T_phi	Normal (Unimodal non-parametric)	$\mu=0.1908, \sigma^2=0.006527$ (bandwidth=0.0064)
T_permX	Normal (Unimodal non-parametric)	$\mu=3.258, \sigma^2=5.616$ (bandwidth=0.185)
T_permY	Normal (Unimodal non-parametric)	$\mu=3.258, \sigma^2=5.616$ (bandwidth=0.185)
T_permZ	Bimodal non-parametric	bandwidth=0.364

3.3.2 Upper Ness Formation

Once again, the statistical moments were calculated and are presented in Table 3.3. Porosity appears in decimal representation and permeability is expressed in miliDarcies (mD). Subse-

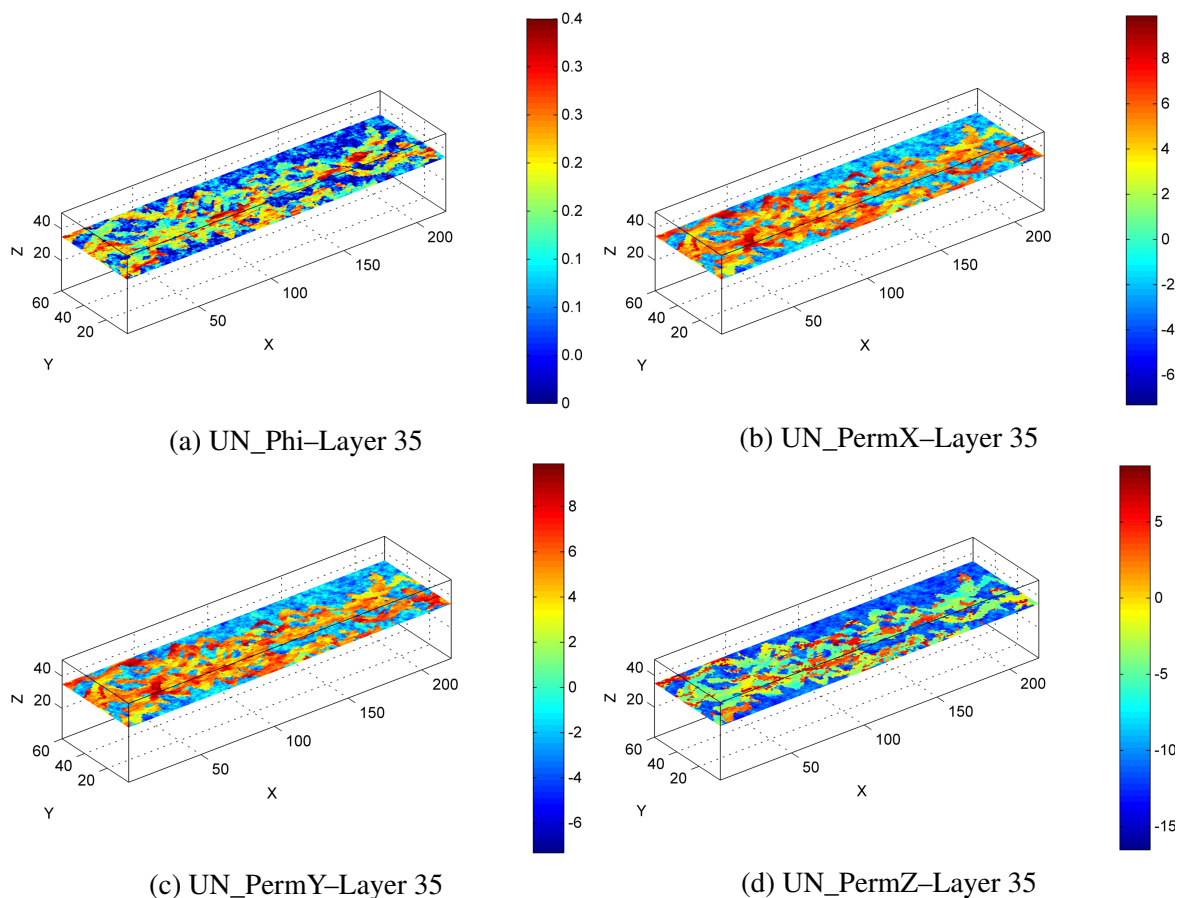


Fig. 3.6 Visualisation of porosity and permeability data of the 35th layer of the Upper Ness formation.

quently, the construction of the histogram and fitting with the proper distribution function was carried out. The histograms are represented in Figures 3.10a through 3.10d, while the numerical results of the fitting appear in Table 3.4. The respective scatter plots are presented in Figures 3.11a through 3.11c.

In this case, Phi, PermX and PermY, all display bimodal distributions, with the only difference being that for porosity the two data groups are not very distinct. This can be easily explained by the fact that the lithology of the Upper Ness formation comprises of two very distinct groups, the permeable channels and the non-permeable background. However, the distribution of PermZ displays an additional peak. This can be justified by the existence of the permeable channels and non-permeable background, combined with the effect of layering (Lake et al., 1991). As already mentioned, the multimodal distribution results from combining multiple normal distributions, meaning that the formation is locally characterized by normal distributions. Thus, the result falls once again in line with the modelling principles described in Subsection 3.1.1.

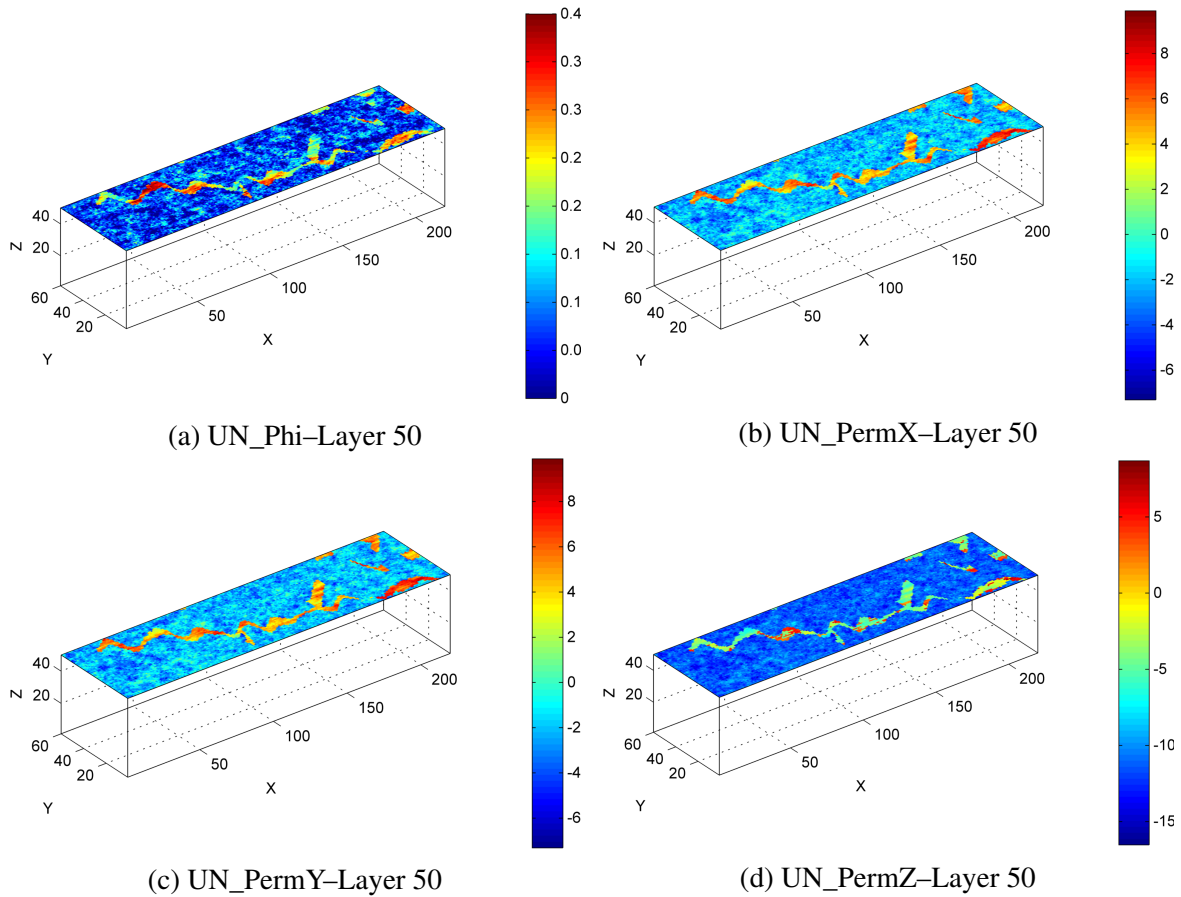


Fig. 3.7 Visualisation of porosity and permeability data of the 50th layer (top) of the Upper Ness formation.

The respective scatter plots appearing in Figures 3.11a through 3.11c display a positive, however not very strong relationship, as the data are not so strictly aligned with the diagonal (Rumsey, 2016). In all three plots the respective data clusters appearing in the histograms are obvious.

Table 3.3 Upper Ness formation statistical parameters. Porosity appears in decimal representation and permeability is expressed in miliDarcies (mD).

Data	Min	Max	Mean	Median	Mode	Variance	Skewness	Kurtosis
UN_phi	0.0	0.4	0.156	0.146	0.0	0.0097	0.252	2.032
UN_permX	6.65e-04	20000	354.96	7.193	20000	1.68e+06	9.264	114.49
UN_permY	6.65e-04	20000	354.96	7.193	20000	1.68e+06	9.264	114.49
UN_permZ	6.65e-08	6000	33.47	9.18e-04	2.0	5.65e+04	16.376	341.29

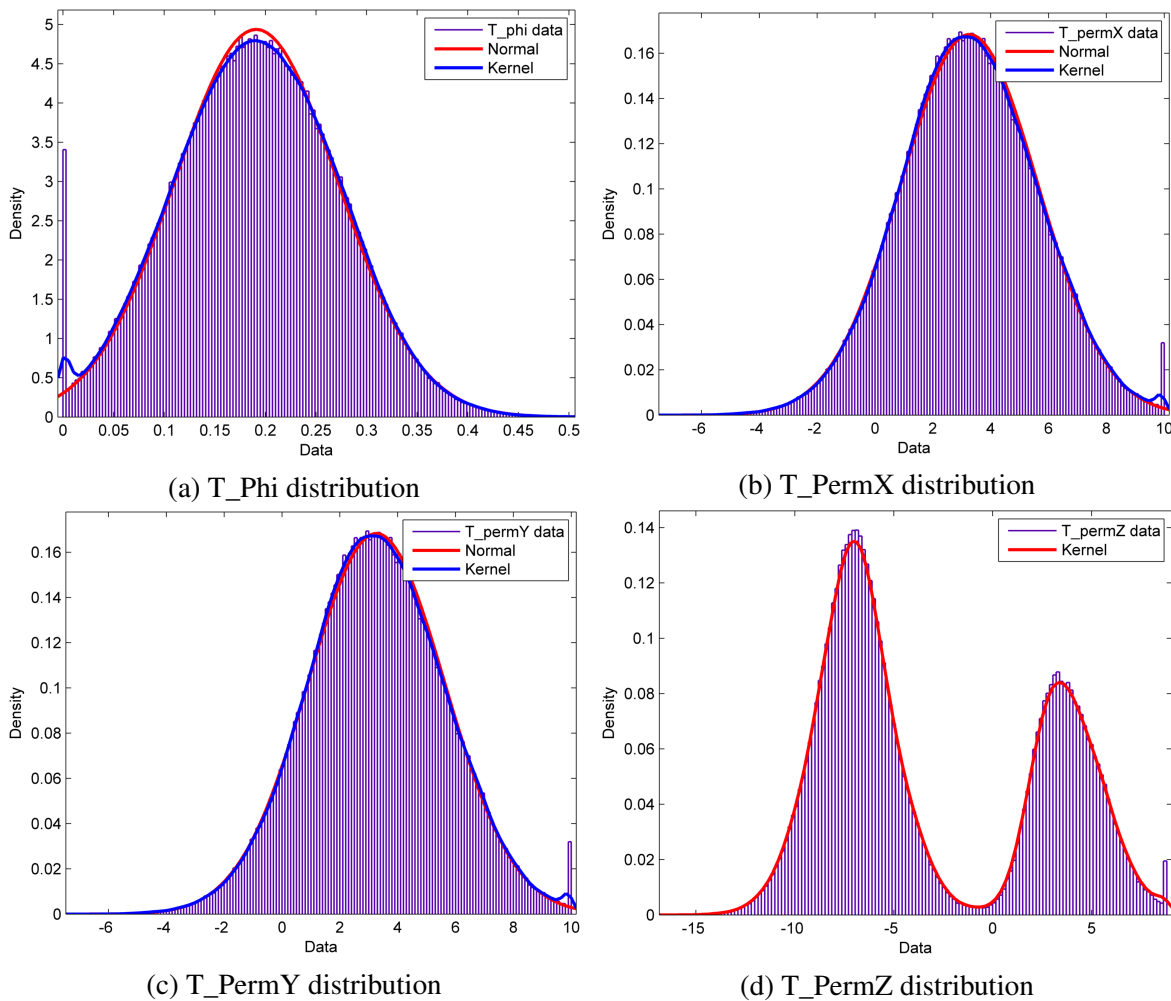


Fig. 3.8 Histograms and fitted PDFs of the respective data groups of the Tarbert formation. Permeability is measured in miliDarcies (mD) and data are analysed after applying logarithm.

Table 3.4 Upper Ness formation distribution parameters. Porosity appears in decimal representation, permeability is measured in miliDarcies (mD) and data are analysed after applying logarithm.

Data	Distribution Type	Parameters
UN_phi	Bimodal non-parametric	bandwidth=0.00872
UN_permX	Bimodal non-parametric	bandwidth=0.4108
UN_permY	Bimodal non-parametric	bandwidth=0.4108
UN_permZ	Trimodal non-parametric	bandwidth=0.4586

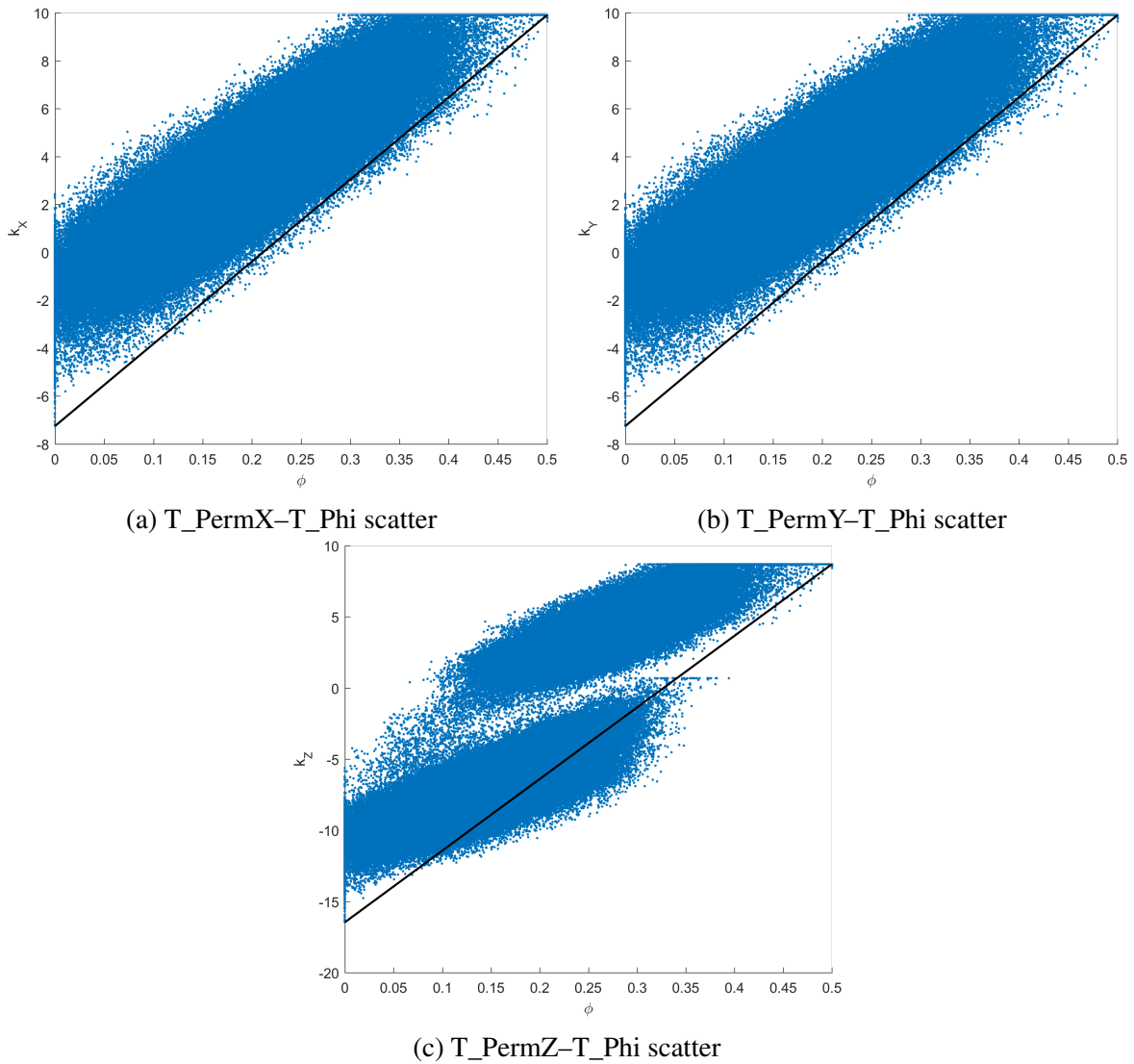


Fig. 3.9 Scatter plots between porosity and permeability data of the Tarbert formation. The respective data clusters are obvious. Permeability is measured in miliDarcies (mD) and data are analysed after applying logarithm.

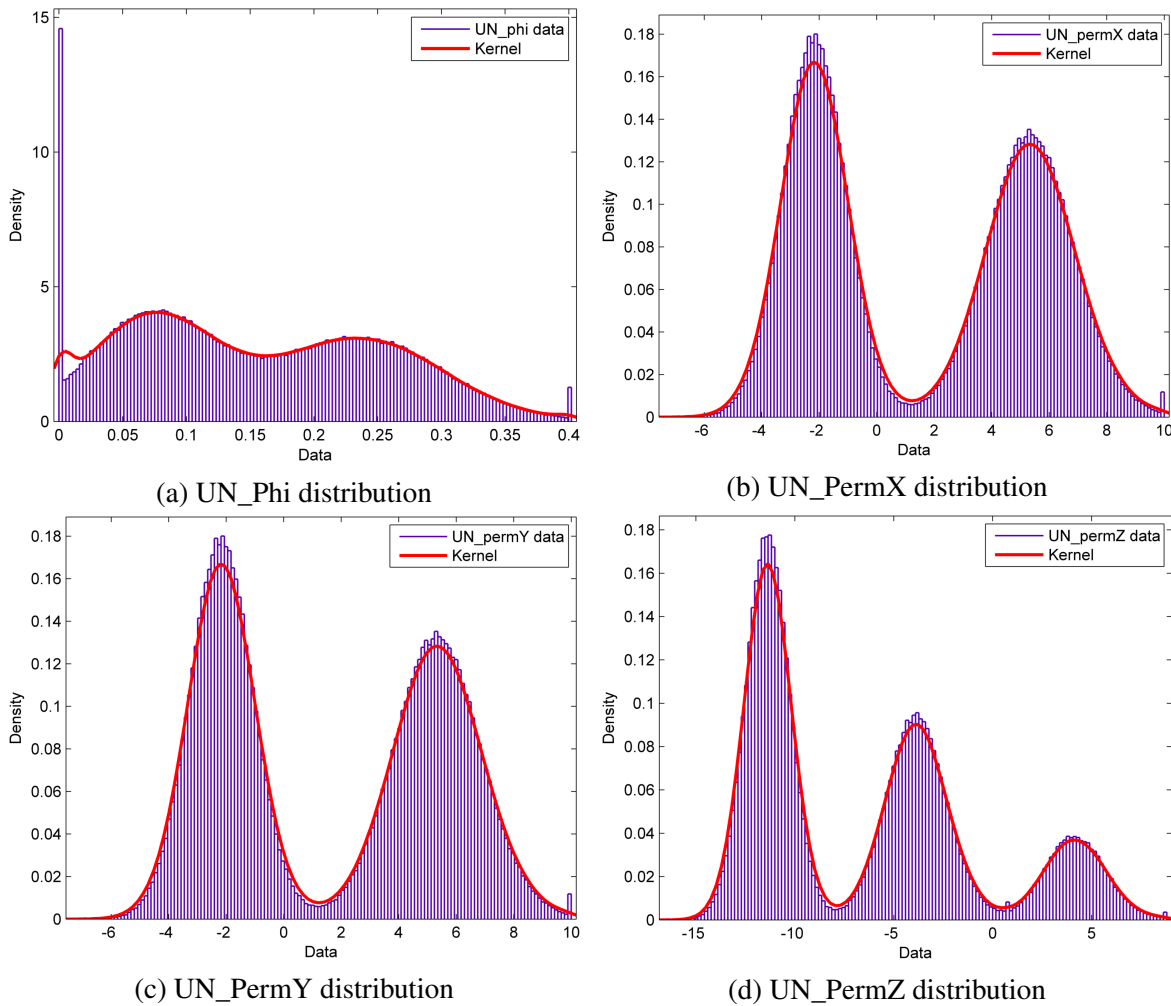


Fig. 3.10 Histograms and fitted PDFs of the respective data groups of the Upper Ness formation. Permeability is measured in miliDarcies (mD) and data are analysed after applying logarithm.

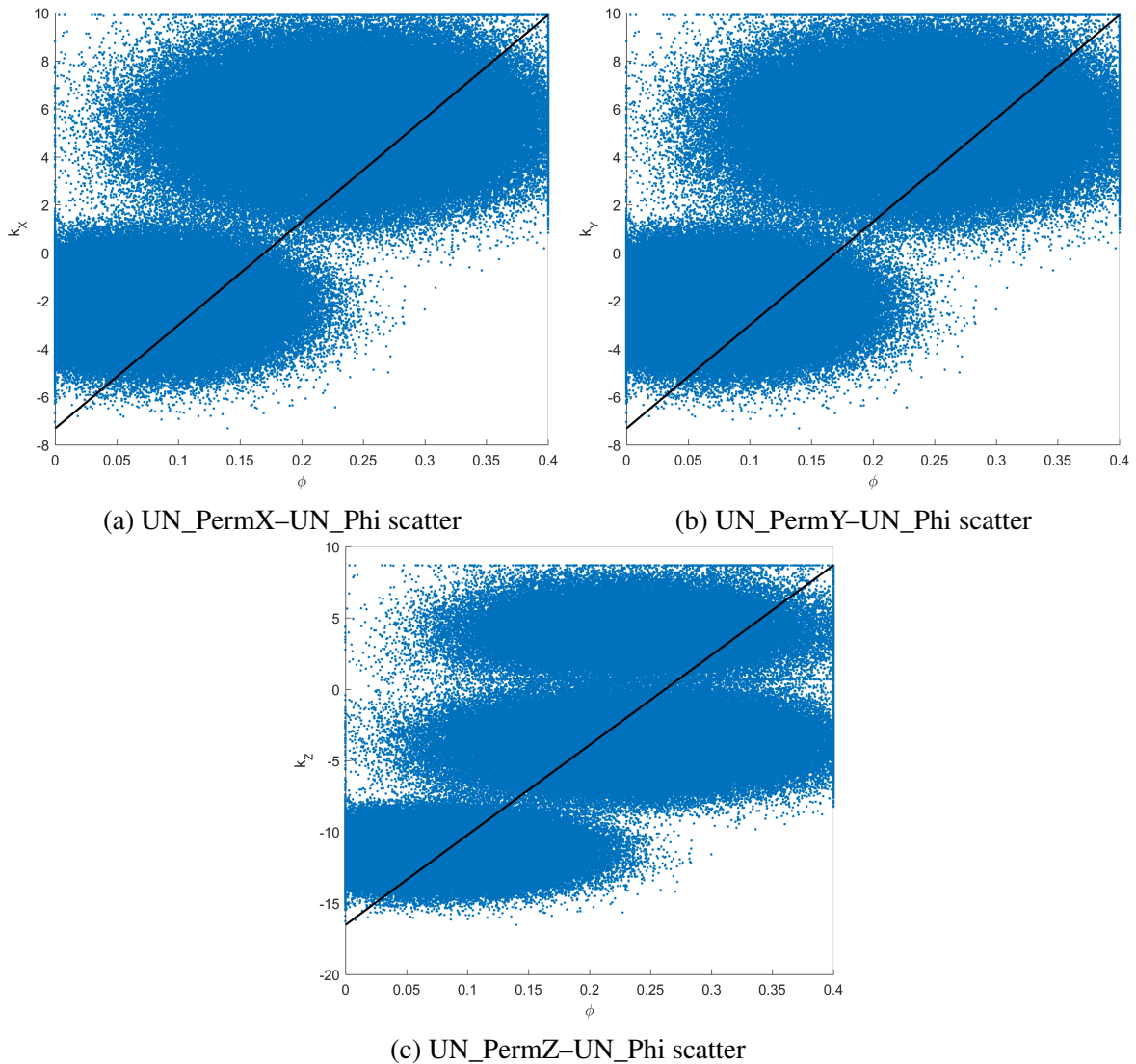


Fig. 3.11 Scatter plots between porosity and permeability data of the Upper Ness formation. The respective data clusters are obvious. Permeability is measured in miliDarcies (mD) and data are analysed after applying logarithm.

Chapter 4

Geostatistical Analysis

Exploratory data analysis is followed by geostatistical analysis. The aim of this step, also referred to as spatial modelling, is the construction of the experimental variogram and fitting it to an appropriate theoretical variogram model, which will be ultimately used in kriging procedures. Considering the two different formations, the analysis is once again carried out separately. It has to be pointed out in advance that, distance is expressed in number of cells, porosity ranges from 0 to 1 and permeability is measured in miliDarcies (mD), whereas data are analysed after applying logarithm, unless it is stated otherwise.

4.1 Variogram Analysis

Variography includes the derivation of the experimental variogram based on the different porosity and permeability data and the subsequent fitting to a theoretical variogram model. This analysis was executed considering data at various locations and directions, such that the results will be as objective as possible, while at the same time sufficient enough to be comparable against each other. The results are presented in the form of Figures and Tables, in order to give a clear image of the behaviour of each formation.

The different experimental variograms required for the analysis were derived using the program *Experimental (Semi-) Variogram* in *Matlab* environment (Schwanghart, 2008), while the variogram fitting was carried out using the program *Variogramfit* again in *Matlab* environment (Schwanghart, 2009).

4.1.1 Experimental Variogram

The simplest variogram calculated is the directional or marginal variogram in which, all points of interest lie on a single direction. For both formations, for each property and for each

direction, a set of 100 marginal variograms were constructed and combined and subsequently the mean variogram of the respective direction was derived. Finally, the mean variograms of the three different directions were plot together for a more summarizing image. Each one of these 100 marginal variograms corresponds to a single core sample, which includes all data points along the respective direction, i.e. 60 points for the X-direction (width), 220 for the Y-direction (length) and 35 or 50 respectively for the Z-direction (height). These 100 cores are parallel to each other and were retrieved from a rectangular 10-by-10 grid with equal intermediate distances.

Creating a 3D plot of multiple variograms for different azimuths across a plane gives rise to the anisotropic variogram. This plot provides important clues about the isotropy of the formation. A round anisotropic variogram suggests isotropic material, while an ellipsoidal anisotropic variogram indicates anisotropic material. Anisotropic variograms were calculated for different layers of both formations.

Another type of variogram that was calculated is the omnidirectional variogram, which takes into consideration all data pairs across a plane, irrespective of azimuth. This type of variogram, like the anisotropic variogram, is applied to horizontal planes, since sediments are deposited horizontally. Layers can acquire inclination but only due to tectonic events. In addition to that, both the the Tarbert and the Upper Ness formations display horizontal layering and thus a vertical omnidirectional variogram would be pointless.

Adding data from different layers to the omnidirectional variogram results in the 3D variogram. Although constructing this variogram based on a finite number of core samples would be more realistic, it was realized that such a method would result in indistinct variogram curves, thus introducing increasing difficulty and further complicating variogram interpretation. For this reason, the 3D variogram was calculated for four subvolumes of both formations. The first, basic subvolume, was a simple rectangular parallelepiped with dimensions 20-by-70-by-20 cells for the Tarbert and 20-by-70-by-30 cells for the Upper Ness formation, while the other three were modified versions of the basic subvolume, elongated on directions X, Y and Z respectively. Each one of these four subvolumes includes less than one quarter of the formation volume, where each quarter is produced by dividing the model in half across the X and Y-directions. A more clarifying image of the procedure appears in Figure 4.1 The model is approximately symmetrical along the Y-direction (with respect to the Y-Z plane), so such a partition is acceptable. The purpose of this partition is to not include the same points more than once in different variograms. This type of variogram takes into consideration data points irrespective of both azimuth and altitude and so, it is considered the most common variogram used in further spatial modelling procedures.

As data taken into consideration for variogram calculation increases, so does the required computational power and time. For this reason, for any data group used in each case, only a limited number of sampling points (or subsamples) was taken into consideration. It was observed that a number of 2000 subsamples would provide sufficient results, concerning the shape and smoothness of the variogram, as well as its other parameters. An indicative plot to support this observation appears in Figure 4.2. However, marginal variograms are an exception to this rule, since all respective data points were used for their calculation.

The set maximum correlation distance is split into several lag distance bins in order to construct each variogram. It was observed that increasing number of bins only affected the smoothness of the variogram curve but not the resulting parameter values, which are of main interest. Thus, keeping computational resources in mind, a number of 20 lag distance bins was deemed sufficient. The respective minimum lag distance is equal to the maximum correlation distance divided by the number of bins, i.e. $h = (maxdist)/20$. An indicative plot used to justify this decision appears in Figure 4.3.

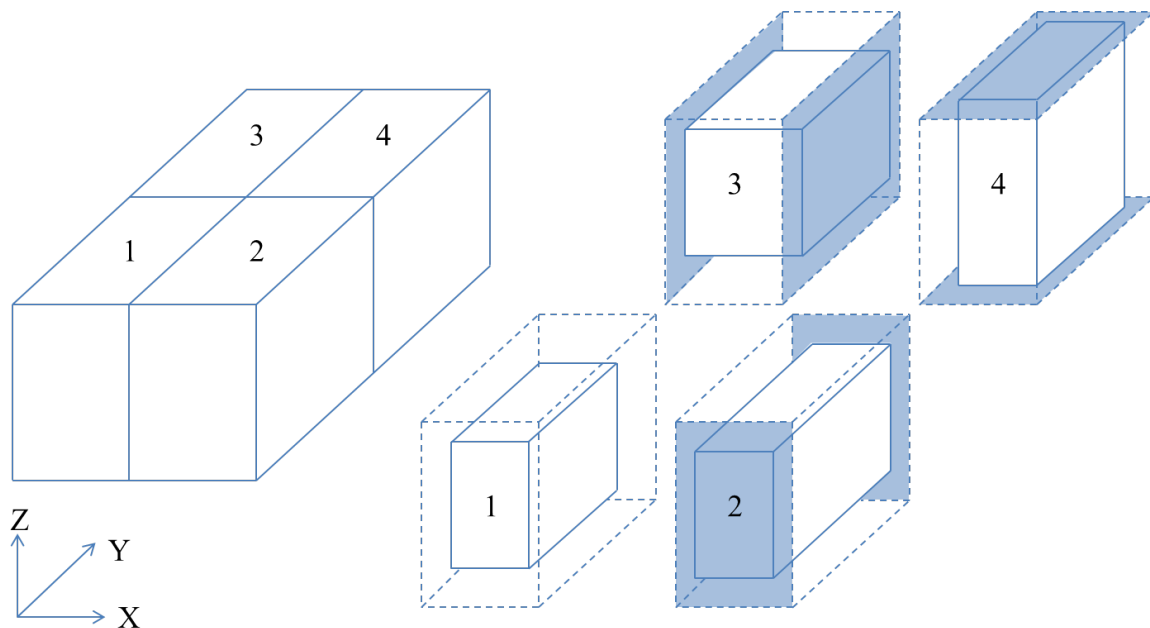


Fig. 4.1 Descriptive image of the partition of each formation and the four subvolumes used for calculating the 3D variograms.

Tarbert Formation

The marginal variograms for porosity and permeability on each of the three directions are presented in Figures 4.4 through 4.7. Each Figure represents 100 combined marginal

variograms, plot together with the mean variogram, for each principal direction, as well as the three mean variograms plot together for comparison. It is obvious that the sill displays a wide variation. Also, PermX and PermY show almost identical behaviour. Finally, the mean variogram of each Z-direction shows a rather noisy curve, in contrast with the corresponding X and Y-direction where the curve is smoother, for all four properties.

The anisotropic variograms for layers 1, 10, 20, 30 and 35 of all four properties are presented in Figures 4.8 through 4.12. The colour distribution of the top view, as well as of the more general 3D view indicates the degree of anisotropy of each layer. Anisotropic behaviour is obvious in all examined layers, with the exception of layer 35 of PermZ, which displays a lesser degree of anisotropy in comparison to the other variograms, as shown in Figure 4.12d. Furthermore, the general trend observed is that variance is increased along the X-direction of the model, compared to the Y-direction, for all layers with only a few exceptions.

The horizontal omnidirectional variograms for layers 1, 10, 20, 30 and 35 of all four properties are presented in Figures 4.13 through 4.17. All layers and properties are characterized by rather smooth variogram curves and small nugget. Once again PermX and PermY have similar behaviour. It is also noteworthy that PermZ displays a greater nugget in comparison to PermX and PermY, for all examined layers.

The derived 3D variograms appear in Figures 4.18 through 4.21. Subvolume 1 (basic) includes the cells X:6–25, Y:21–90, Z:11–30, subvolume 2 (elongated towards Y-direction) includes the cells X:36–55, Y:1–110, Z:11–30, subvolume 3 (elongated towards X-direction) includes the cells X:1–30, Y:131–200, Z:11–30 and finally, subvolume 4 (elongated towards Z-direction) includes the cells X:36–55, Y:131–200, Z:1–35. Porosity variograms reach the sill relatively faster than permeability variograms for subvolumes 1 and 2. However, for subvolumes 3 and 4 the respective variograms display similar behaviour, which leads to the conclusion that data are stronger correlated as length(Y) of the subvolume increases, rather than width(X) or height(Z).

Upper Ness Formation

The marginal variograms for porosity and permeability on each of the three directions are presented in Figures 4.22 through 4.25. Each Figure represents 100 combined marginal variograms, plot together with the mean variogram, for each principal direction, as well as the three mean variograms plot together for comparison. In this formation, the wide variation of the sill is obvious as well. Also, once more, PermX and PermY display very similar results. The mean variogram of Z-directions is not as smooth as that of X and Y-directions.

The anisotropic variograms for layers 1, 10, 20, 30, 40 and 50 of all four properties are presented in Figures 4.26 through 4.31. The colour distribution of the top view, as well as of the more general 3D view indicates the degree of anisotropy of each layer. Anisotropic behaviour is obvious in most examined layers, with only a few exceptions where there is a lesser degree of anisotropy. In this case as well, variance generally increases towards X-direction (width) of the model, compared to the Y-direction (length), for all layers.

The horizontal omnidirectional variograms for layers 1, 10, 20, 30, 40 and 50 of all four properties are presented in Figures 4.32 through 4.37. Most layers and properties display smooth variogram curves and relatively small nugget with a few exceptions. PermX and PermY show very similar behaviour.

The calculated 3D variograms appear in Figures 4.38 through 4.41. Subvolume 1 (basic) includes the cells X:6–25, Y:21–90, Z:11–40, subvolume 2 (elongated towards Y-direction) includes the cells X:36–55, Y:1–110, Z:11–40, subvolume 3 (elongated towards X-direction) includes the cells X:1–30, Y:131–200, Z:11–40 and finally, subvolume 4 (elongated towards Z-direction) includes the cells X:36–55, Y:131–200, Z:1–50. The variograms of each property for the same subvolume display fairly similar behaviour, which is mostly characterized by a large nugget, small range for subvolumes 2 and 4, and greater range for subvolumes 1 and 3. These observations suggest that a lot of noisy and uninterpretable in short distance data exist in the Upper Ness formation and also that correlation strengthens with increasing width(X) of the formation.

4.1.2 Theoretical Variogram Model

After the required experimental variograms have been derived they have to be fitted to the appropriate theoretical variogram models, in order to determine the required nugget, sill and range. Since the variogram models are expected to be further used in 3D modelling, it is pointless to fit any other than the 3D variogram. For that reason, indicatively, the experimental variograms of the first Subvolume of all four properties for both formations have been fit to an appropriate theoretical model.

The program used (Schwanghart, 2009) includes nine different possible theoretical models. Each variogram was tried out with all nine models and the best fit was determined using the *Coefficient of Determination* or R^2 of goodness of fit, which was calculated simultaneously by the program. This coefficient ranges from 0 to 1, while fitting quality improves as it reaches the unity (Magee, 1990). An indicative plot of porosity variogram fitting for the Tarbert formation appears in Figure 4.42, where the nine available models are displayed. Finally, the numerical results of R^2 are presented in summarizing Tables, while

the fitted 3D variograms, as well as the respective modelling parameters, are presented in Figures and Tables for both formations.

Tarbert Formation

The 3D variogram of each property was fit to each one of the nine available models and the determination coefficients for each fit are summarized in Table 4.1. The Exponential model is the best fit to porosity, as well as permeability variograms, since it results in the determination coefficient closest to the unity. The fitted variograms are represented in Figures 4.43a through 4.43d, while the respective modelling parameters of interest, namely the nugget, sill and range, are presented in Table 4.2.

An initial observation is that all properties were best fitted with an Exponential model. Furthermore, PermX and PermY once again display similar behaviour. Last but not least, the displayed nugget is relatively small, while range varies for each property.

Table 4.1 Summarizing table of R^2 values derived from the fitting of the 3D variogram of first Subvolume to a theoretical model, for the Tarbert formation.

Data	Bilinear	Circular	Spherical	Pentaspherical	Exponential
T_phi	0.8961	0.925	0.9299	0.9354	0.9641
T_permX	0.9016	0.92	0.9276	0.9338	0.962
T_permY	0.8995	0.9181	0.9278	0.9365	0.9728
T_permZ	0.9194	0.9283	0.9334	0.9392	0.9717
Data	Gaussian	Whittle	Stable	Matern	
T_phi	0.9292	0.9561	0.9454	0.9561	
T_permX	0.8881	0.9389	0.9254	0.9389	
T_permY	0.8969	0.9518	0.9357	0.9518	
T_permZ	0.9324	0.9623	0.9502	0.9623	

Table 4.2 Variogram modelling parameters of the first Subvolume of porosity and permeability for Tarbert formation.

Data	Model	Nugget	Sill	Range
T_phi	Exponential	0.0016	0.0051	2.9327
T_permX	Exponential	1.4313	3.5207	7.4516
T_permY	Exponential	1.2209	3.7321	6.6353
T_permZ	Exponential	4.3938	26.1665	2.2036

Upper Ness Formation

The 3D variogram of each property was fit to the nine available models and the determination coefficients for each fit are summarized in Table 4.3. Based on these results, the best fit model for porosity is the Stable model, for permeability of X–direction the Gaussian and for permeability of both Y and Z–direction the Pentaspherical. The fitted variograms are presented in Figures 4.44a through 4.44d, while the respective modelling parameters of interest, namely the nugget, sill and range, are presented in Table 4.4.

The first observation is that not all properties fit best to the same theoretical model, which can be caused due to the high heterogeneity of the formation, or even due to the number of sampling points used. The estimated nugget ranges from small to moderate values, while the range seems to be close for PermY and PermZ, which were fitted to the same theoretical variogram model.

Table 4.3 Summarizing table of R^2 values derived from the fitting of the 3D variogram of the first Subvolume to a theoretical model, for the Upper Ness formation.

Data	Bilinear	Circular	Spherical	Pentaspherical	Exponential
UN_phi	0.9838	0.9871	0.99	0.9921	0.9878
UN_permX	0.9853	0.9896	0.9922	0.9939	0.9798
UN_permY	0.9863	0.9924	0.9947	0.9962	0.9887
UN_permZ	0.9781	0.9815	0.9843	0.9859	0.9756
Data	Gaussian	Whittle	Stable	Matern	
UN_phi	0.9928	0.994	0.9958	0.994	
UN_permX	0.9944	0.9878	0.9929	0.9878	
UN_permY	0.9953	0.9925	0.9958	0.9925	
UN_permZ	0.9839	0.9795	0.9839	0.9795	

Table 4.4 Variogram modelling parameters of the first Subvolume of porosity and permeability for Upper Ness formation.

Data	Model	Nugget	Sill	Range
UN_phi	Stable	0.003	0.0063	2.9889
UN_permX	Gaussian	6.3982	9.2346	3.7273
UN_permY	Pentaspherical	3.1547	12.0522	8.2222
UN_permZ	Pentaspherical	13.4164	20.812	7.9973

4.2 Upscaling

In order to carry out the upscaling of permeability of the model, Simplified Renormalization was applied in combination with Wiener bounds, to determine the minimum and maximum equivalent permeability of the upscaled model. The procedure included the successive averaging of cell pairs along X, then along Y and finally along Z–direction in an iterative manner. Cells parallel to the flow direction were arithmetically averaged, otherwise if they were in series with respect to the flow they were harmonically averaged. More specifically, for PermX harmonic averaging was applied along X–direction, for PermY along Y–direction and for PermZ along Z–direction. Especially for upscaling porosity, the same procedure was applied, however all values were arithmetically averaged. The upscaling algorithm is included in the Appendix. It has to be clarified that the algorithm utilized the original data without logarithm, which was only applied subsequently in order to study the corresponding statistical parameters.

For both formations and all four properties, the results of each iteration are presented in the form of 3D images of the model, histogram plots of the upscaled data and tables containing the respective statistical parameters and moments. For comparison, the fine grid parameters of all four properties have been described in detail in Chapter 3. It is remarkable that each iteration reduces significantly the number of grid blocks, about 8 times with each rerun.

4.2.1 Tarbert Formation

The results of each iteration are presented as follows, while the last iteration constitutes of a single equivalent value for each property. A total of eight iterations were required to reach the ultimate equivalent value. With each successive iteration data became coarser and the 3D images became more indistinct as expected. The multimodal distribution appears to be a better fit than the normal distribution to all respective data histograms.

1st iteration

The resulting model has dimensions 30–by–110–by–18 blocks (59400 blocks). Images of the model appear in Figures 4.45a through 4.45d. The range of upscaled data as well as the respective statistical moments are presented in Table 4.5. Finally, the resulting data histograms are displayed in Figures 4.46a through 4.46d, while the respective parameters of the fit distributions are summarized in Table 4.6. As expected, the general shape of the upscaled data distributions does not differ from the fine grid model, although in this case the

low permeability peak of PermZ data is smaller than the high permeability peak. The 3D images already seem more "pixelated" than the fine grid model images.

Table 4.5 Tarbert formation statistical parameters after the first iteration of upscaling. Porosity appears in decimal representation and permeability is expressed in miliDarcies (mD).

Data	Min	Max	Mean	Median	Mode	Variance	Skewness	Kurtosis
T_phi	0.0	0.4446	0.1909	0.1898	0.1366	0.0039	0.1019	2.7767
T_permX	0.0046	20000	311.62	36.69	20000	1.25e+06	8.0787	87.3584
T_permY	0.005	20000	321.07	38.08	20000	1.301e+06	7.9123	83.63
T_permZ	6.503e-07	6000	91.95	6.4612	6000	1.164e+05	7.782	81.3767

Table 4.6 Tarbert formation distribution parameters after the first iteration of upscaling. The parentheses describe an alternative distribution fit. Porosity appears in decimal representation, permeability is measured in miliDarcies (mD) and data are analysed after applying logarithm.

Data	Distribution Type	Parameters
T_phi	Normal (Unimodal non-parametric)	$\mu=0.1909$, $\sigma^2=0.0039$ (bandwidth=0.0076)
T_permX	Normal (Unimodal non-parametric)	$\mu=3.6573$, $\sigma^2=4.3658$ (bandwidth=0.2423)
T_permY	Normal (Unimodal non-parametric)	$\mu=3.6932$, $\sigma^2=4.3628$ (bandwidth=0.2425)
T_permZ	Bimodal non-parametric	bandwidth=0.4242

2nd iteration

The resulting model has dimensions 15-by-55-by-9 blocks (7425 blocks). Images of the model appear in Figures 4.47a through 4.47d. The range of upscaled data as well as the respective statistical moments are presented in Table 4.7. Finally, the resulting data histograms are displayed in Figures 4.48a through 4.48d, while the respective parameters of the fit distributions are summarized in Table 4.8. Once again the general shape of the upscaled data distributions remains the same and in addition, the low permeability peak of PermZ is significantly smaller. The 3D images get even more pixelated.

3rd iteration

The resulting model has dimensions 8-by-28-by-5 blocks (1120 blocks). Images of the model appear in Figures 4.49a through 4.49d. The range of upscaled data as well as the respective statistical moments are presented in Table 4.9. Finally, the resulting data histograms are displayed in Figures 4.50a through 4.50d, while the respective parameters of

Table 4.7 Tarbert formation statistical parameters after the second iteration of upscaling. Porosity appears in decimal representation and permeability is expressed in miliDarcies (mD).

Data	Min	Max	Mean	Median	Mode	Variance	Skewness	Kurtosis
T_phi	0.0506	0.3615	0.1909	0.1899	0.0506	0.0024	0.1158	2.799
T_permX	0.2194	12075	280.66	49.28	0.2194	6.643e+05	6.4707	55.811
T_permY	0.2137	11948	297.73	53.2907	0.2137	7.218e+05	6.2363	52.021
T_permZ	8.894e-06	3613.6	88.0107	11.9645	8.894e-06	6.645e+04	5.9451	47.493

Table 4.8 Tarbert formation distribution parameters after the second iteration of upscaling. The parentheses describe an alternative distribution fit. Porosity appears in decimal representation, permeability is measured in miliDarcies (mD) and data are analysed after applying logarithm.

Data	Distribution Type	Parameters
T_phi	Normal (Unimodal non-parametric)	$\mu=0.1909$, $\sigma^2=0.0024$ (bandwidth=0.0088)
T_permX	Normal (Unimodal non-parametric)	$\mu=4.0107$, $\sigma^2=3.1658$ (bandwidth=0.3118)
T_permY	Normal (Unimodal non-parametric)	$\mu=4.0752$, $\sigma^2=3.1648$ (bandwidth=0.3114)
T_permZ	Bimodal non-parametric	bandwidth=0.4035

the fit distributions are summarized in Table 4.10. The general shape of the upscaled data distributions remains the same and in addition, the low permeability peak of PermZ tends to flatten out. The 3D images get even more pixelated and resemble little of the fine grid image any more.

Table 4.9 Tarbert formation statistical parameters after the third iteration of upscaling. Porosity appears in decimal representation and permeability is expressed in miliDarcies (mD).

Data	Min	Max	Mean	Median	Mode	Variance	Skewness	Kurtosis
T_phi	0.0724	0.3025	0.1898	0.1869	0.0724	0.0015	0.162	3.0201
T_permX	0.5447	5885	226.31	57.238	0.5447	2.715e+05	5.0703	36.169
T_permY	0.866	5739.8	247.02	60.51	0.866	3.161e+05	4.8168	32.322
T_permZ	7.279e-05	1793.5	76.55	16.265	7.279e-05	3.259e+04	4.5094	27.878

4th iteration

The resulting model has dimensions 4-by-14-by-3 blocks (168 blocks). Images of the model appear in Figures 4.51a through 4.51d. The range of upscaled data as well as the respective statistical moments are presented in Table 4.11. Finally, the resulting data histograms

Table 4.10 Tarbert formation distribution parameters after the third iteration of upscaling. The parentheses describe an alternative distribution fit. Porosity appears in decimal representation, permeability is measured in miliDarcies (mD) and data are analysed after applying logarithm.

Data	Distribution Type	Parameters
T_phi	Normal (Unimodal non-parametric)	$\mu=0.1898$, $\sigma^2=0.00152$ (bandwidth=0.0096)
T_permX	Normal (Unimodal non-parametric)	$\mu=4.1656$, $\sigma^2=2.4303$ (bandwidth=0.3793)
T_permY	Normal (Unimodal non-parametric)	$\mu=4.2559$, $\sigma^2=2.4061$ (bandwidth=0.3794)
T_permZ	Bimodal non-parametric	bandwidth=0.4727

are displayed in Figures 4.52a through 4.52d, while the respective parameters of the fit distributions are summarized in Table 4.12. The general shape of the distributions remains the same and the low permeability peak of PermZ gets progressively smaller. The 3D images become vague at this point.

Table 4.11 Tarbert formation statistical parameters after the fourth iteration of upscaling. Porosity appears in decimal representation and permeability is expressed in miliDarcies (mD).

Data	Min	Max	Mean	Median	Mode	Variance	Skewness	Kurtosis
T_phi	0.103	0.2767	0.1884	0.1853	0.1030	0.0012	0.1446	2.8908
T_permX	1.1306	2588.7	174.29	48.67	1.131	1.23e+05	4.3394	25.4932
T_permY	2.7526	2999.3	201.801	59.92	2.753	1.516e+05	4.161	24.403
T_permZ	0.05	881.62	64.901	15.783	0.05	1.856e+04	3.764	19.213

Table 4.12 Tarbert formation distribution parameters after the fourth iteration of upscaling. The parentheses describe an alternative distribution fit. Porosity appears in decimal representation, permeability is measured in miliDarcies (mD) and data are analysed after applying logarithm.

Data	Distribution Type	Parameters
T_phi	Normal (Unimodal non-parametric)	$\mu=0.1884$, $\sigma^2=0.00125$ (bandwidth=0.0131)
T_permX	Normal (Unimodal non-parametric)	$\mu=4.1155$, $\sigma^2=1.9969$ (bandwidth=0.5081)
T_permY	Normal (Unimodal non-parametric)	$\mu=4.2889$, $\sigma^2=1.9602$ (bandwidth=0.4822)
T_permZ	Unimodal non-parametric	bandwidth=0.6801

5th iteration

The resulting model has dimensions 2-by-7-by-2 blocks (28 blocks). Images of the model appear in Figures 4.53a through 4.53d. The range of upscaled data as well as the respective statistical moments are presented in Table 4.13. Finally, the resulting data histograms are displayed in Figures 4.54a through 4.54d, while the respective parameters of the fit distributions are summarized in Table 4.14. All histograms have more or less the same shape and the 3D images have become indistinct.

Table 4.13 Tarbert formation statistical parameters after the fifth iteration of upscaling. Porosity appears in decimal representation and permeability is expressed in miliDarcies (mD).

Data	Min	Max	Mean	Median	Mode	Variance	Skewness	Kurtosis
T_phi	0.1234	0.2485	0.1866	0.1837	0.1234	6.678e+04	0.0122	3.758
T_permX	2.7957	640.1	102.969	47.581	2.7957	2.235e+04	2.581	8.957
T_permY	4.1812	888.16	150.331	70.983	4.1812	4.482e+04	2.373	7.9365
T_permZ	0.1262	358.22	50.338	16.868	0.1262	8.048e+03	2.6376	9.0161

Table 4.14 Tarbert formation distribution parameters after the fifth iteration of upscaling. The parentheses describe an alternative distribution fit. Porosity appears in decimal representation, permeability is measured in miliDarcies (mD) and data are analysed after applying logarithm.

Data	Distribution Type	Parameters
T_phi	Normal (Unimodal non-parametric)	$\mu=0.1866, \sigma^2=0.00067$ (bandwidth=0.00764)
T_permX	Normal (Unimodal non-parametric)	$\mu=3.9577, \sigma^2=1.3939$ (bandwidth=0.4636)
T_permY	Normal (Unimodal non-parametric)	$\mu=4.291, \sigma^2=1.5992$ (bandwidth=0.6061)
T_permZ	Normal (Unimodal non-parametric)	$\mu=2.5986, \sigma^2=3.5905$ (bandwidth=0.8691)

6th iteration

The resulting model has dimensions 1-by-4-by-1 blocks (4 blocks), thus it is represented by a linear arrangement of blocks. The resulting block values appear in Table 4.15. The difference between PermX and PermY can be due to the different flow direction along which, data are harmonically averaged.

Table 4.15 Tarbert formation block values after the sixth iteration of upscaling. Porosity appears in decimal representation and permeability is expressed in miliDarcies (mD).

Data	Block 1	Block 2	Block 3	Block 4
T_phi	0.1784	0.2063	0.1820	0.1728
T_permX	51.8361	86.4913	51.9715	17.3997
T_permY	57.9514	335.0546	58.1501	37.7507
T_permZ	9.1877	21.0869	12.0048	1.3786

7th iteration

The resulting model has dimensions 1-by-2-by-1 blocks (2 blocks), once again a linear arrangement of blocks. The resulting block values appear in Table 4.16.

Table 4.16 Tarbert formation block values after the seventh iteration of upscaling. Porosity appears in decimal representation and permeability is expressed in miliDarcies (mD).

Data	Block 1	Block 2
T_phi	0.1924	0.1774
T_permX	69.1637	34.6858
T_permY	98.8122	45.7808
T_permZ	15.1373	6.6917

8th iteration

The final iteration results in a single equivalent value for the whole model. The respective values for each property along with the corresponding Wiener bounds are presented in Table 4.17. All equivalent values fall into the suggested bounds.

Table 4.17 Tarbert formation equivalent values after the eighth iteration of upscaling, combined with Wiener bounds. Porosity appears in decimal representation and permeability is expressed in miliDarcies (mD).

Data	Wiener Bounds		Equivalent Value
	Lower	Upper	
T_phi	–	–	0.1849
T_permX	1.5884	356.4888	51.9247
T_permY	1.5884	356.488	62.5715
T_permZ	1.761e-04	94.0889	10.9145

4.2.2 Upper Ness Formation

The results of each iteration are presented in the following subsections, while the last iteration constitutes of a single equivalent value for each property. A total of eight iterations were required to reach the ultimate equivalent value. With each successive iteration data become coarser and the 3D images become more indistinct.

1st iteration

The resulting model has dimensions 30-by-110-by-25 blocks (82500 blocks). Images of the model appear in Figures 4.55a through 4.55d. The range of upscaled data as well as the respective statistical moments are presented in Table 4.18. Finally, the resulting data histograms are displayed in Figures 4.56a through 4.56d, while the respective parameters of the fit distributions are summarized in Table 4.19. The general shape of the upscaled data distributions does not differ significantly from the fine grid model and in addition, the distribution peaks seem to be more equalized between them than before upscaling. The 3D images already seem more pixelated than the fine grid model images.

Table 4.18 Upper Ness formation statistical parameters after the first iteration of upscaling. Porosity appears in decimal representation and permeability is expressed in miliDarcies (mD).

Data	Min	Max	Mean	Median	Mode	Variance	Skewness	Kurtosis
UN_phi	0.0	0.389	0.1564	0.1547	0.0	0.0062	0.1015	2.0502
UN_permX	0.0036	19601	246.32	47.46	0.0036	4.58e+05	8.8699	128.401
UN_permY	0.0038	19600	294.75	58.83	0.0038	5.997e+05	7.663	94.663
UN_permZ	4.485e-07	5134.7	32.876	0.0291	3.159e-06	1.899e+04	12.119	226.38

Table 4.19 Upper Ness formation distribution parameters after the first iteration of upscaling. Porosity appears in decimal representation, permeability is measured in miliDarcies (mD) and data are analysed after applying logarithm.

Data	Distribution Type	Parameters
UN_phi	Bimodal non-parametric	bandwidth=0.0107
UN_permX	Bimodal non-parametric	bandwidth=0.4326
UN_permY	Bimodal non-parametric	bandwidth=0.4233
UN_permZ	Trimodal non-parametric	bandwidth=1.091

2nd iteration

The resulting model has dimensions 15-by-55-by-13 blocks (10725 blocks). Images of the model appear in Figures 4.57a through 4.57d. The range of upscaled data as well as

the respective statistical moments are presented in Table 4.20. Finally, the resulting data distributions are displayed in Figures 4.58a through 4.58d, while the respective parameters of the fit distributions are summarized in Table 4.21. The general shape of the upscaled data distributions is similar to that of the fine grid model, while all distributions appear to shift weight from low to higher permeability. The medium permeability peak of PermZ tends to flatten out. The 3D images already become more pixelated than those of the fine grid model.

Table 4.20 Upper Ness formation statistical parameters after the second iteration of upscaling. Porosity appears in decimal representation and permeability is expressed in miliDarcies (mD).

Data	Min	Max	Mean	Median	Mode	Variance	Skewness	Kurtosis
UN_phi	0.0065	0.3253	0.1544	0.1554	0.1657	0.004	-0.0397	2.0664
UN_permX	0.0095	13988	159.23	64.045	0.0095	1.156e+05	12.481	340.962
UN_permY	0.0125	14451	232.87	101.18	0.0125	2.055e+05	8.611	161.32
UN_permZ	1.411e-06	3404.7	31.65	7.8232	1.411e-06	7.008e+03	12.147	316.701

Table 4.21 Upper Ness formation distribution parameters after the second iteration of upscaling. Porosity appears in decimal representation, permeability is measured in miliDarcies (mD) and data are analysed after applying logarithm.

Data	Distribution Type	Parameters
UN_phi	Bimodal non-parametric	bandwidth=0.0125
UN_permX	Bimodal non-parametric	bandwidth=0.386
UN_permY	Bimodal non-parametric	bandwidth=0.346
UN_permZ	Trimodal non-parametric	bandwidth=0.4472

3rd iteration

The resulting model has dimensions 8-by-28-by-7 blocks (1568 blocks). Images of the model appear in Figures 4.59a through 4.59d. The range of upscaled data as well as the respective statistical moments are presented in Table 4.22. Finally, the resulting data distributions are displayed in Figures 4.60a through 4.60d, while the respective parameters of the fit distributions are summarized in Table 4.23. The general shape of the upscaled data distributions is still close to that of the fine grid model, while all distributions keep shifting weight from low to higher permeability. Porosity tends to a single peak distribution, however the multimodal distribution still fits better the distribution of the data. In addition, the medium permeability peak of PermZ has flattened out almost completely. The 3D images have become even more pixelated and the channels are barely recognizable.

Table 4.22 Upper Ness formation statistical parameters after the third iteration of upscaling. Porosity appears in decimal representation and permeability is expressed in miliDarcies (mD).

Data	Min	Max	Mean	Median	Mode	Variance	Skewness	Kurtosis
UN_phi	0.0215	0.2585	0.1497	0.1515	0.0215	0.0022	-0.1475	2.2678
UN_permX	0.0273	1131.1	98.121	65.714	0.0273	1.416e+04	2.764	16.84
UN_permY	0.0376	3691	182.2	124.39	0.0376	5.115e+04	4.346	46.51
UN_permZ	4.92e-06	1201.6	29.008	16.949	4.92e-06	2.481e+03	10.324	207.25

Table 4.23 Upper Ness formation distribution parameters after the third iteration of upscaling. The parentheses describe an alternative distribution fit. Porosity appears in decimal representation, permeability is measured in miliDarcies (mD) and data are analysed after applying logarithm.

Data	Distribution Type	Parameters
UN_phi	Unimodal non-parametric (Normal)	bandwidth=0.0126 ($\mu=0.1497$, $\sigma^2=0.0022$)
UN_permX	Bimodal non-parametric	bandwidth=0.3641
UN_permY	Bimodal non-parametric	bandwidth=0.3207
UN_permZ	Trimodal non-parametric	bandwidth=0.3484

4th iteration

The resulting model has dimensions 4-by-14-by-4 blocks (224 blocks). Images of the model appear in Figures 4.61a through 4.61d. The range of upscaled data as well as the respective statistical moments are presented in Table 4.24. Finally, the resulting data distributions are displayed in Figures 4.62a through 4.62d, while the respective parameters of the fit distributions are summarized in Table 4.25. The shape of the upscaled data distributions is not similar any more to that of the fine grid model. The low permeability peaks have all severely reduced, while PermZ includes a lot of sparse data between the low and high permeability peaks. Last but not least, the 3D images have become quite vague.

Table 4.24 Upper Ness formation statistical parameters after the fourth iteration of upscaling. Porosity appears in decimal representation and permeability is expressed in miliDarcies (mD).

Data	Min	Max	Mean	Median	Mode	Variance	Skewness	Kurtosis
UN_phi	0.0561	0.221	0.1441	0.1463	0.0561	0.0013	-0.1386	2.442
UN_permX	0.0753	366.86	62.569	52.145	0.0753	4.087e+03	1.577	6.308
UN_permY	0.0972	744.52	144.91	129.01	0.0972	1.565e+04	1.332	5.912
UN_permZ	1.412e-05	306.48	25.498	21.404	1.412e-05	895.08	4.463	37.817

Table 4.25 Upper Ness formation distribution parameters after the fourth iteration of upscaling. The parentheses describe an alternative distribution fit. Porosity appears in decimal representation, permeability is measured in miliDarcies (mD) and data are analysed after applying logarithm.

Data	Distribution Type	Parameters
UN_phi	Unimodal non-parametric (Normal)	bandwidth=0.013 ($\mu=0.144$, $\sigma^2=0.0013$)
UN_permX	Bimodal non-parametric	bandwidth=0.3916
UN_permY	Bimodal non-parametric	bandwidth=0.3504
UN_permZ	Bimodal non-parametric	bandwidth=0.3484

5th iteration

The resulting model has dimensions 2-by-7-by-2 blocks (28 blocks). Images of the model appear in Figures 4.63a through 4.63d. The range of upscaled data as well as the respective statistical moments are presented in Table 4.26. Finally, the resulting data distributions are displayed in Figures 4.64a through 4.64d, while the respective parameters of the fit distributions are summarized in Table 4.27. At this point, the data display little information in comparison to the fine grid model, porosity approaches a uniform distribution and the distinct low permeability peak does not appear in PermY data. In PermZ distribution the medium permeability peak has reappeared, however that could very well be considered an over-statement. The 3D images display no clear information about the formation.

Table 4.26 Upper Ness formation statistical parameters after the fifth iteration of upscaling. Porosity appears in decimal representation and permeability is expressed in miliDarcies (mD).

Data	Min	Max	Mean	Median	Mode	Variance	Skewness	Kurtosis
UN_phi	0.1052	0.1776	0.1441	0.1437	0.1052	5.038e-04	-0.0642	1.702
UN_permX	4.308	115.74	46.231	42.45	4.308	908.44	0.4266	2.364
UN_permY	26.904	286.44	133.44	126.6	26.904	5164.2	0.4913	2.153
UN_permZ	4.277e-05	82.041	19.771	14.209	4.277e-05	455.1	0.9404	3.495

6th iteration

The resulting model has dimensions 1-by-4-by-1 blocks (4 blocks), thus it is represented by a linear arrangement of blocks. The resulting block values appear in Table 4.28. The difference between PermX and PermY can be caused by the harmonic averaging, which is applied along different flow directions.

Table 4.27 Upper Ness formation distribution parameters after the fifth iteration of upscaling. Porosity appears in decimal representation, permeability is measured in miliDarcies (mD) and data are analysed after applying logarithm.

Data	Distribution Type	Parameters
UN_phi	Unimodal non-parametric	bandwidth=0.017
UN_permX	Bimodal non-parametric	bandwidth=0.3964
UN_permY	Unimodal non-parametric	bandwidth=0.4167
UN_permZ	Trimodal non-parametric	bandwidth=1.0623

Table 4.28 Upper Ness formation block values after the sixth iteration of upscaling. Porosity appears in decimal representation and permeability is expressed in miliDarcies (mD).

Data	Block 1	Block 2	Block 3	Block 4
UN_phi	0.1451	0.1442	0.1427	0.1444
UN_permX	38.7261	44.7238	41.5534	35.9065
UN_permY	147.2840	137.0625	111.9781	137.8747
UN_permZ	1.5684	5.2680	2.2246	3.8282

7th iteration

The resulting model has dimensions 1-by-2-by-1 blocks (2 blocks), resulting again in a linear arrangement of blocks. The block values appear in Table 4.29. The difference between PermX and PermY remains the approximately same.

Table 4.29 Upper Ness formation block values after the seventh iteration of upscaling. Porosity appears in decimal representation and permeability is expressed in miliDarcies (mD).

Data	Block 1	Block 2
UN_phi	0.1447	0.1435
UN_permX	41.7249	38.7300
UN_permY	141.9895	123.5844
UN_permZ	3.4182	3.0264

8th iteration

The final iteration results in a single equivalent value for the whole model. The respective values for each property along with the corresponding Wiener bounds are presented in Table 4.30. The difference between PermX and PermY has increased insignificantly. All equivalent values fall into the suggested bounds.

Table 4.30 Upper Ness formation equivalent values after the eighth iteration of upscaling, combined with Wiener bounds. Porosity appears in decimal representation and permeability is expressed in miliDarcies (mD).

Data	Wiener Bounds		Equivalent Value
	Lower	Upper	
UN_phi	–	–	0.1441
UN_permX	0.124	354.96	40.228
UN_permY	0.124	354.96	132.15
UN_permZ	1.241e-05	33.474	3.222

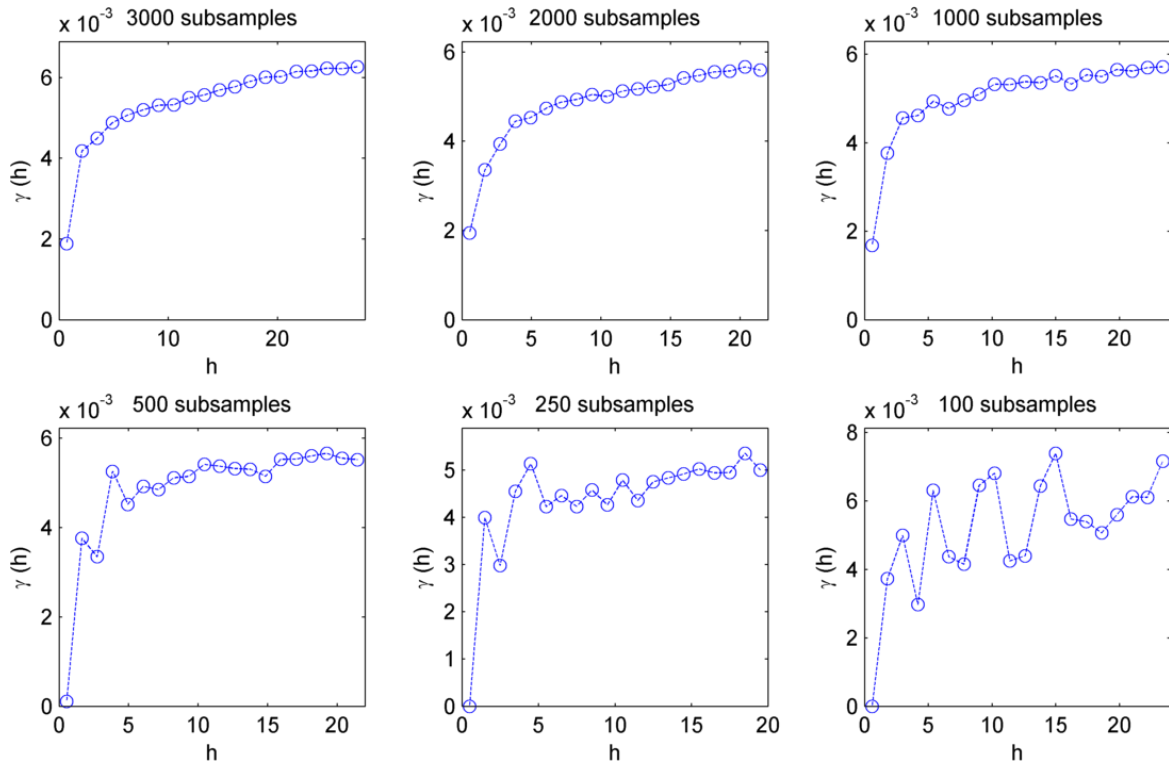


Fig. 4.2 Indicative 3D variogram plots with different number of used sampling points, for a subvolume (X:15–45, Y:50–150, Z:15:25) of porosity of Tarbert formation.

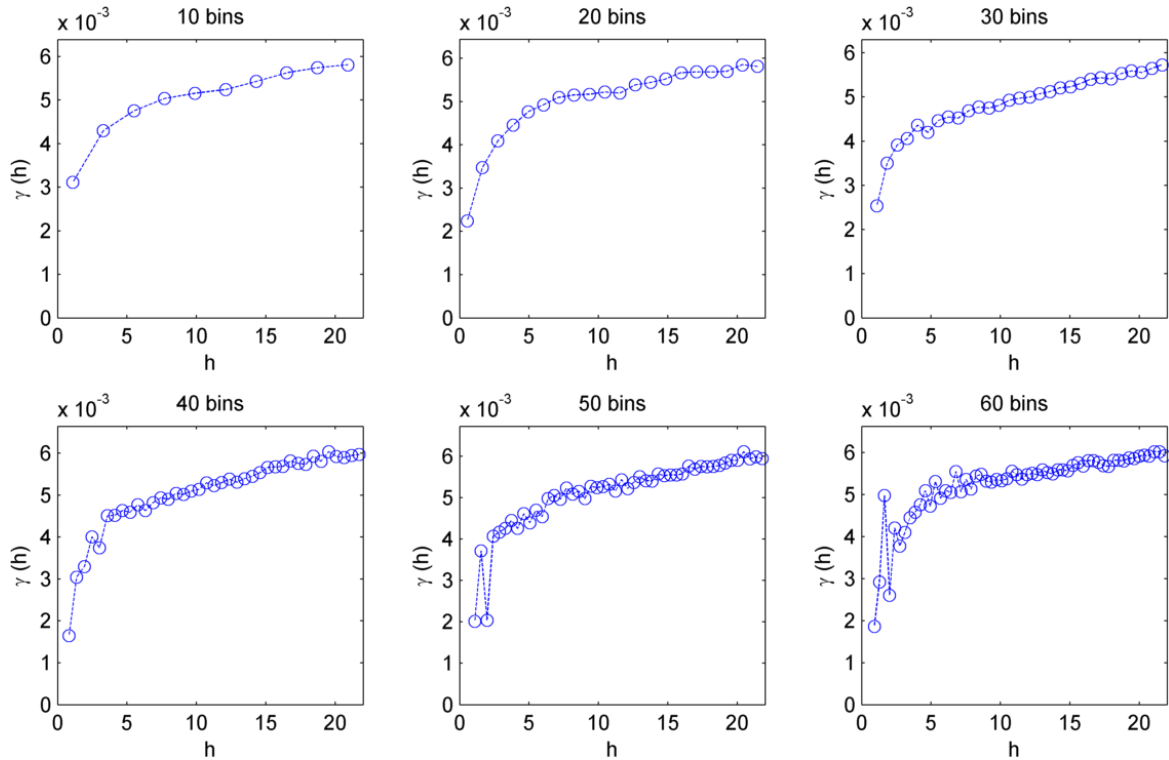


Fig. 4.3 Indicative variogram plots with different number of lag distance bins, for a subvolume (X:15–45, Y:50–150, Z:15:25) of porosity of Tarbert formation. Respective minimum lag distance is equal to $h = \text{maxdist}/\text{bins}$.

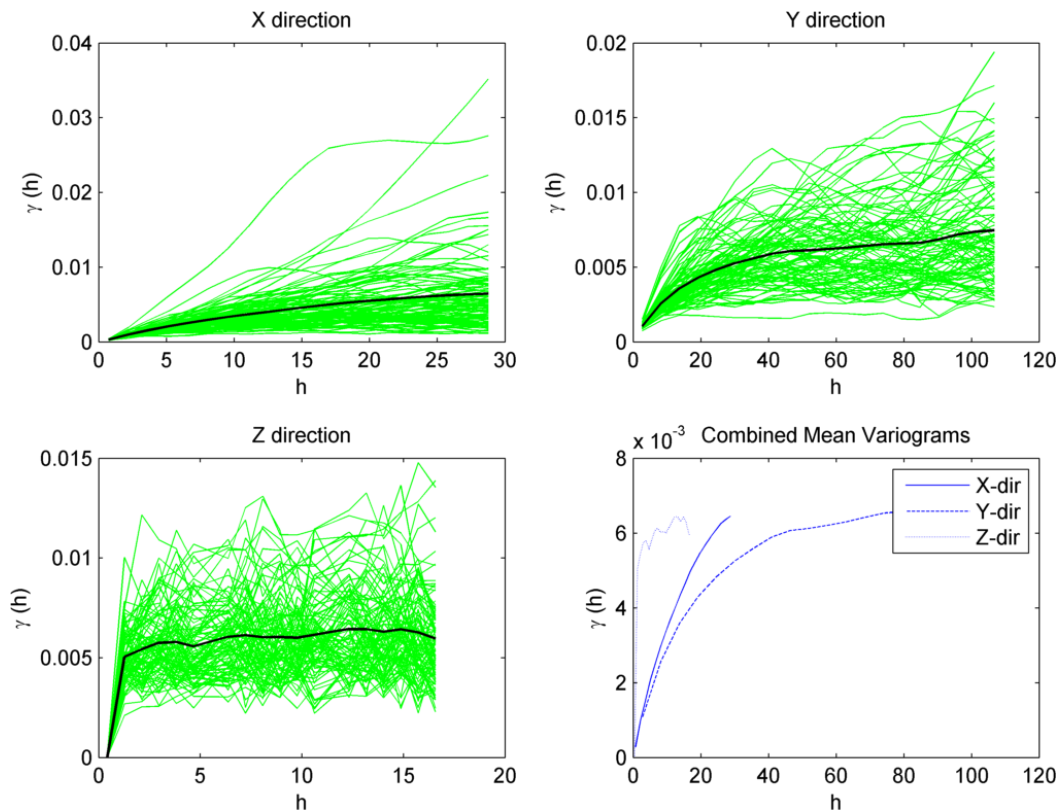


Fig. 4.4 Combined marginal variograms of 100 core samples for porosity of Tarbert formation, for the three principal directions. The black line represents the mean variogram.

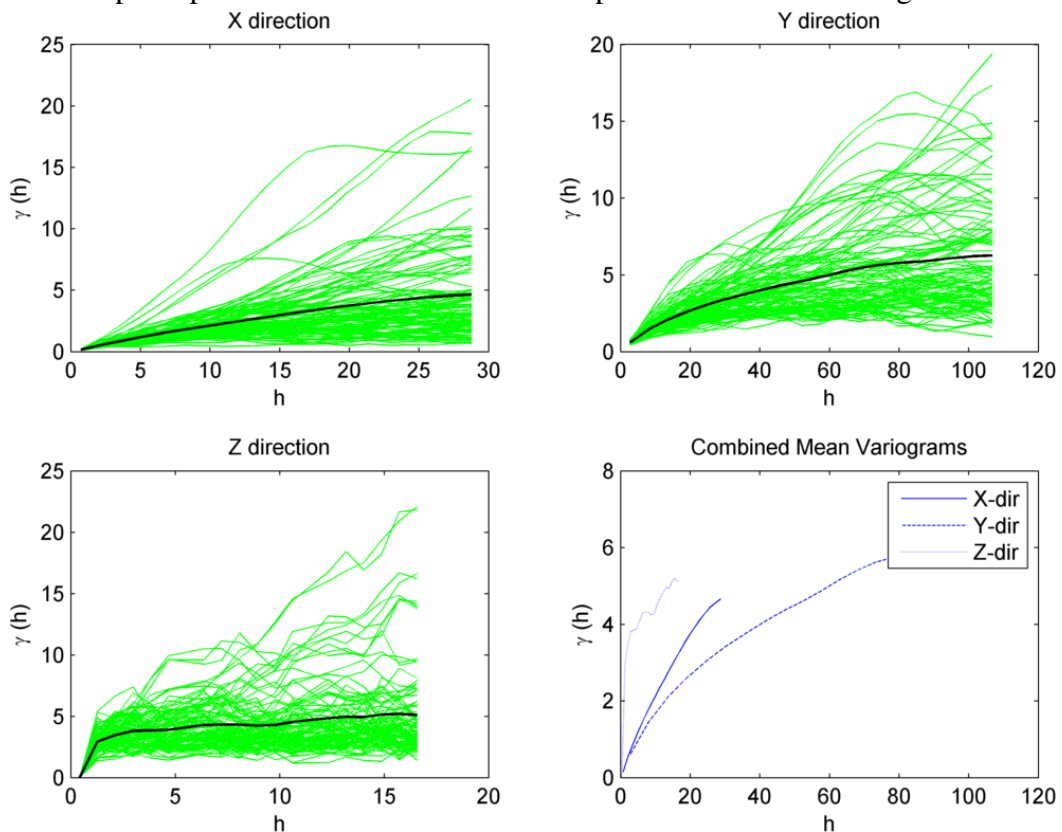


Fig. 4.5 Combined marginal variograms of 100 core samples for permeability of X-direction of Tarbert formation, for the three principal directions. The black line represents the mean variogram.

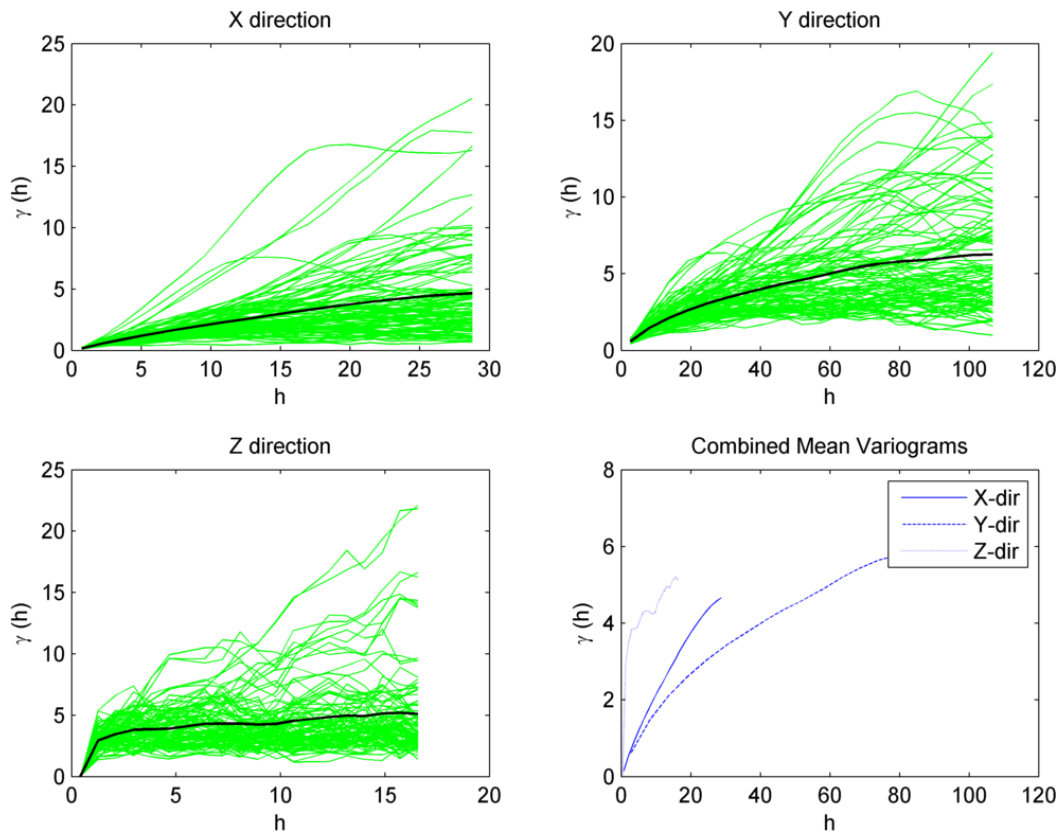


Fig. 4.6 Combined marginal variograms of 100 core samples for permeability of Y-direction of Tarbert formation, for the three principal directions. The black line represents the mean variogram.

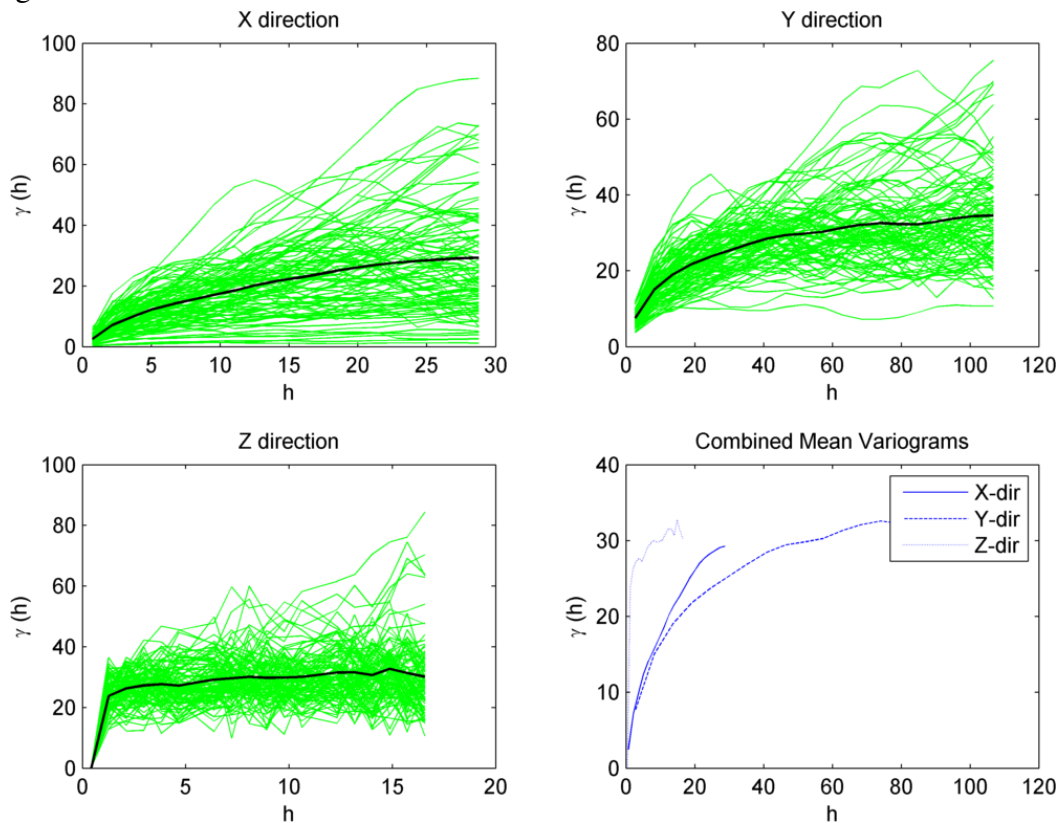
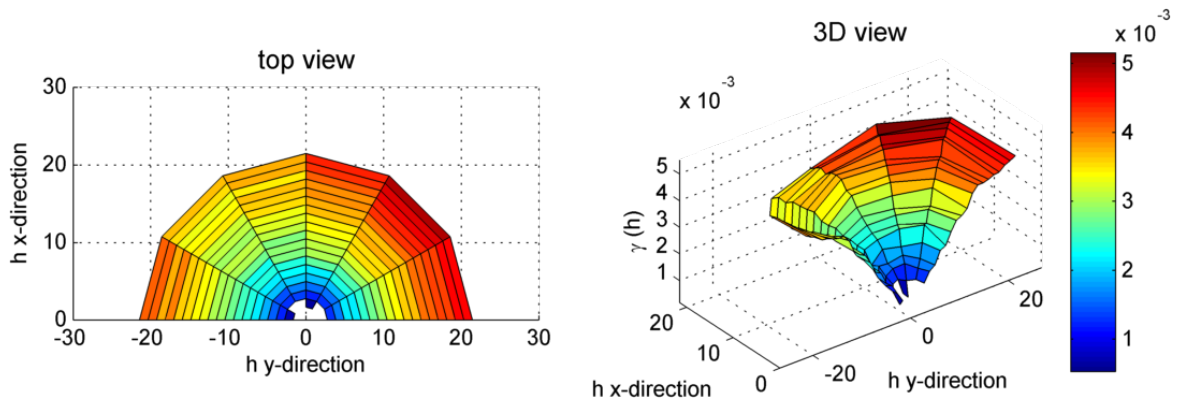
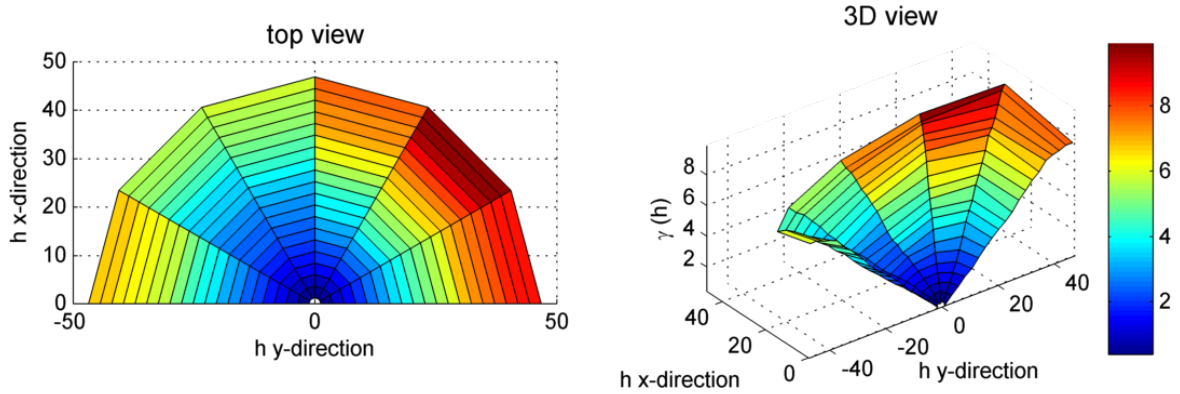


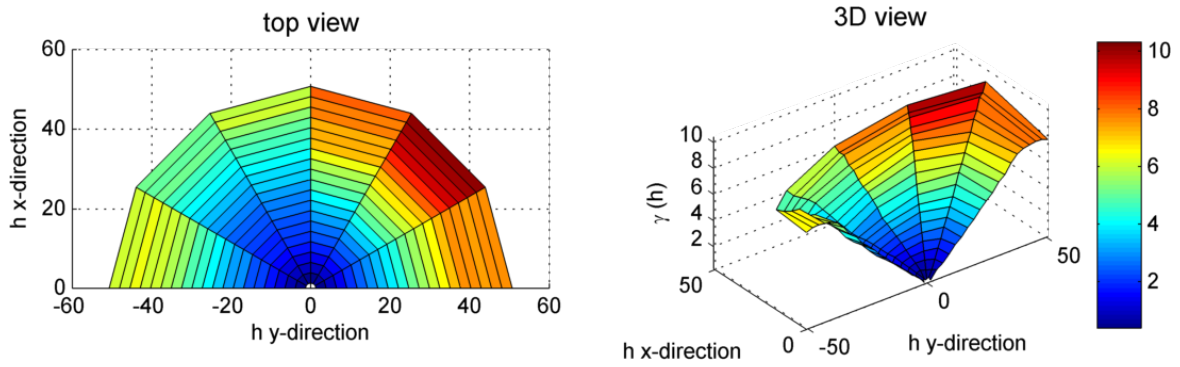
Fig. 4.7 Combined marginal variograms of 100 core samples for permeability of Z-direction of Tarbert formation, for the three principal directions. The black line represents the mean variogram.



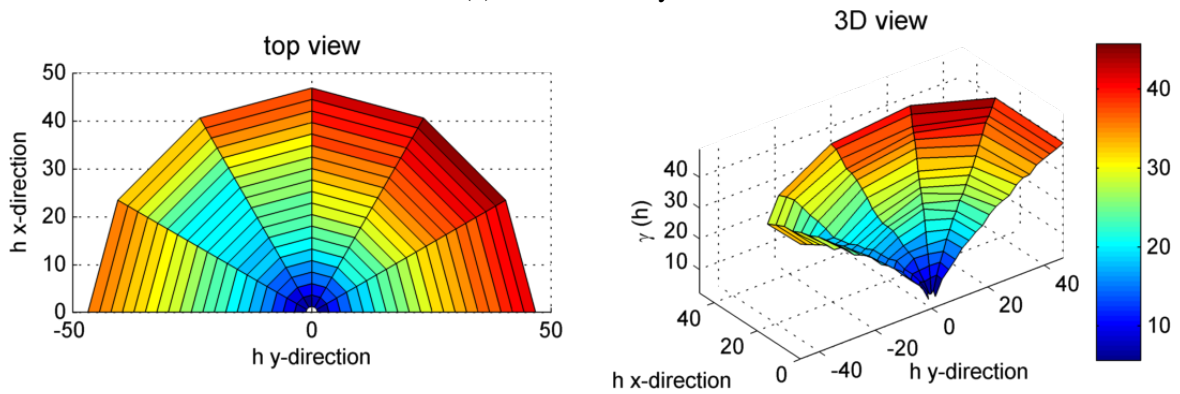
(a) T_Phi-Layer 1



(b) T_PermX-Layer 1

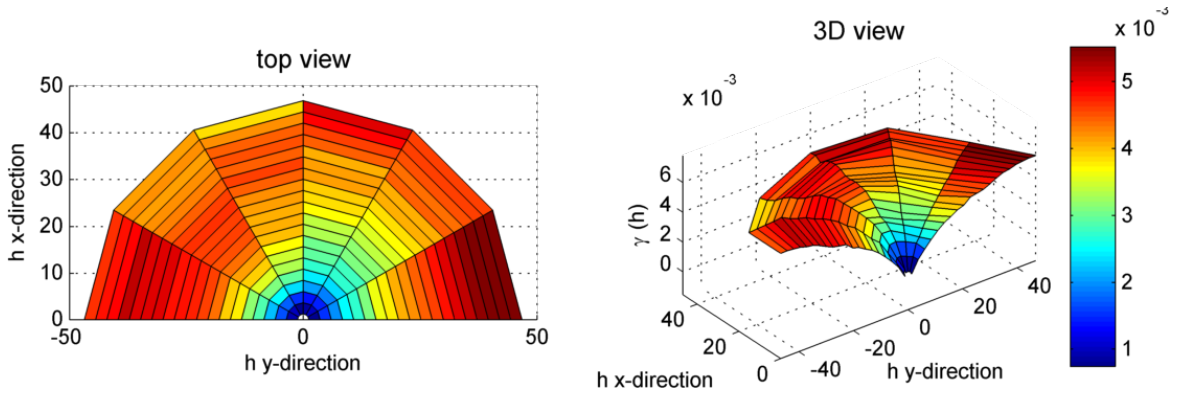


(c) T_PermY-Layer 1

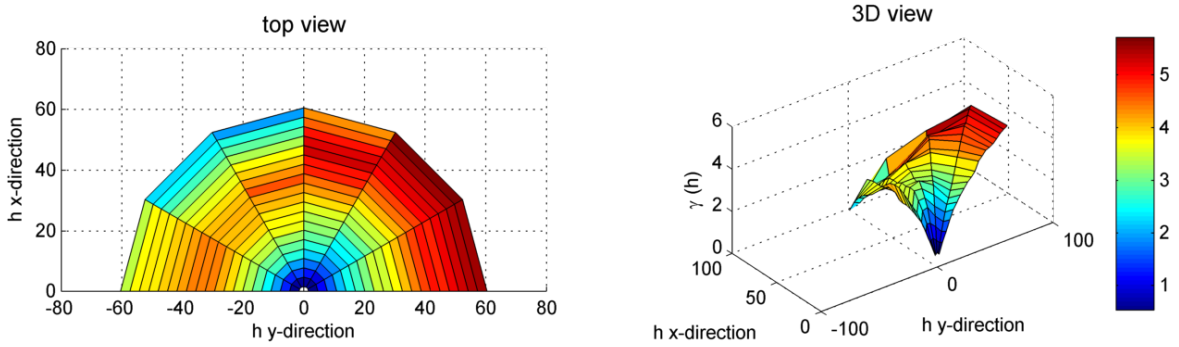


(d) T_PermZ-Layer 1

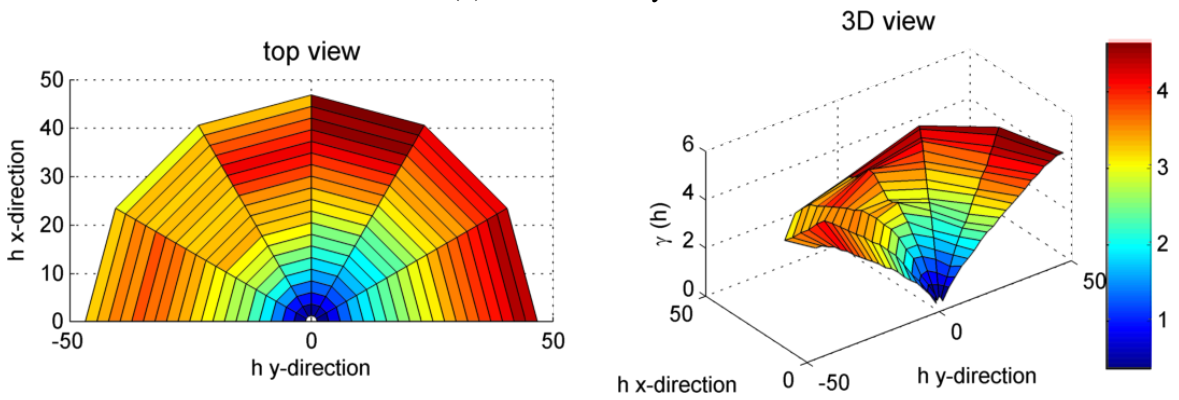
Fig. 4.8 Top and 3D view of anisotropic variogram of the first (bottom) layer for porosity and permeability of the Tarbert formation.



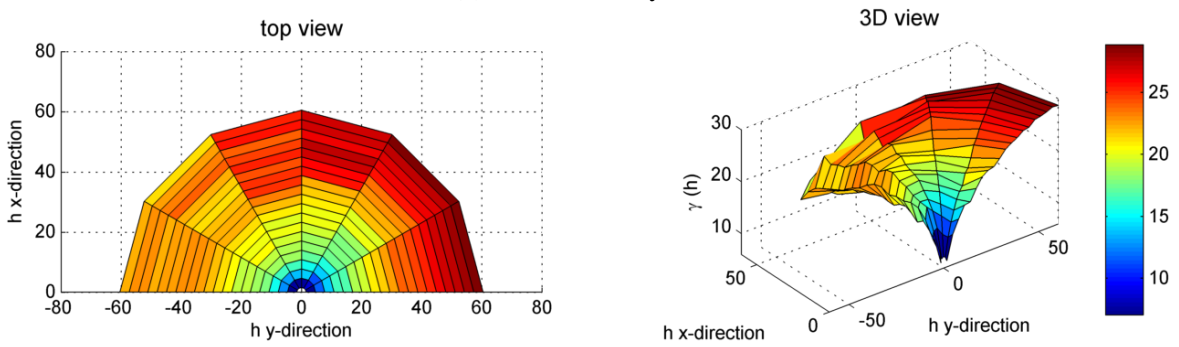
(a) T_Phi-Layer 10



(b) T_PermX-Layer 10



(c) T_PermY-Layer 10



(d) T_PermZ-Layer 10

Fig. 4.9 Top and 3D view of anisotropic variogram of the 10th layer for porosity and permeability of the Tarbert formation.

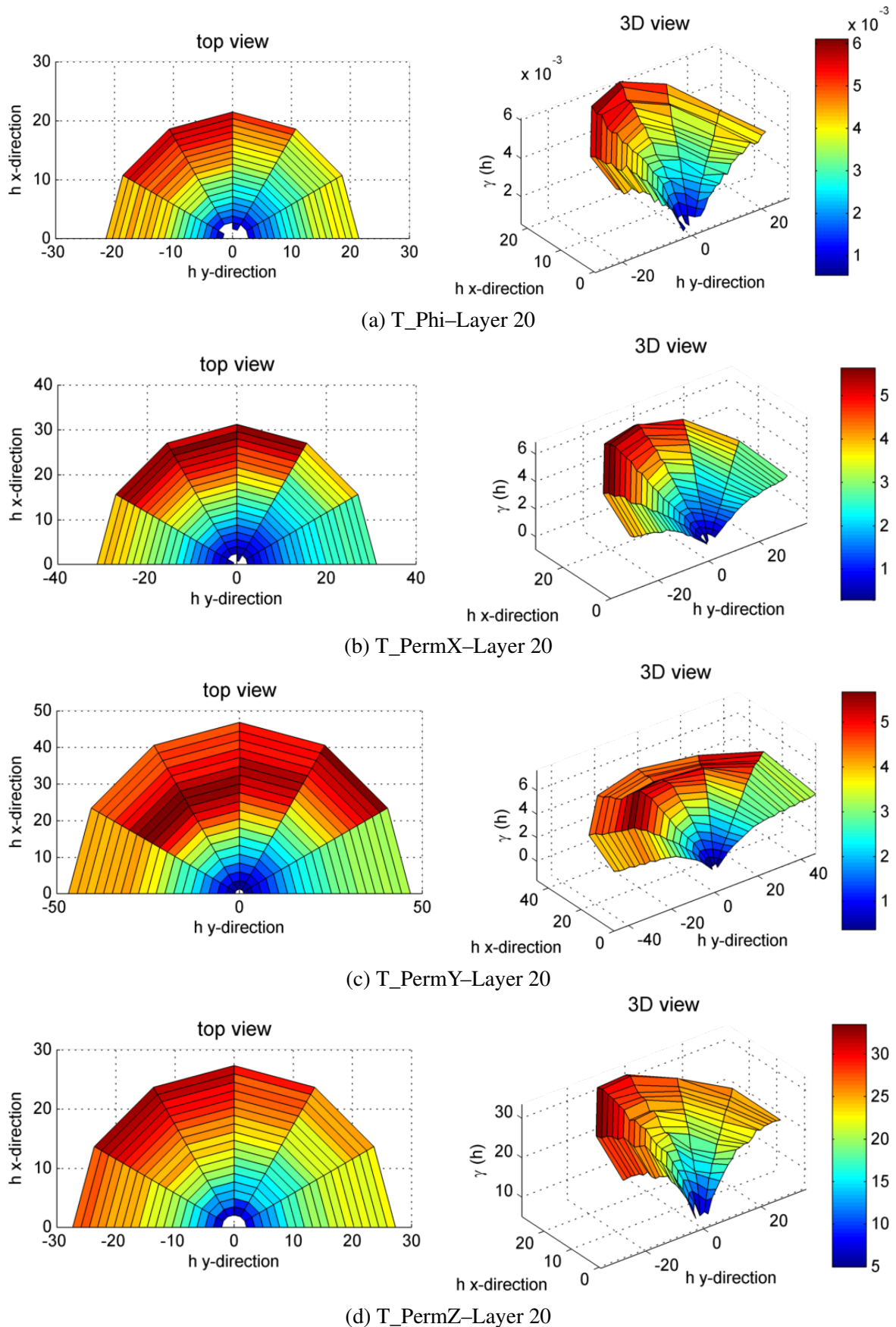
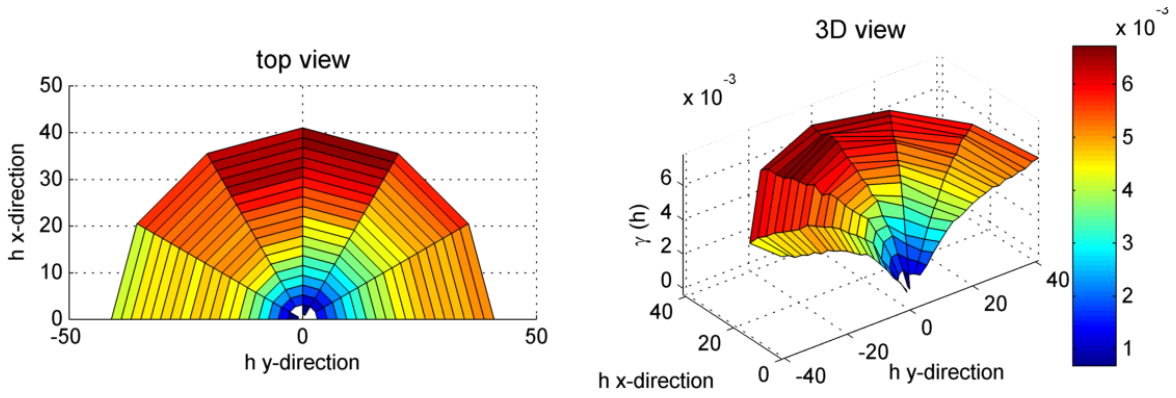
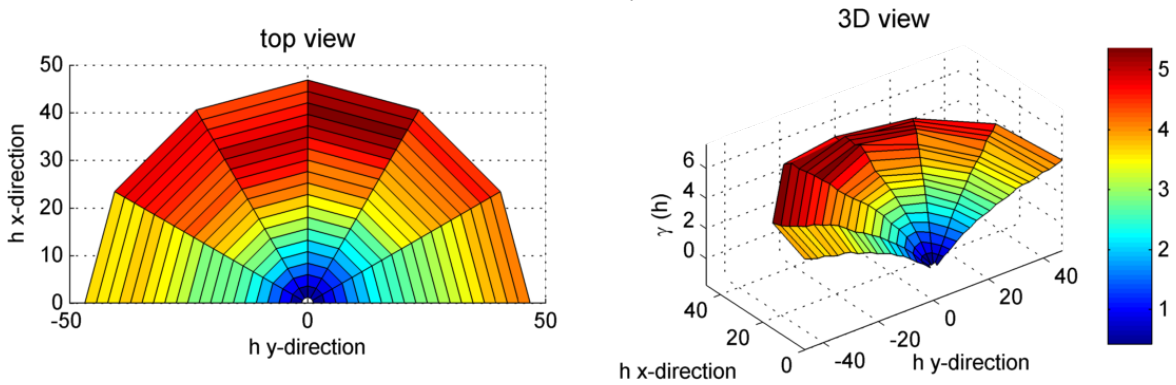


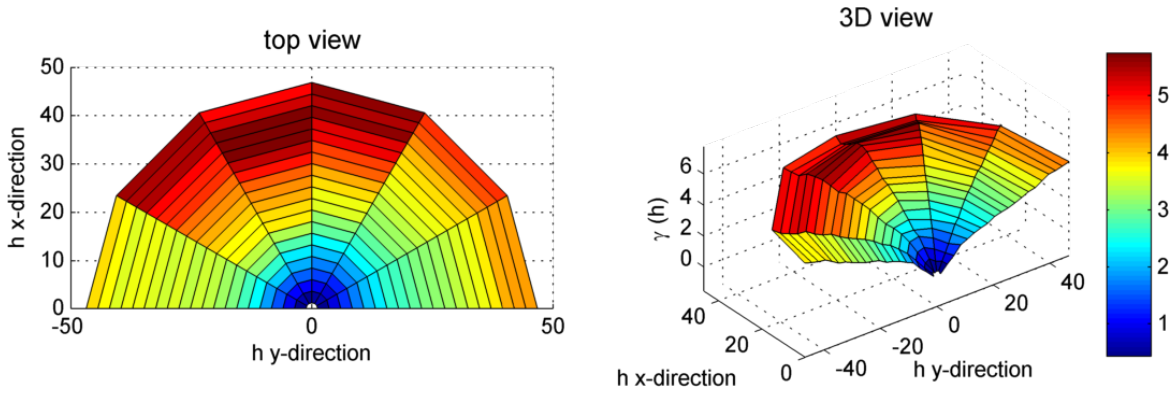
Fig. 4.10 Top and 3D view of anisotropic variogram of the 20th layer for porosity and permeability of the Tarbert formation.



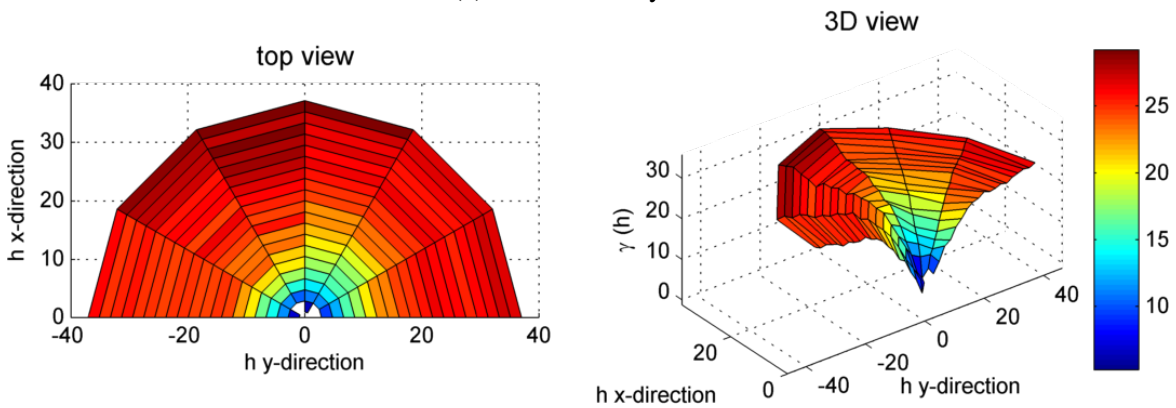
(a) T_Phi-Layer 30



(b) T_PermX-Layer 30

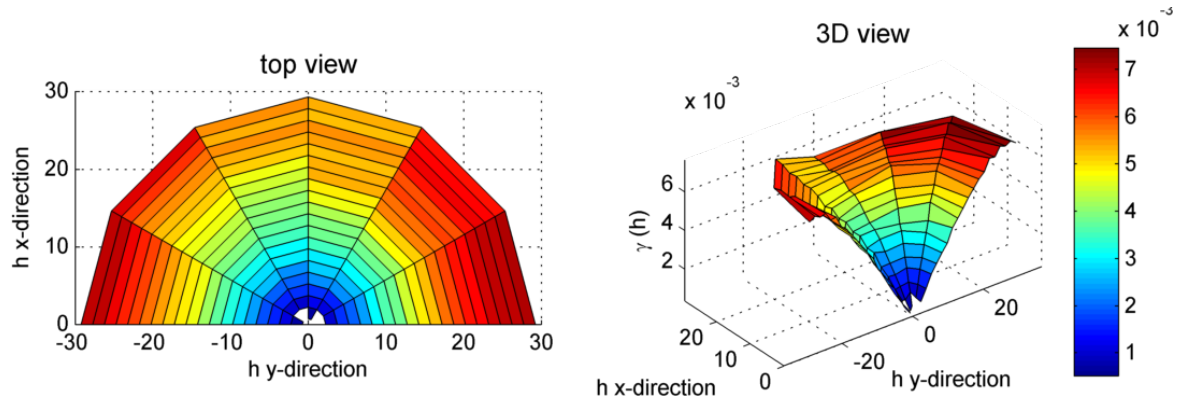


(c) T_PermY-Layer 30

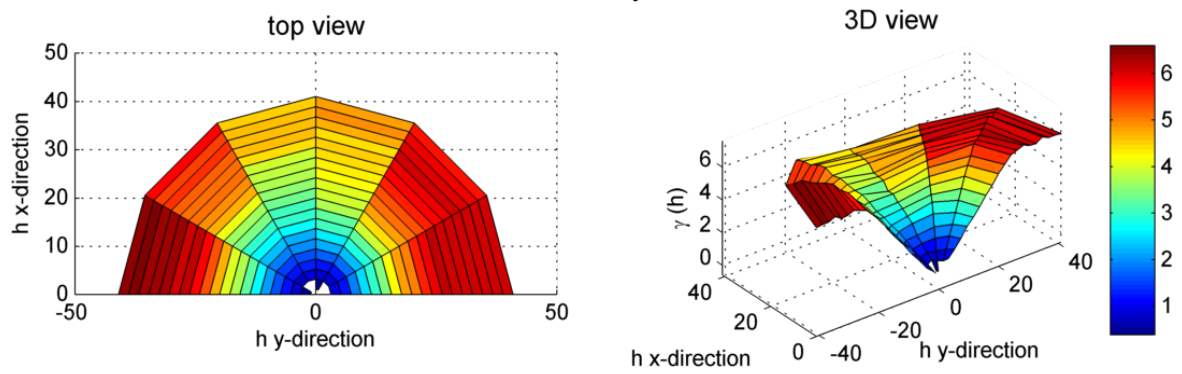


(d) T_PermZ-Layer 30

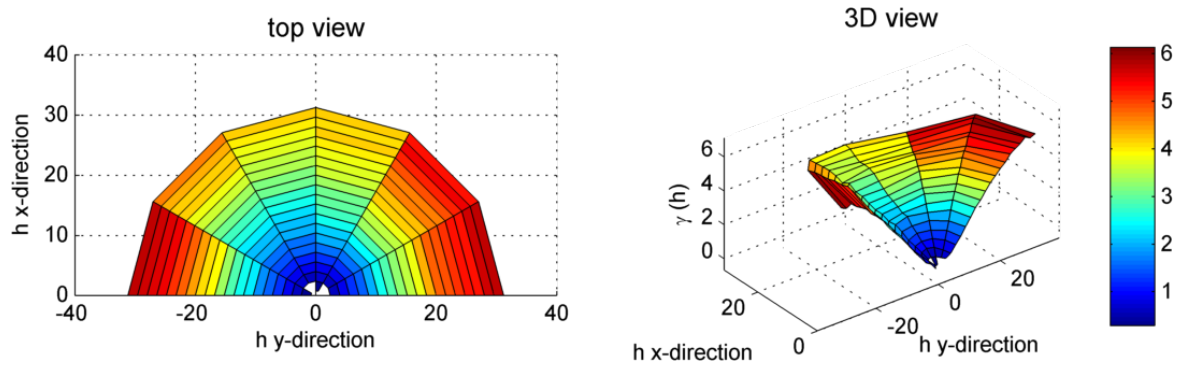
Fig. 4.11 Top and 3D view of anisotropic variogram of the 30th layer for porosity and permeability of the Tarbert formation.



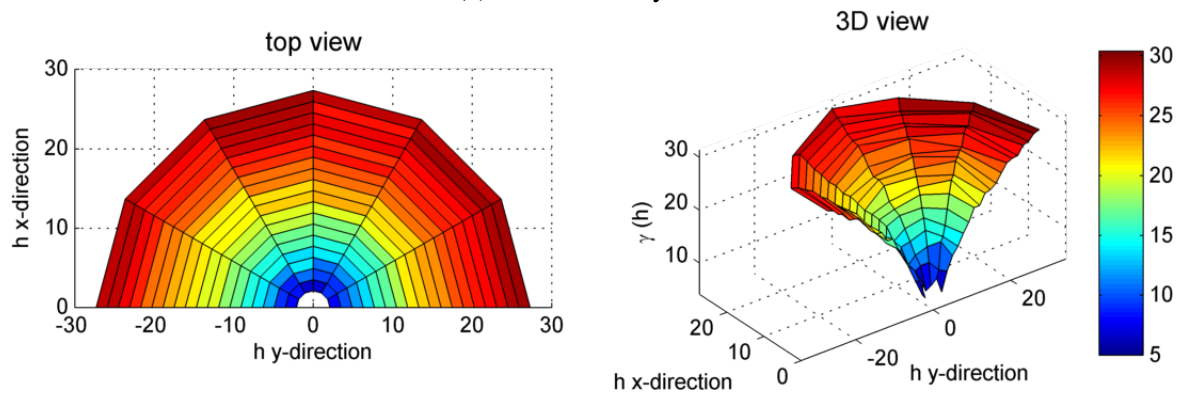
(a) T_Phi-Layer 35



(b) T_PermX-Layer 35



(c) T_PermY-Layer 35



(d) T_PermZ-Layer 35

Fig. 4.12 Top and 3D view of anisotropic variogram of the 35th (top) layer for porosity and permeability of the Tarbert formation.

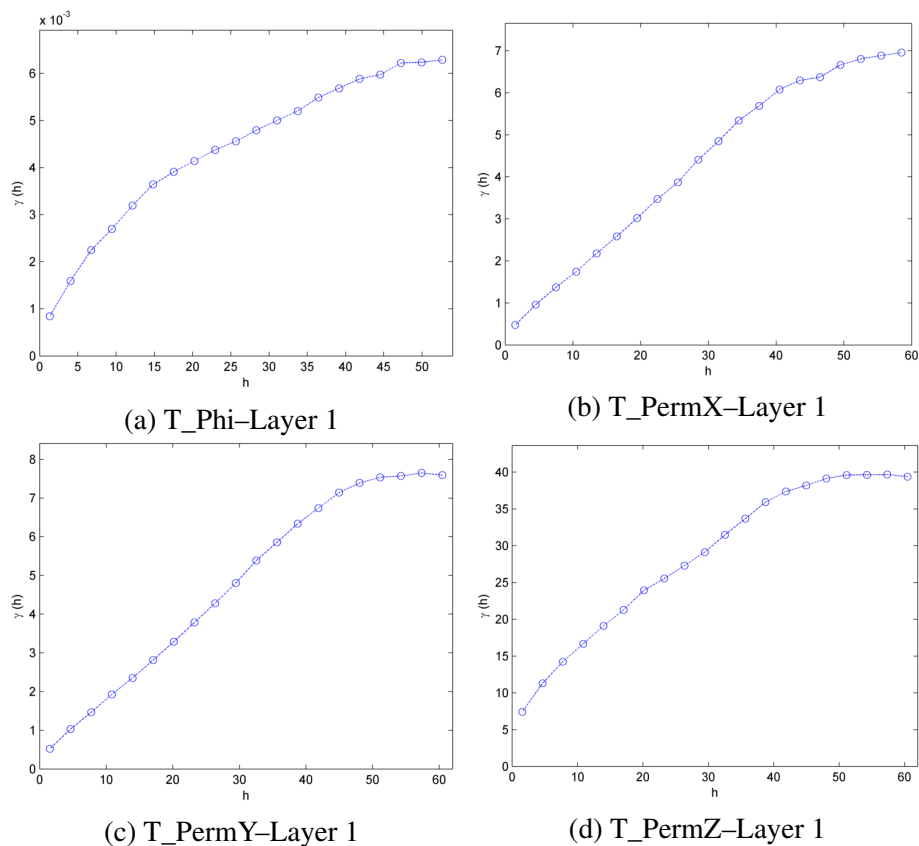


Fig. 4.13 Omnidirectional variograms of the first (bottom) layer for porosity and permeability of the Tarbert formation.

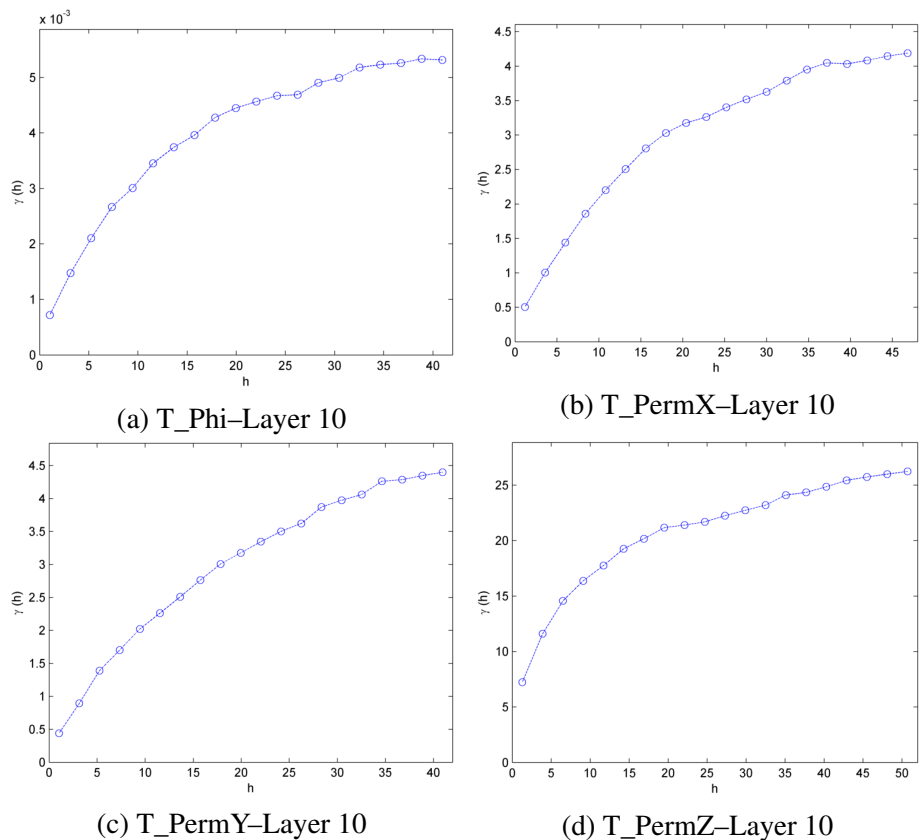


Fig. 4.14 Omnidirectional variograms of the 10th layer for porosity and permeability of the Tarbert formation.

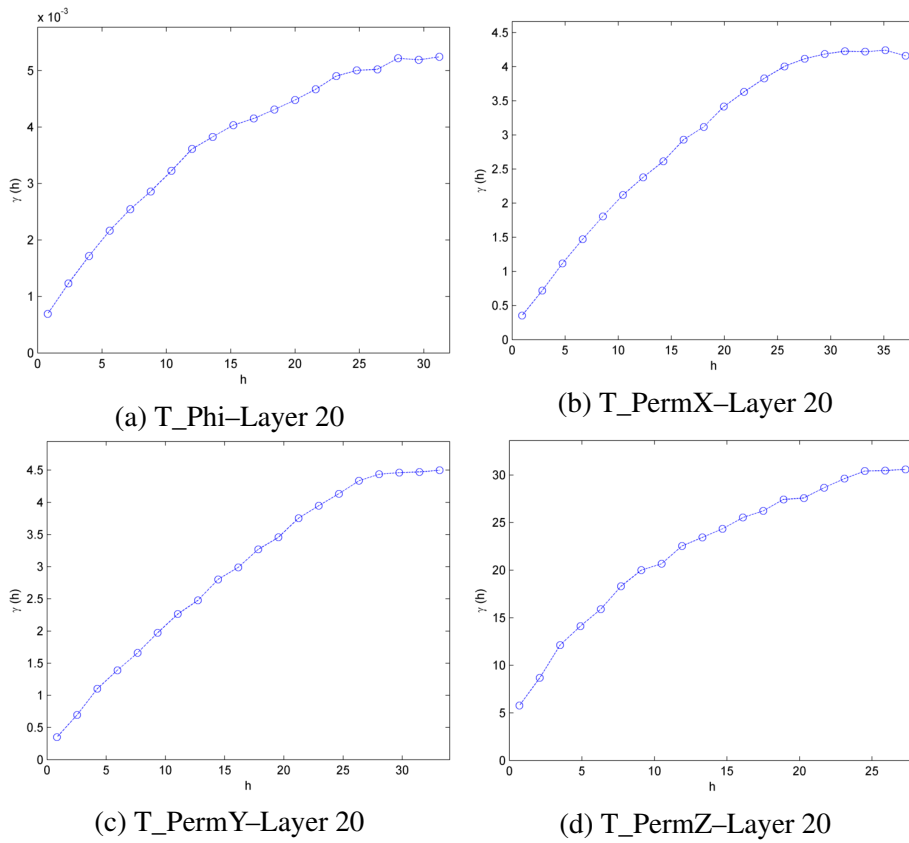


Fig. 4.15 Omnidirectional variograms of the 20th layer for porosity and permeability of the Tarbert formation.

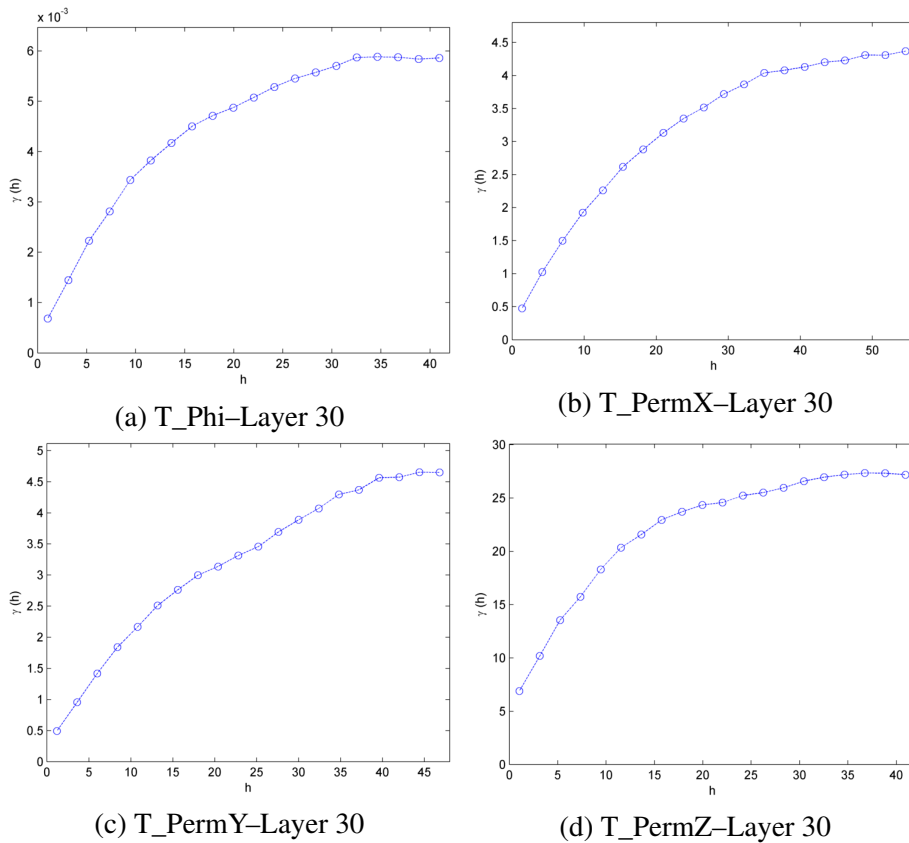


Fig. 4.16 Omnidirectional variograms of the 30th layer for porosity and permeability of the Tarbert formation.

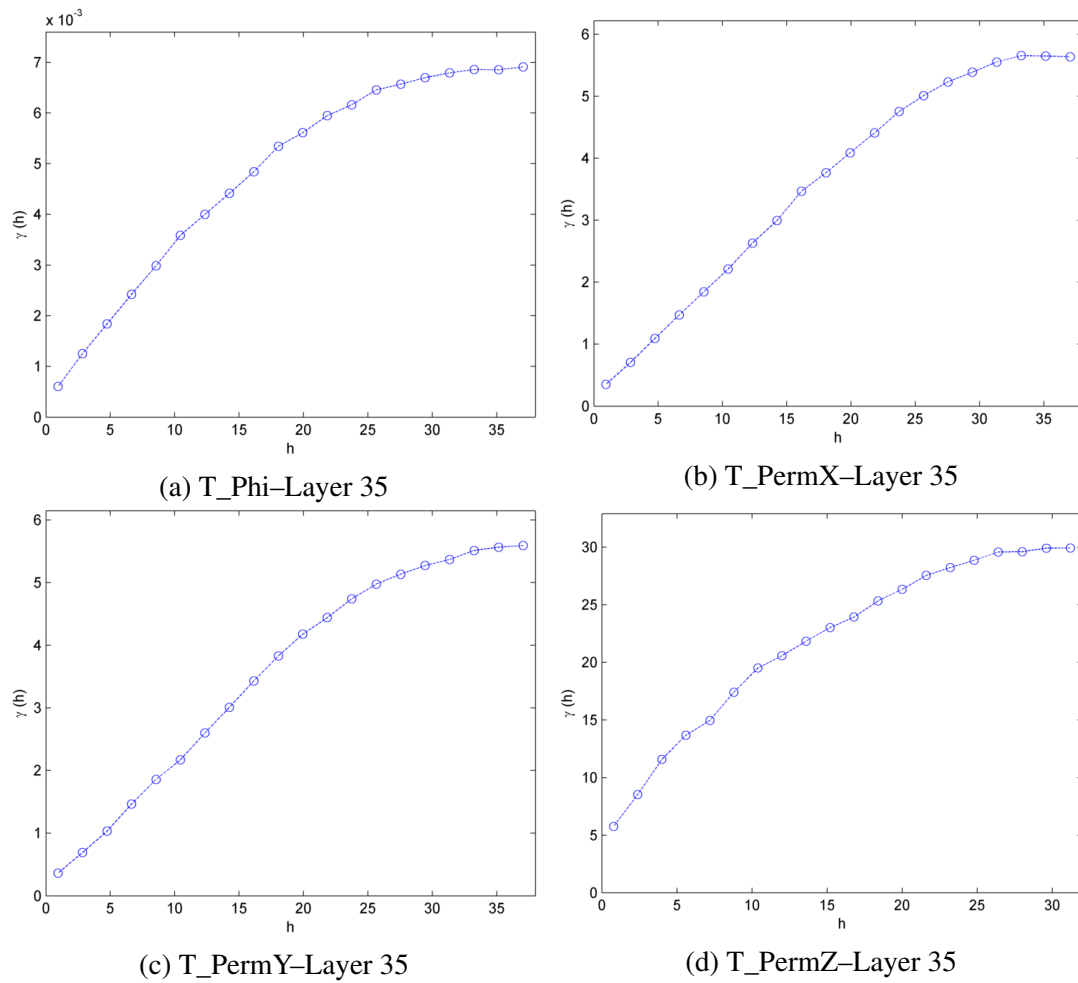


Fig. 4.17 Omnidirectional variograms of the 35th (top) layer for porosity and permeability of the Tarbert formation.

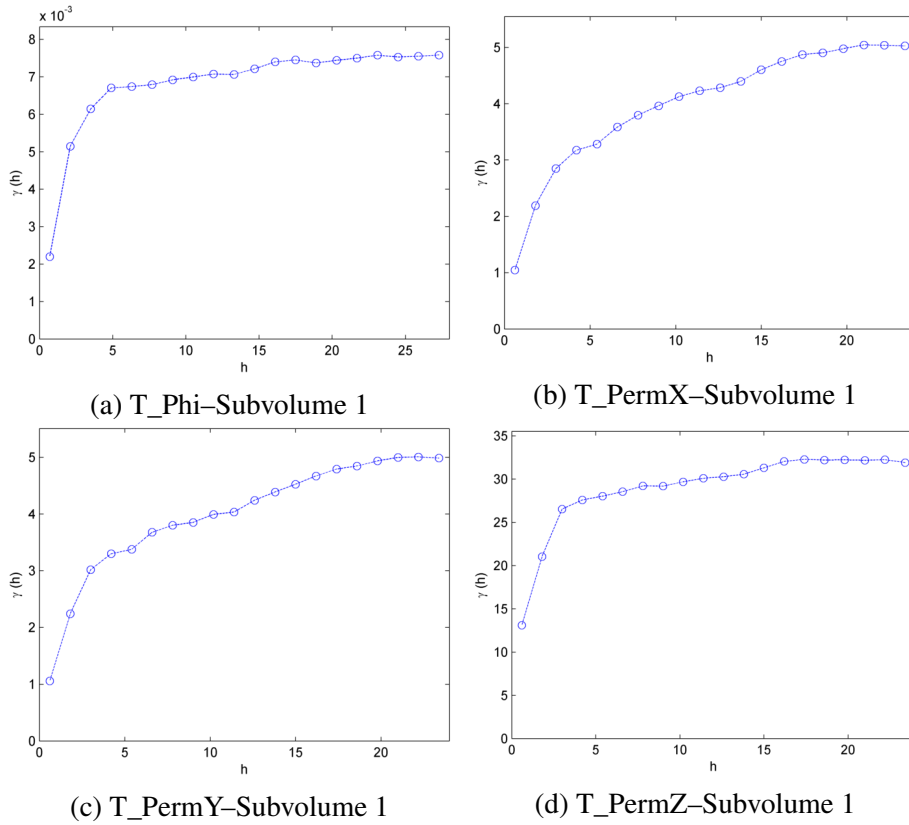


Fig. 4.18 3D variograms of the first (basic) subvolume (X:6–25, Y:21–90, Z:11–30) for porosity and permeability of the Tarbert formation.

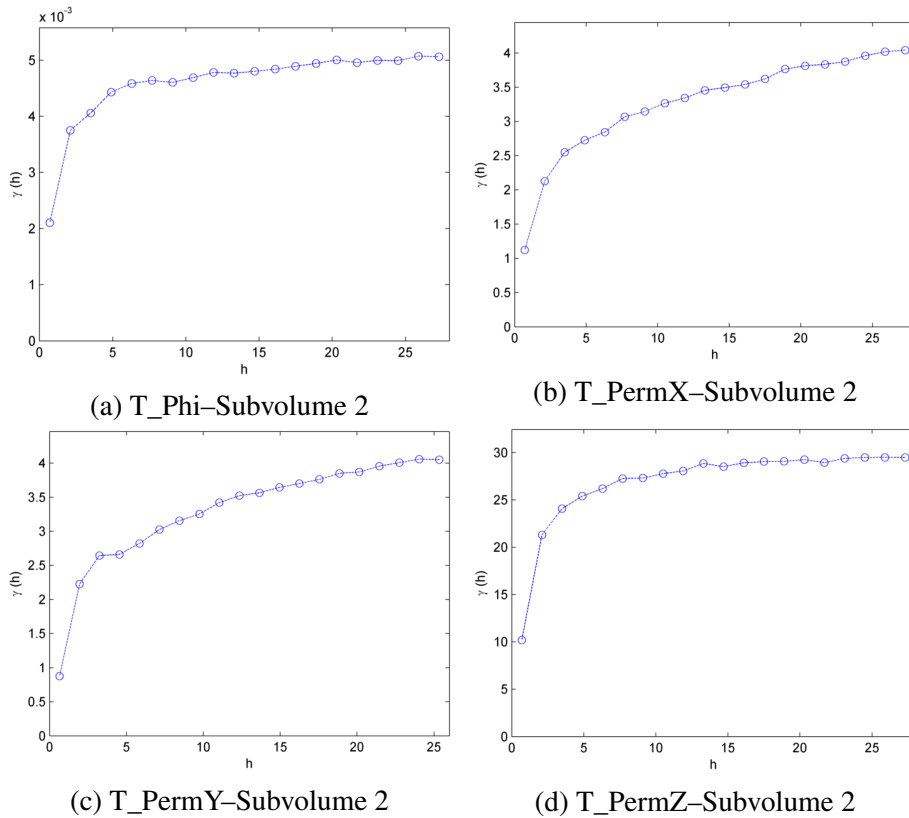


Fig. 4.19 3D variograms of the second (elongated towards X-direction) subvolume (X:36–55, Y:1–110, Z:11–30) for porosity and permeability of the Tarbert formation.

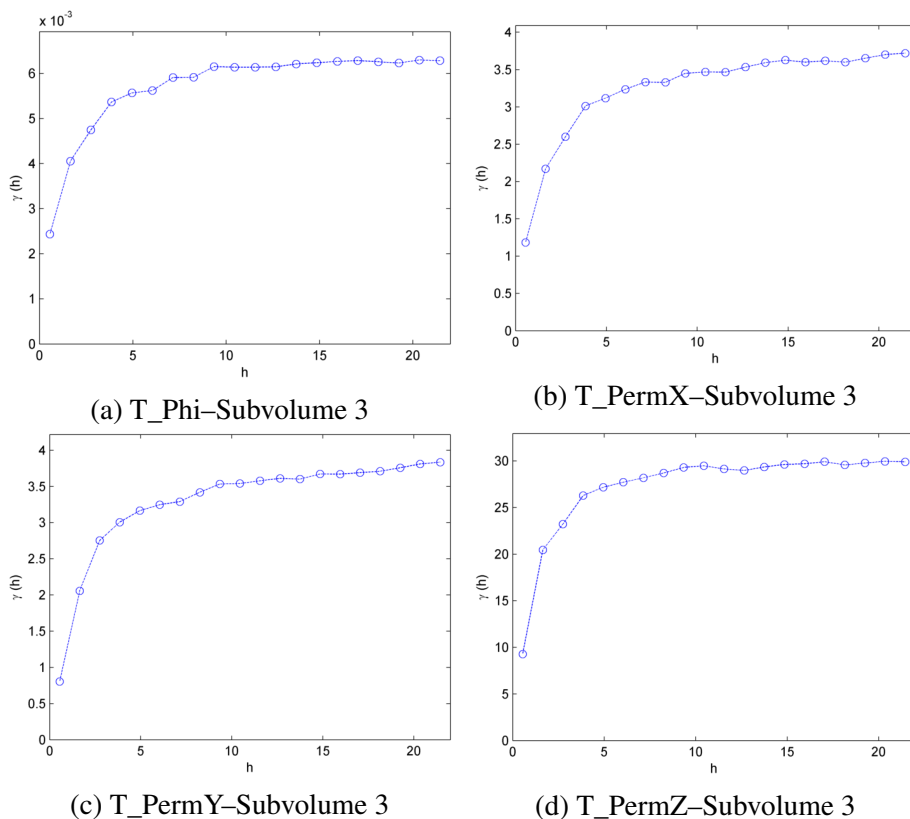


Fig. 4.20 3D variograms of the third (elongated towards Y-direction) subvolume (X:1–30, Y:131–200, Z:11–30) for porosity and permeability of the Tarbert formation.

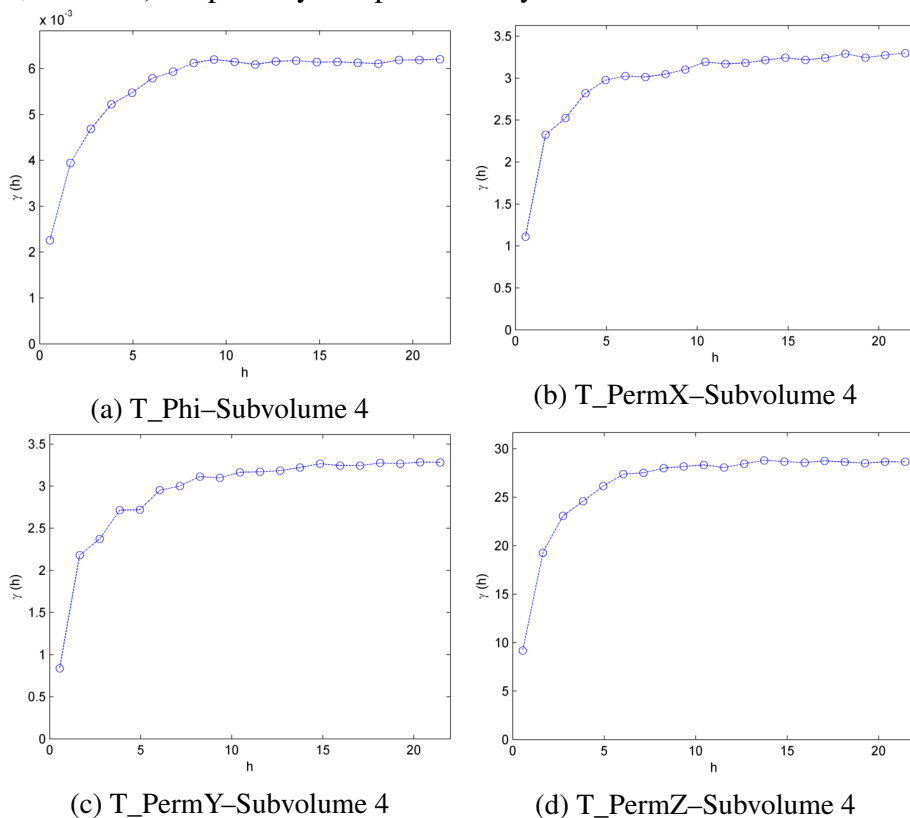


Fig. 4.21 3D variograms of the fourth (elongated towards Z-direction) subvolume (X:36–55, Y:131–200, Z:1–35) for porosity and permeability of the Tarbert formation.

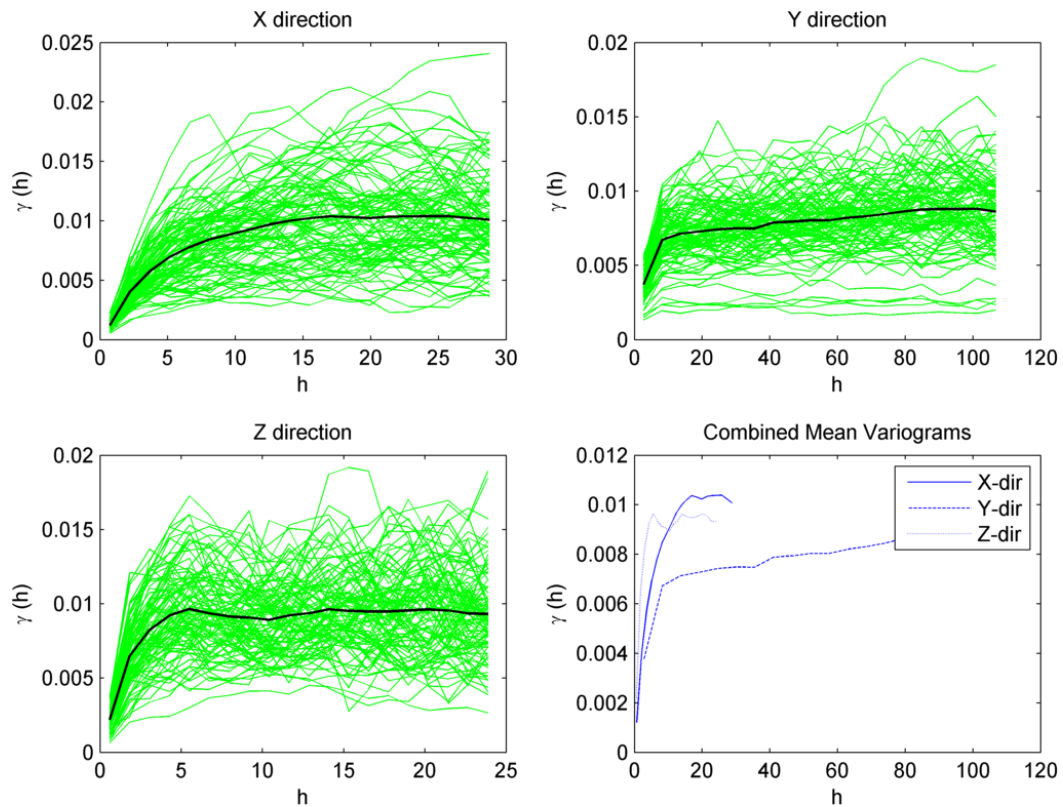


Fig. 4.22 Combined marginal variograms of 100 core samples for porosity of Upper Ness formation, for the three principal directions. The black line represents the mean variogram.

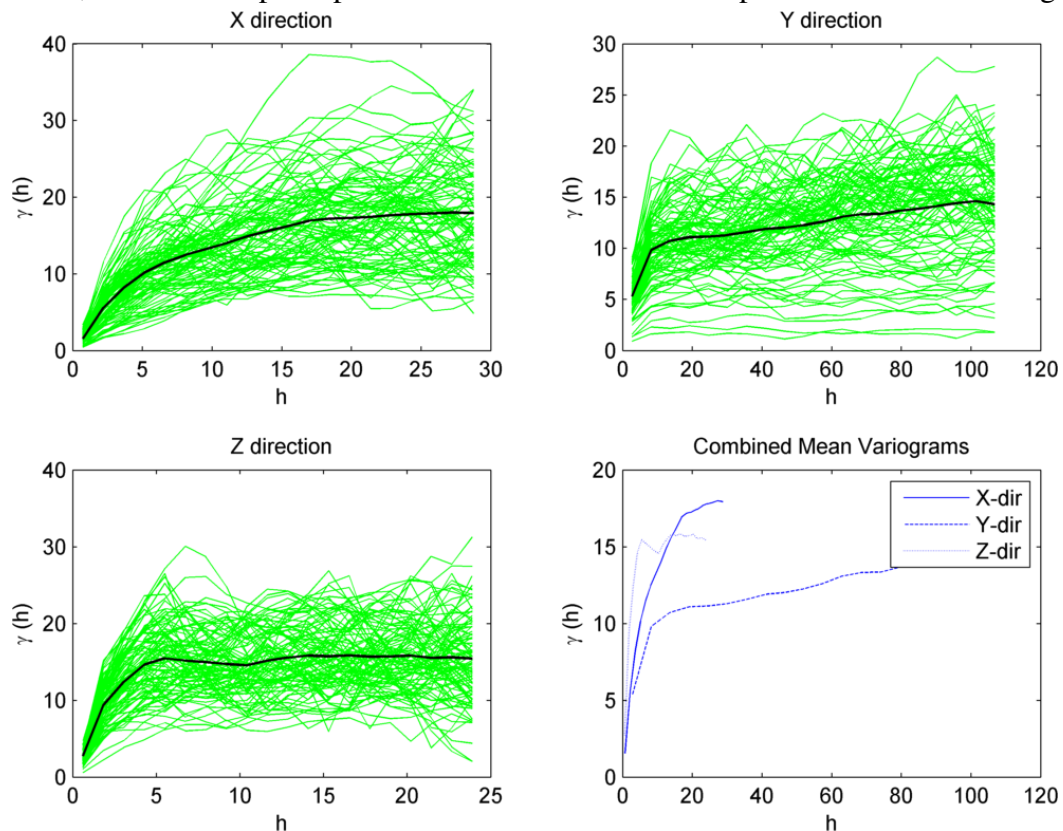


Fig. 4.23 Combined marginal variograms of 100 core samples for permeability of X-direction of Upper Ness formation, for the three principal directions. The black line represents the mean variogram.

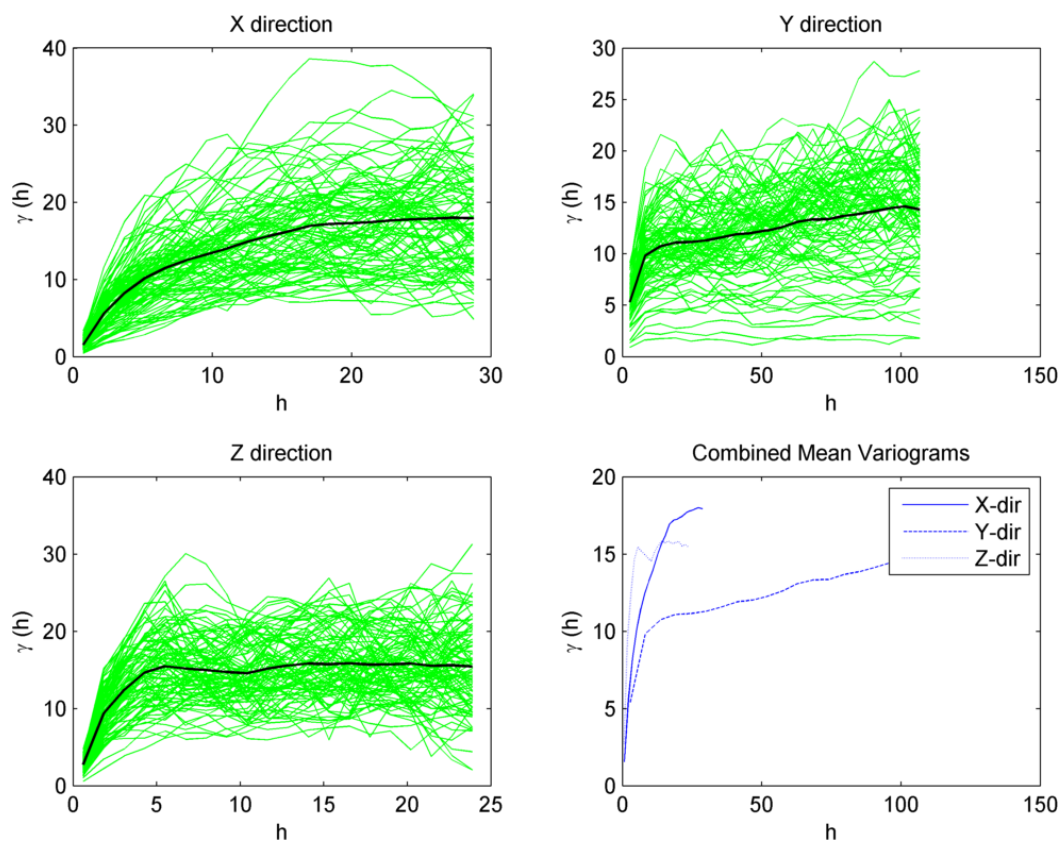


Fig. 4.24 Combined marginal variograms of 100 core samples for permeability of Y-direction of Upper Ness formation, for the three principal directions. The black line represents the mean variogram.

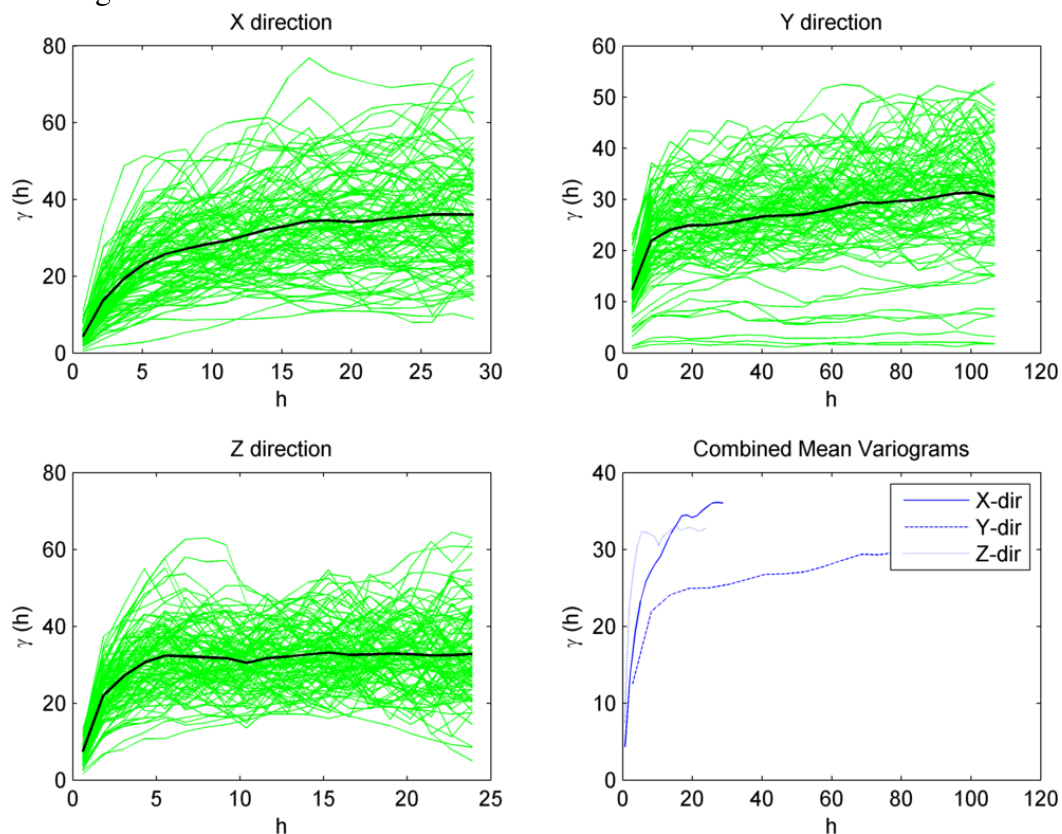


Fig. 4.25 Combined marginal variograms of 100 core samples for permeability of Z-direction of Upper Ness formation, for the three principal directions. The black line represents the mean variogram.

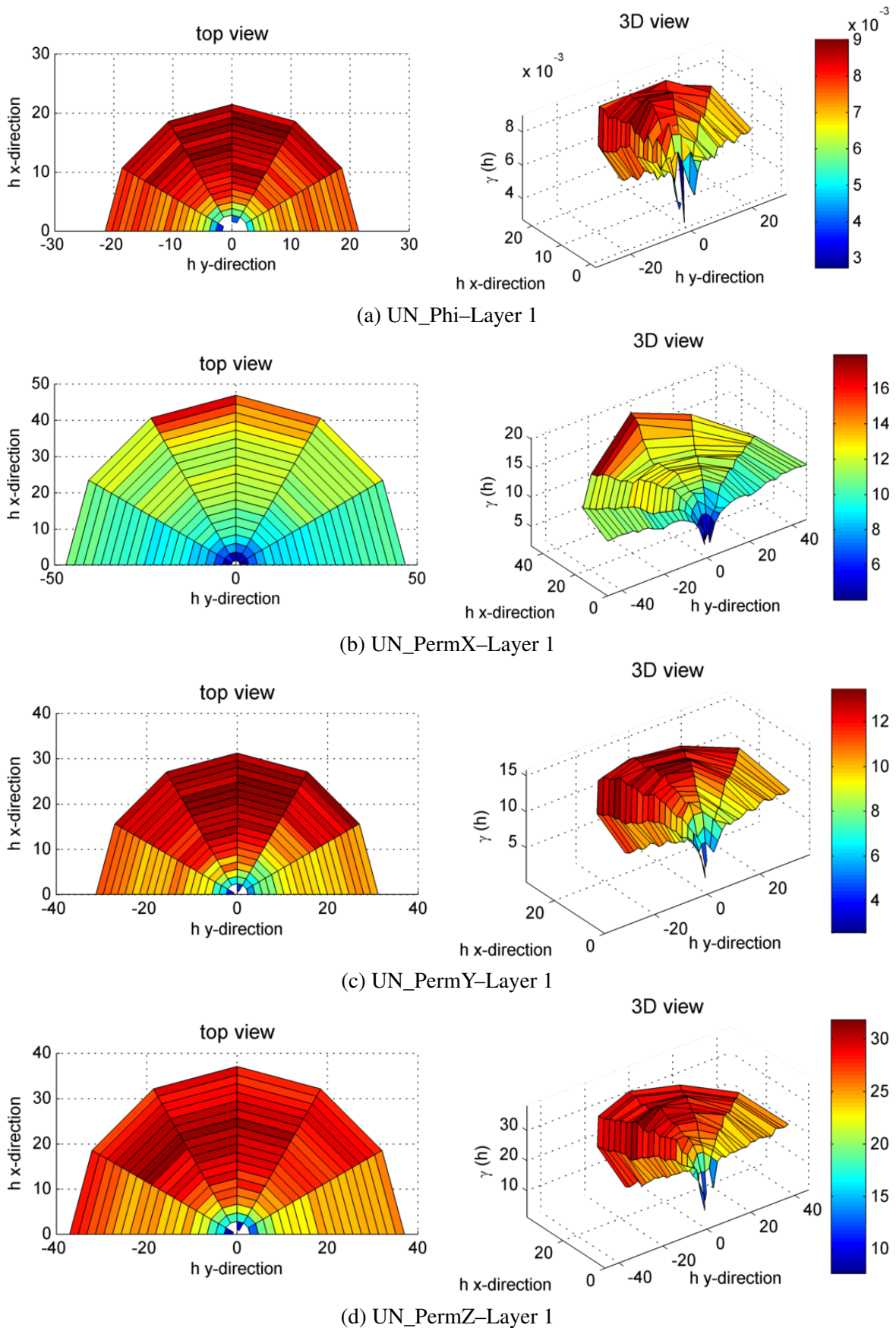
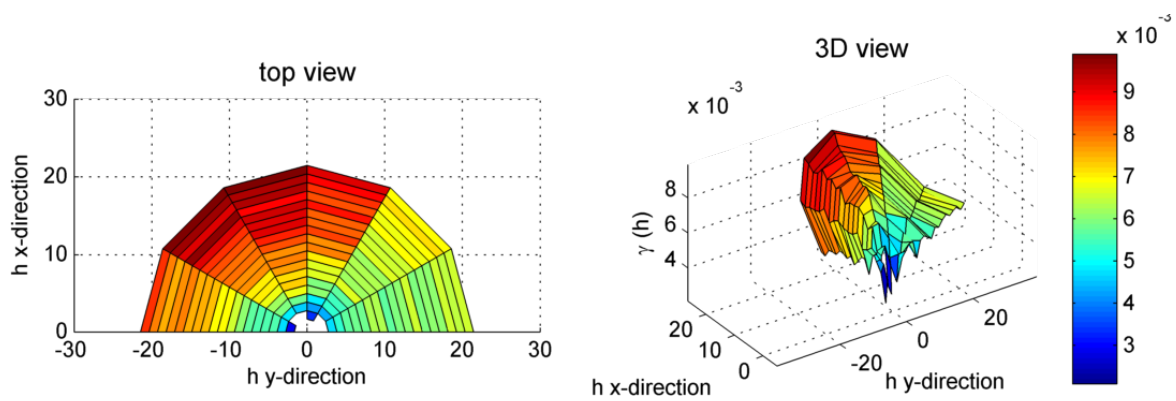
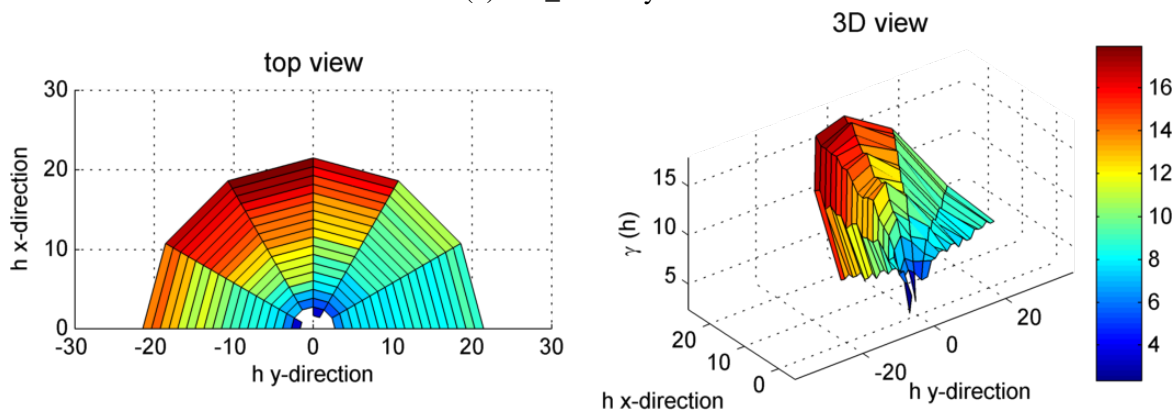


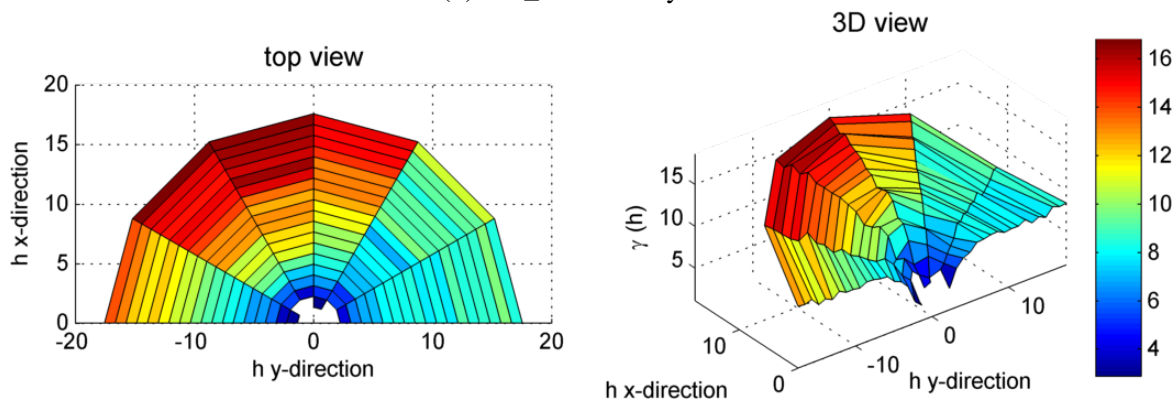
Fig. 4.26 Top and 3D view of anisotropic variogram of the first (bottom) layer for porosity and permeability of the Upper Ness formation.



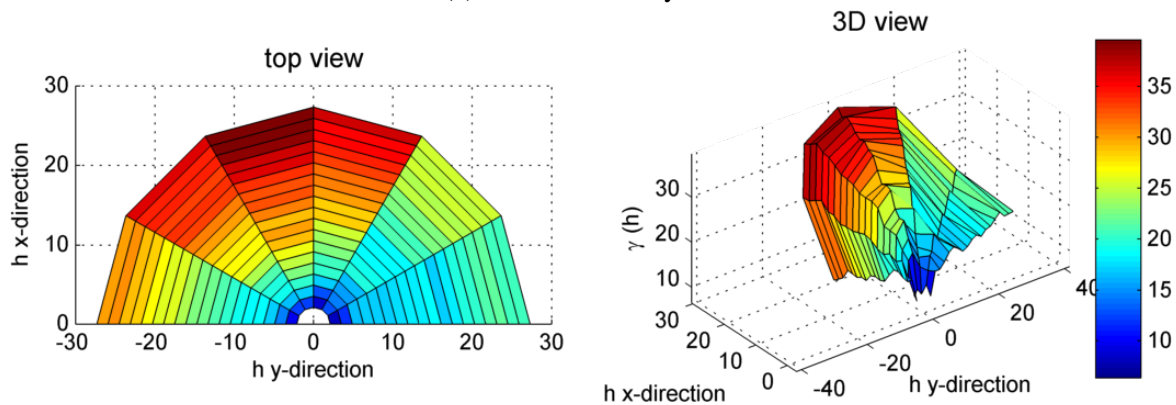
(a) UN_Phi-Layer 10



(b) UN_PermX-Layer 10



(c) UN_PermY-Layer 10



(d) UN_PermZ-Layer 10

Fig. 4.27 Top and 3D view of anisotropic variogram of the 10th layer for porosity and permeability of the Upper Ness formation.

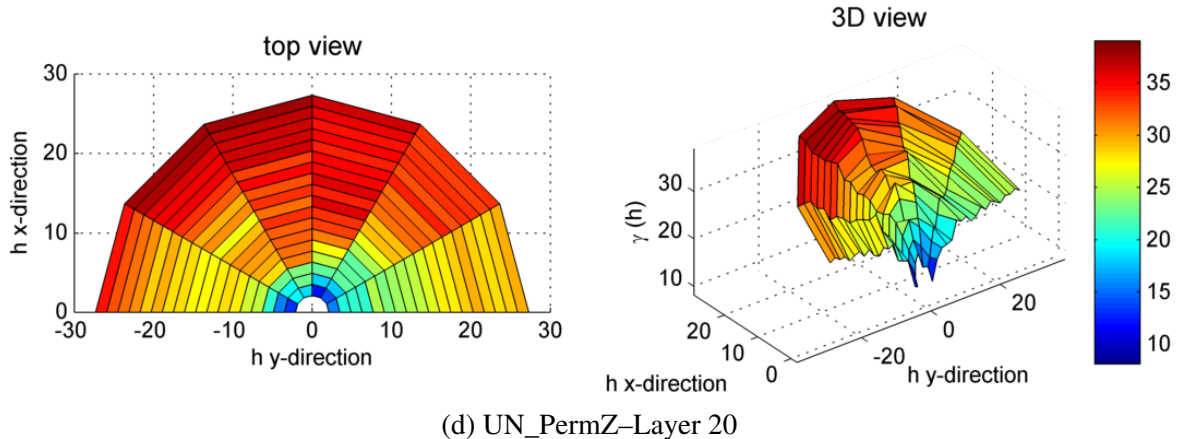
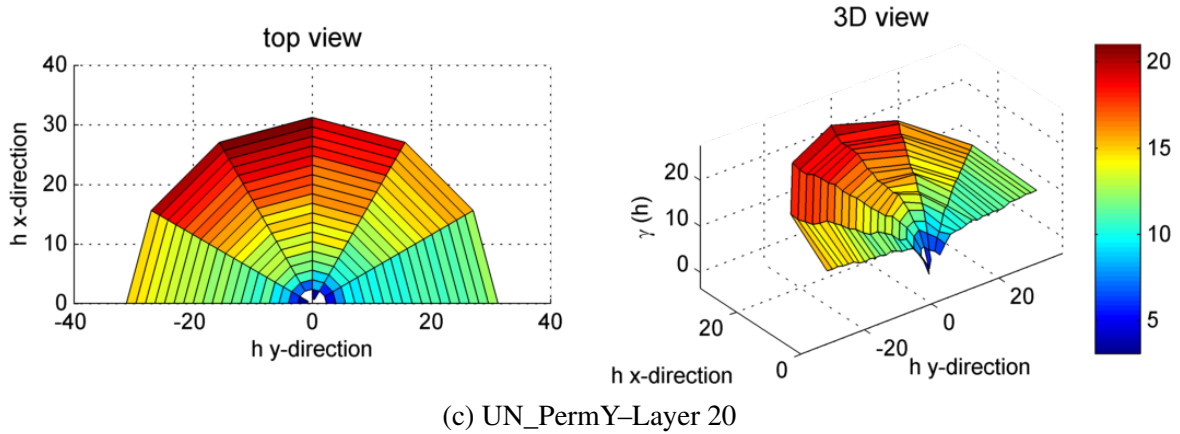
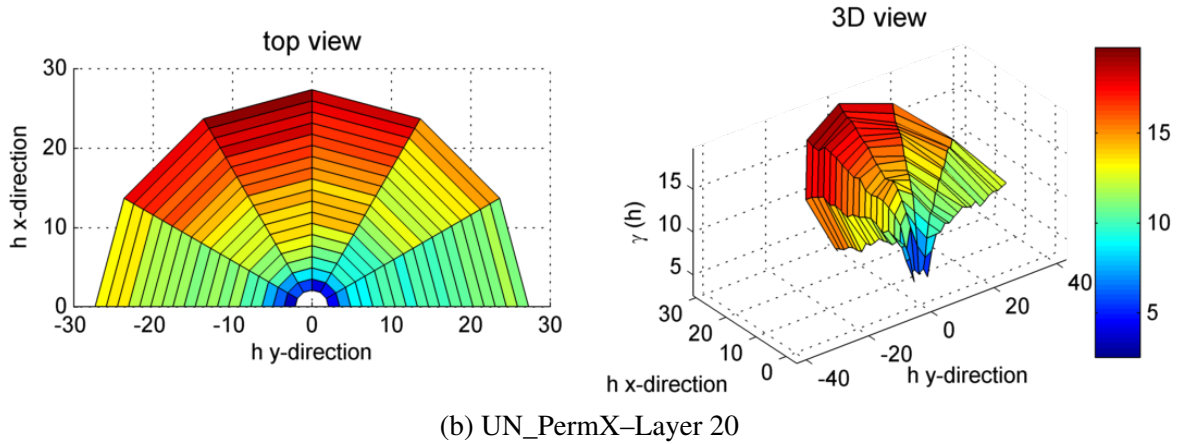
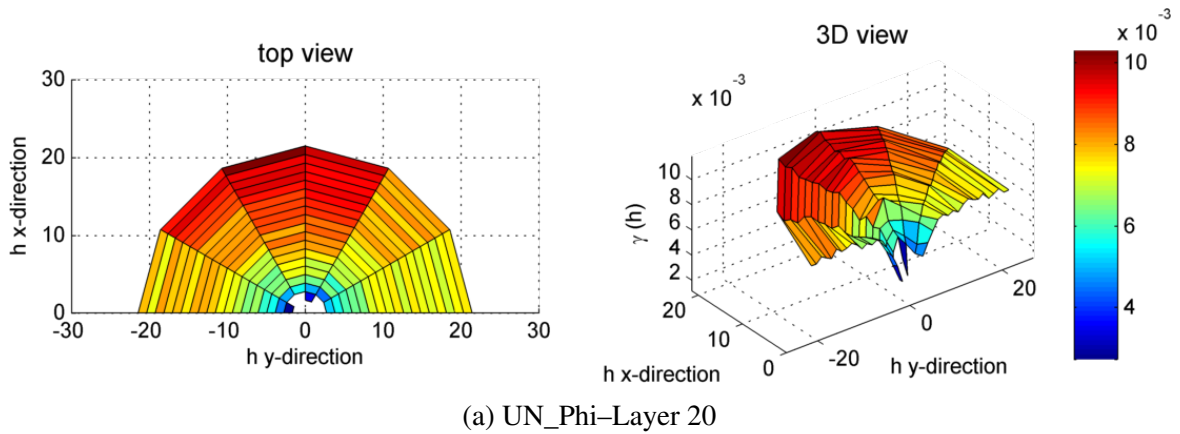
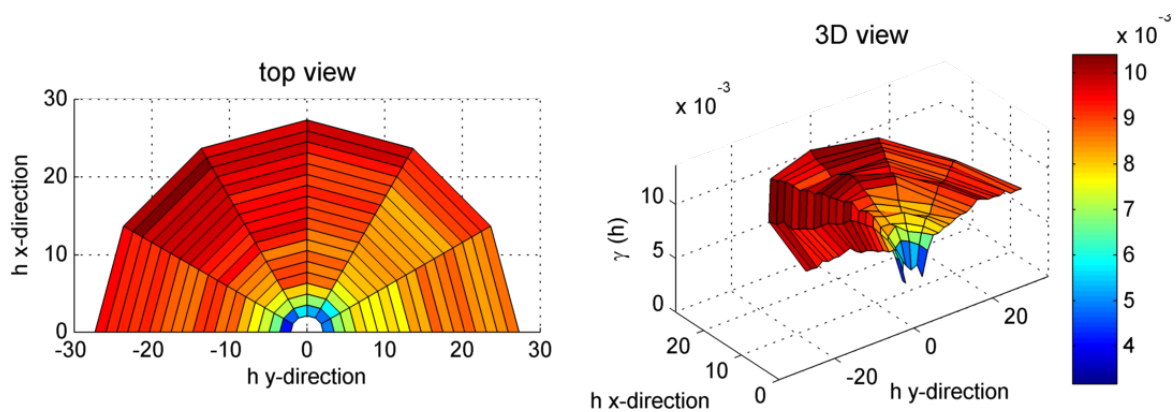
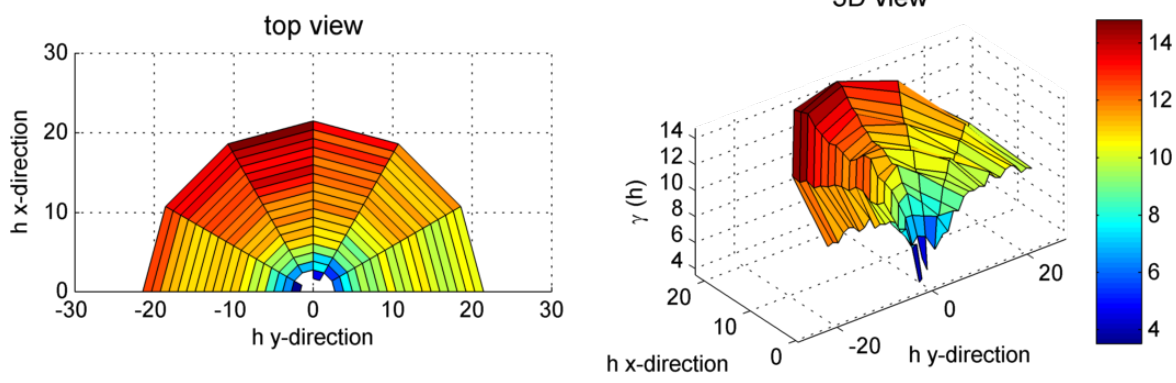


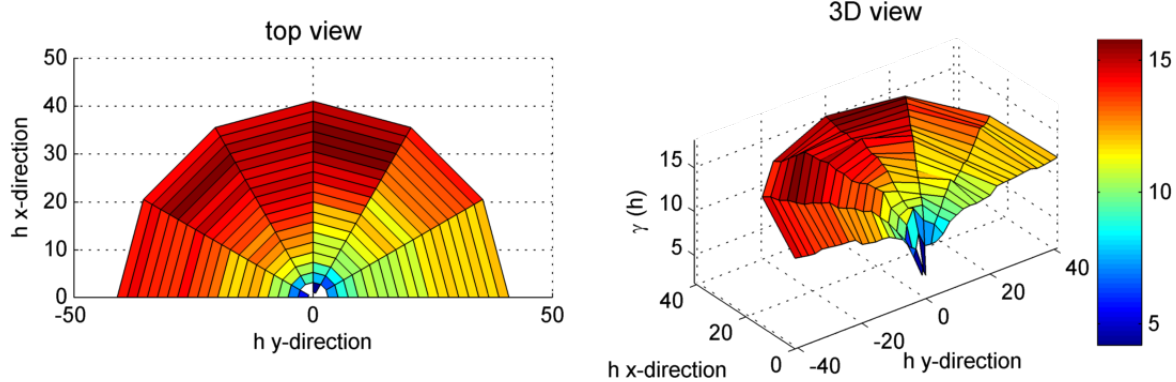
Fig. 4.28 Top and 3D view of anisotropic variogram of the 20th layer for porosity and permeability of the Upper Ness formation.



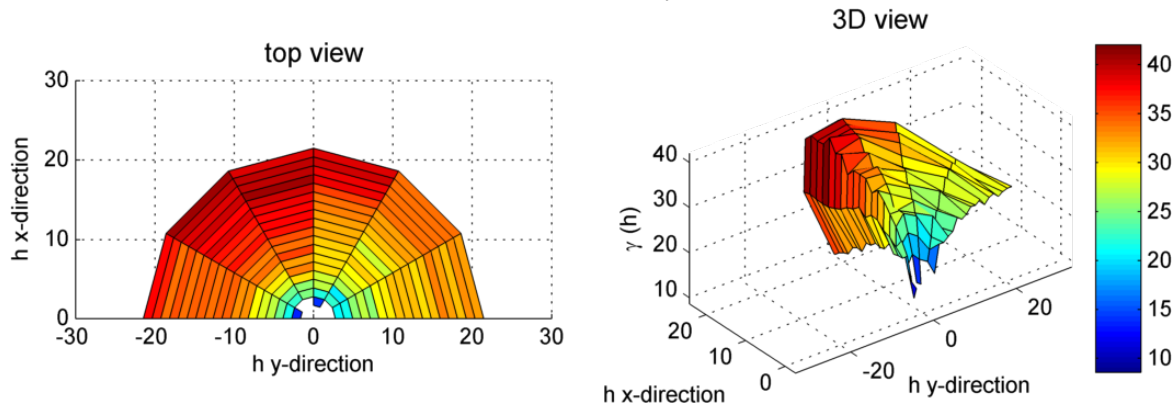
(a) UN_Phi-Layer 30



(b) UN_PermX-Layer 30

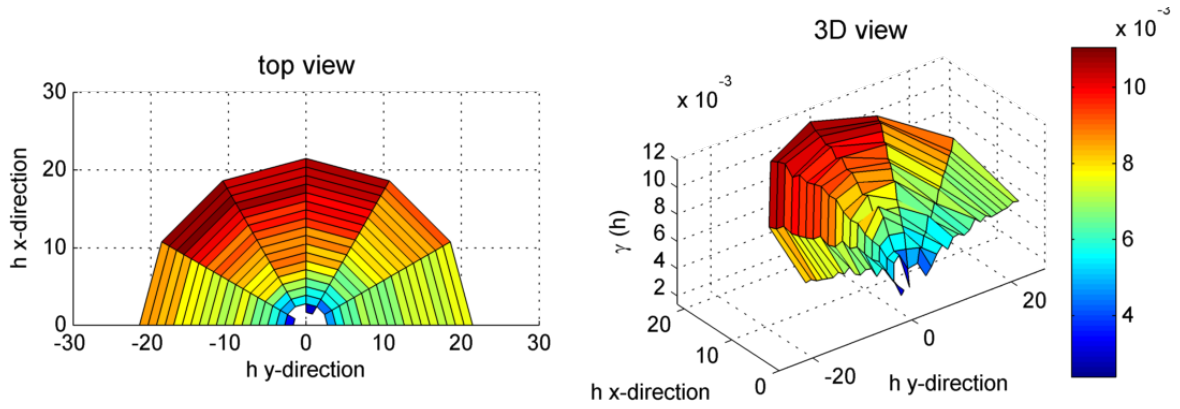


(c) UN_PermY-Layer 30

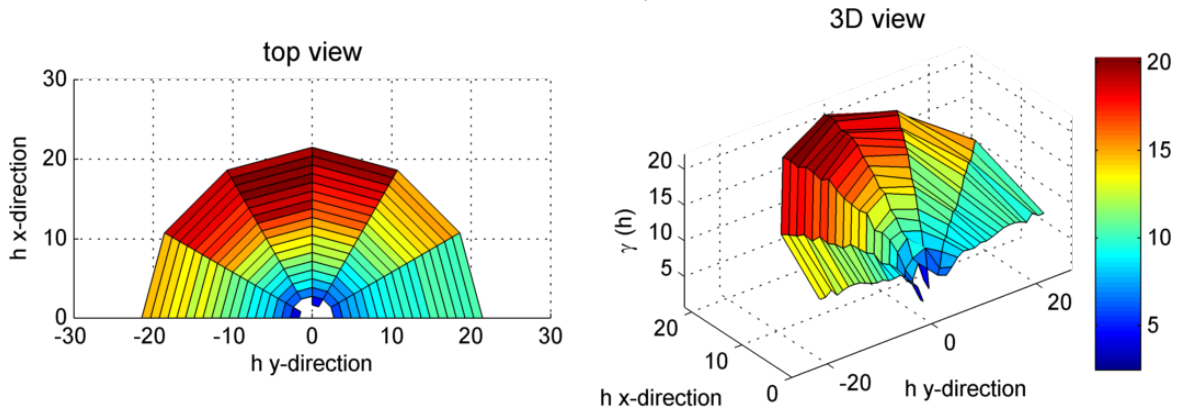


(d) UN_PermZ-Layer 30

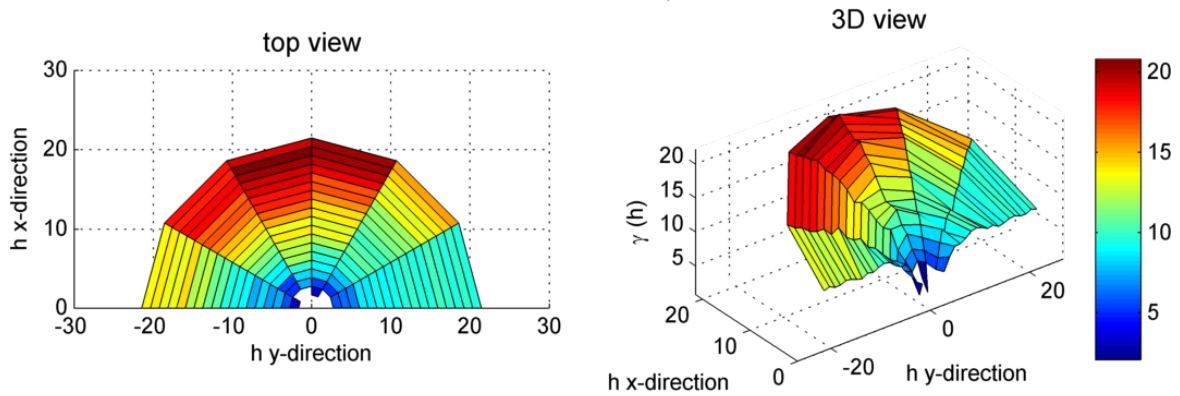
Fig. 4.29 Top and 3D view of anisotropic variogram of the 30th layer for porosity and permeability of the Upper Ness formation.



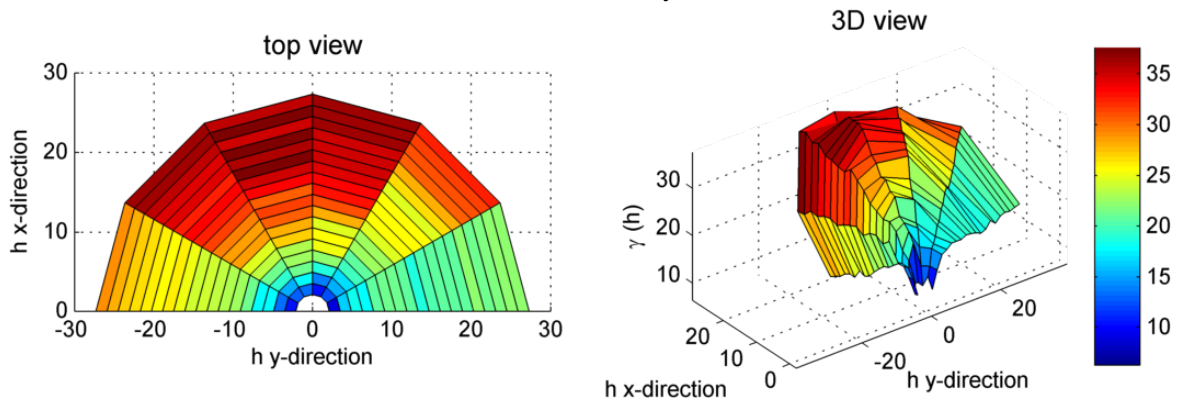
(a) UN_Phi-Layer 40



(b) UN_PermX-Layer 40

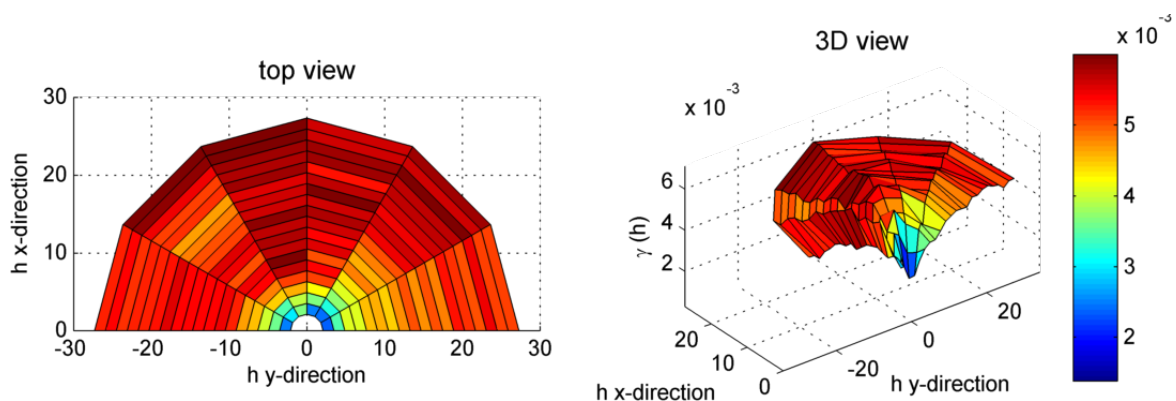


(c) UN_PermY-Layer 40

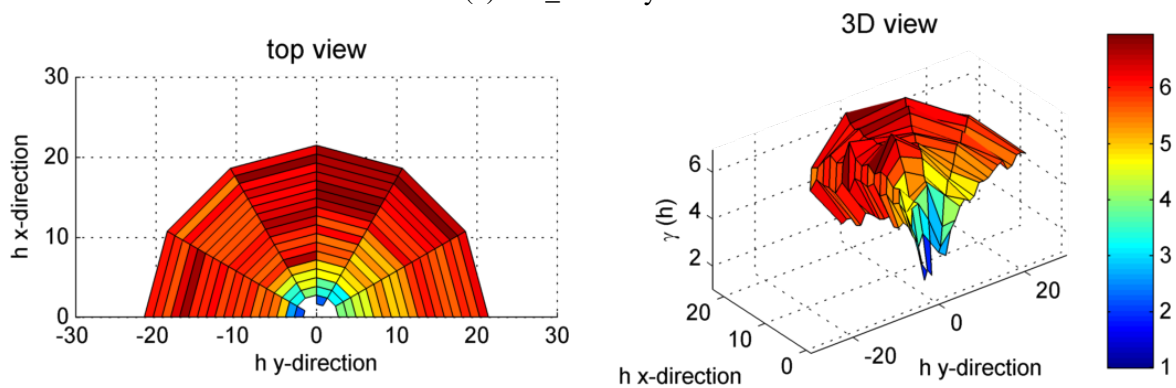


(d) UN_PermZ-Layer 40

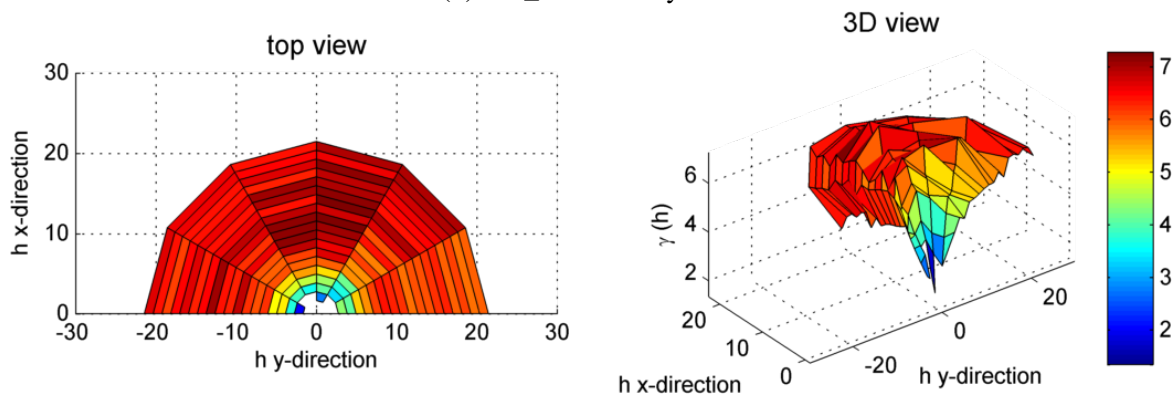
Fig. 4.30 Top and 3D view of anisotropic variogram of the 40th layer for porosity and permeability of the Upper Ness formation.



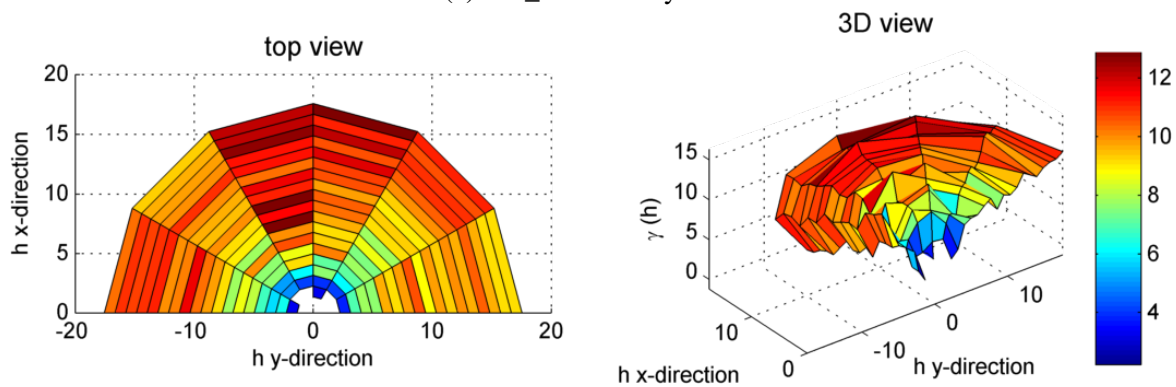
(a) UN_Phi-Layer 50



(b) UN_PermX-Layer 50



(c) UN_PermY-Layer 50



(d) UN_PermZ-Layer 50

Fig. 4.31 Top and 3D view of anisotropic variogram of the 50th (top) layer for porosity and permeability of the Upper Ness formation.

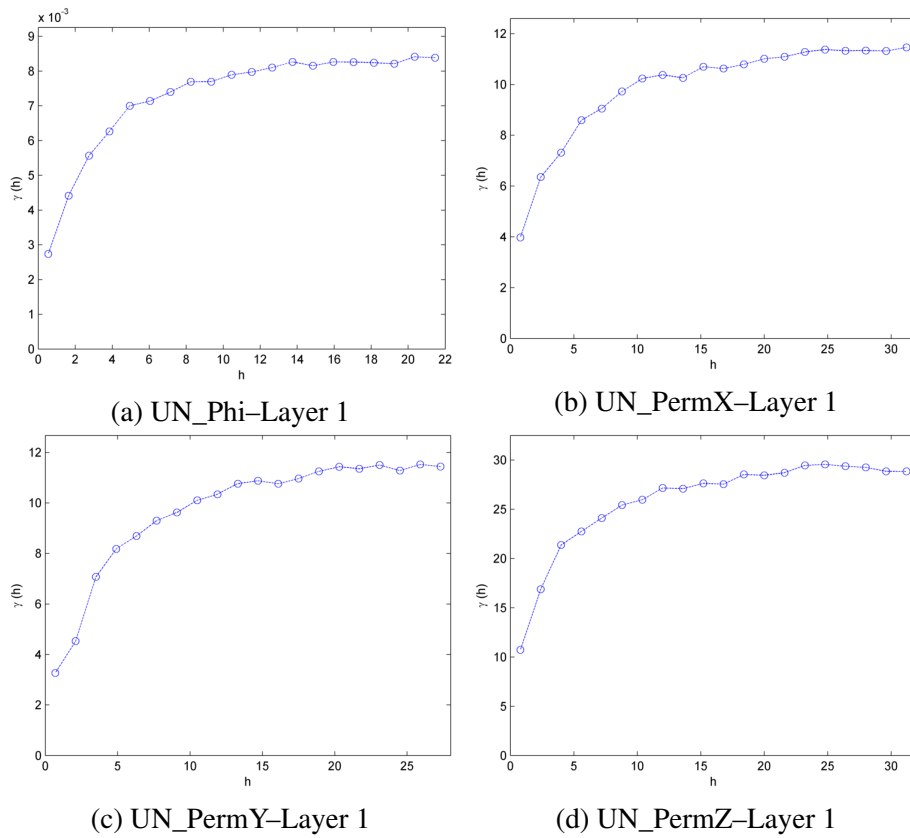


Fig. 4.32 Omnidirectional variograms of the first (bottom) layer for porosity and permeability of the Upper Ness formation.

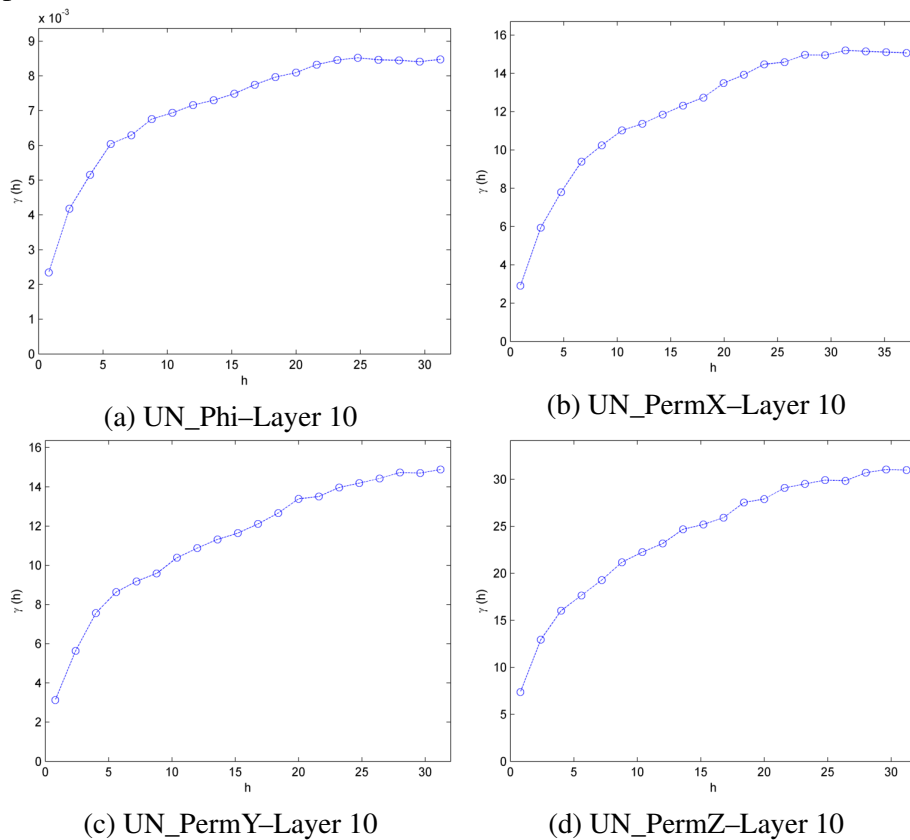


Fig. 4.33 Omnidirectional variograms of the 10th layer for porosity and permeability of the Upper Ness formation.

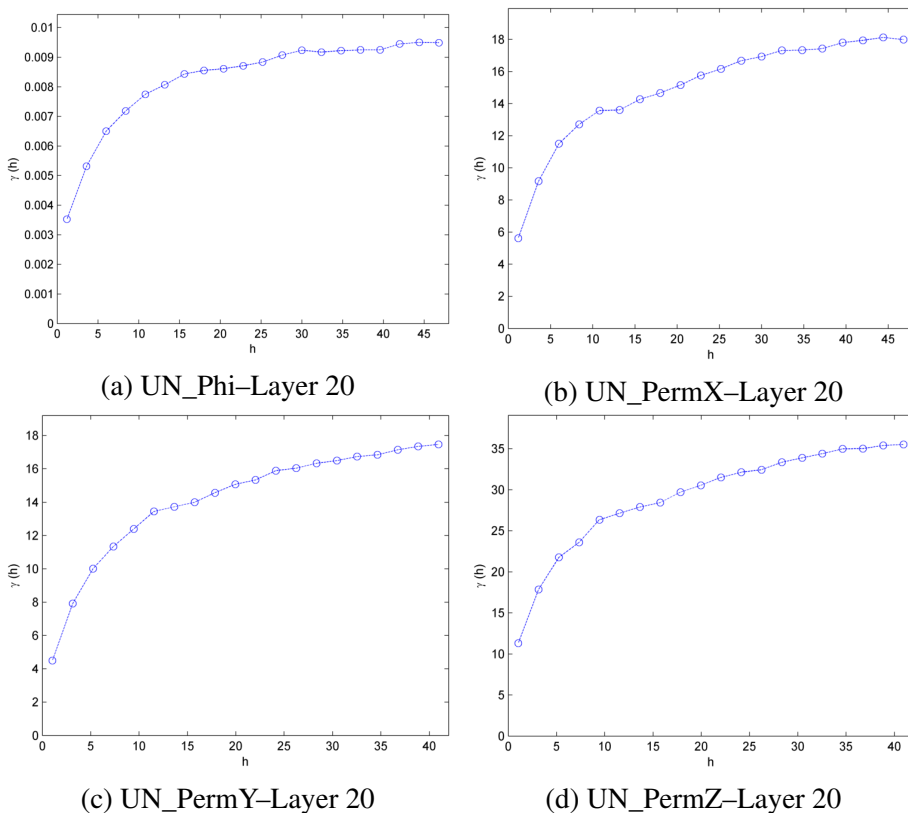


Fig. 4.34 Omnidirectional variograms of the 20th layer for porosity and permeability of the Upper Ness formation.

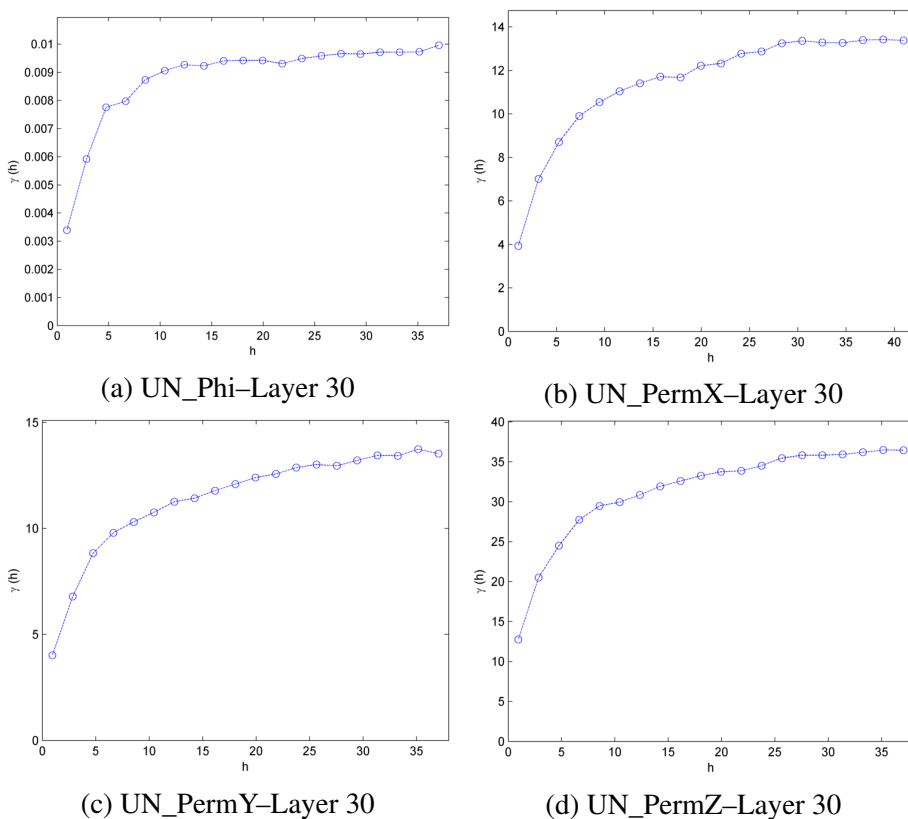


Fig. 4.35 Omnidirectional variograms of the 30th layer for porosity and permeability of the Upper Ness formation.

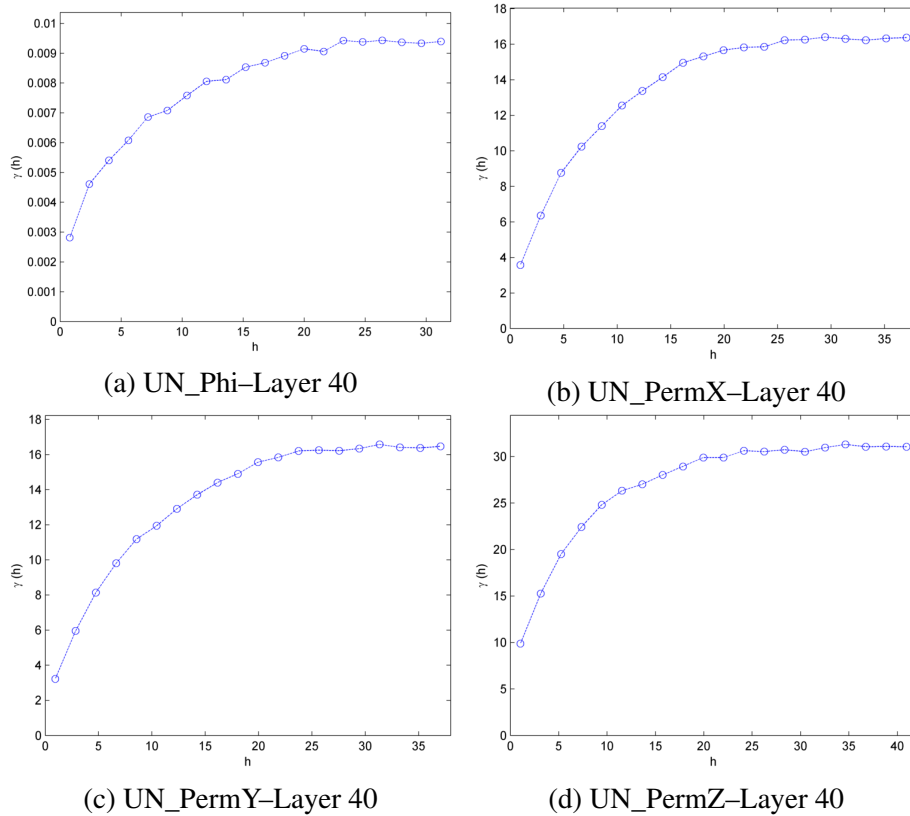


Fig. 4.36 Omnidirectional variograms of the 40th layer for porosity and permeability of the Upper Ness formation.

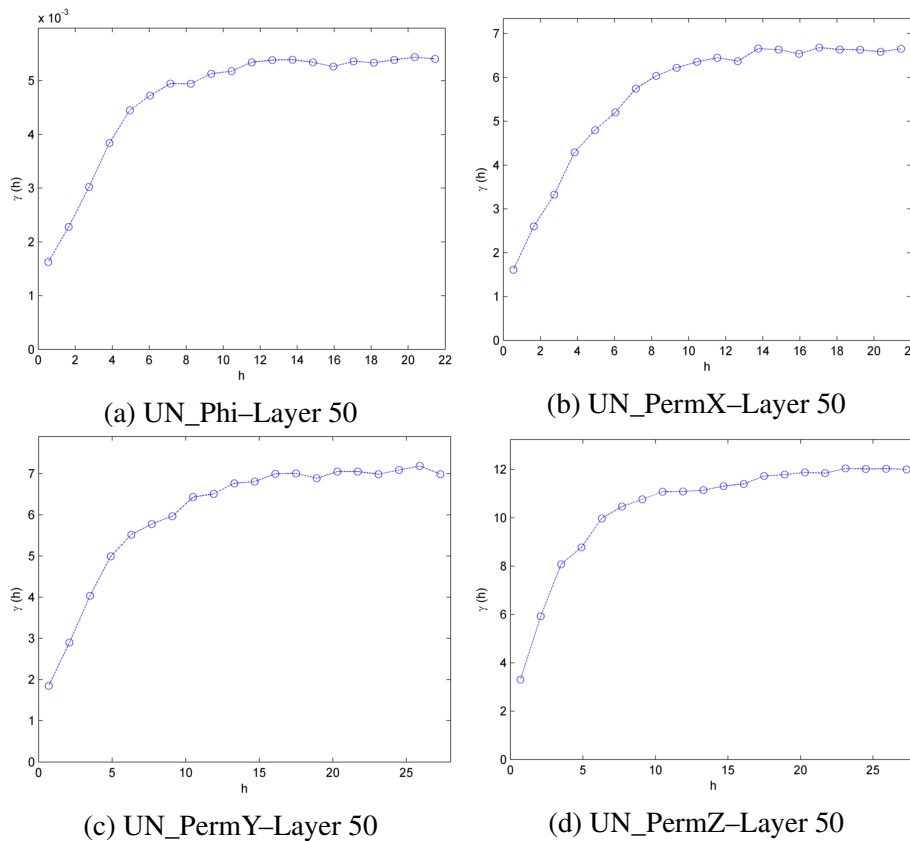


Fig. 4.37 Omnidirectional variograms of the 50th (top) layer for porosity and permeability of the Upper Ness formation.

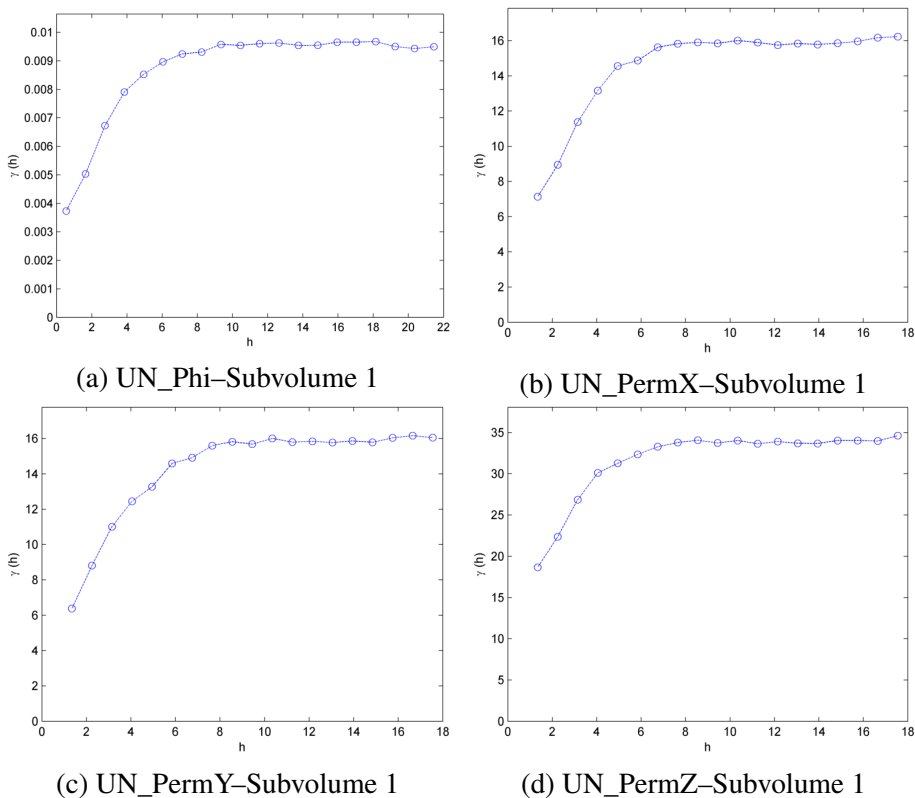


Fig. 4.38 3D variograms of the first (basic) subvolume (X:6–25, Y:21–90, Z:11–40) for porosity and permeability of the Upper Ness formation.

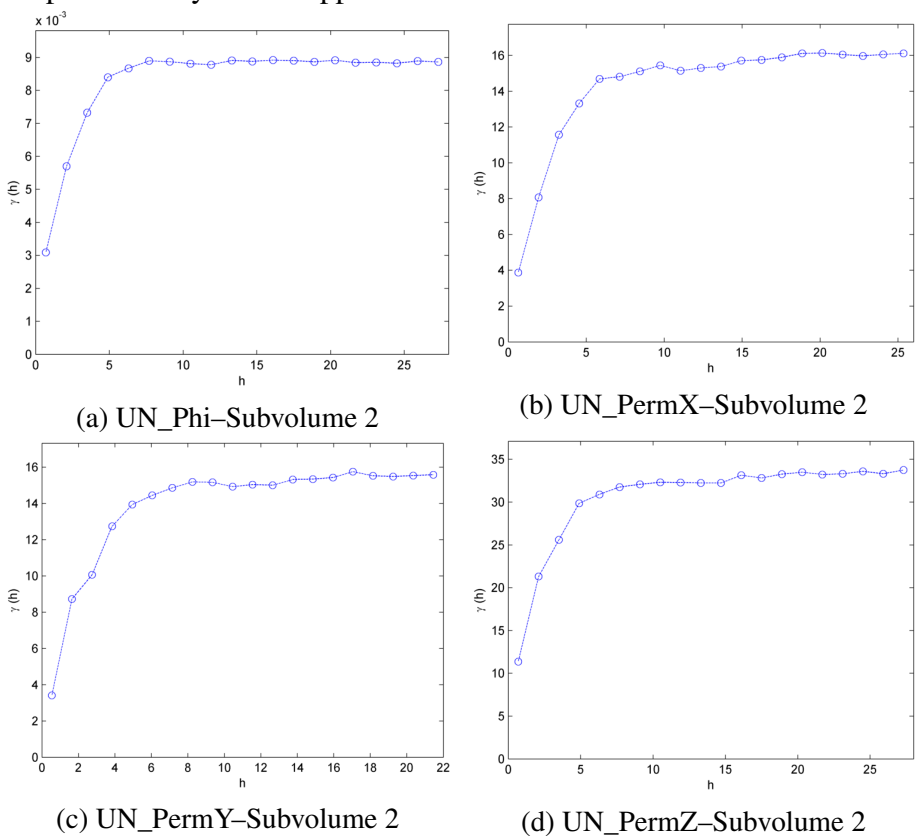


Fig. 4.39 3D variograms of the second (elongated towards X-direction) subvolume (X:36–55, Y:1–110, Z:11–40) for porosity and permeability of the Upper Ness formation.

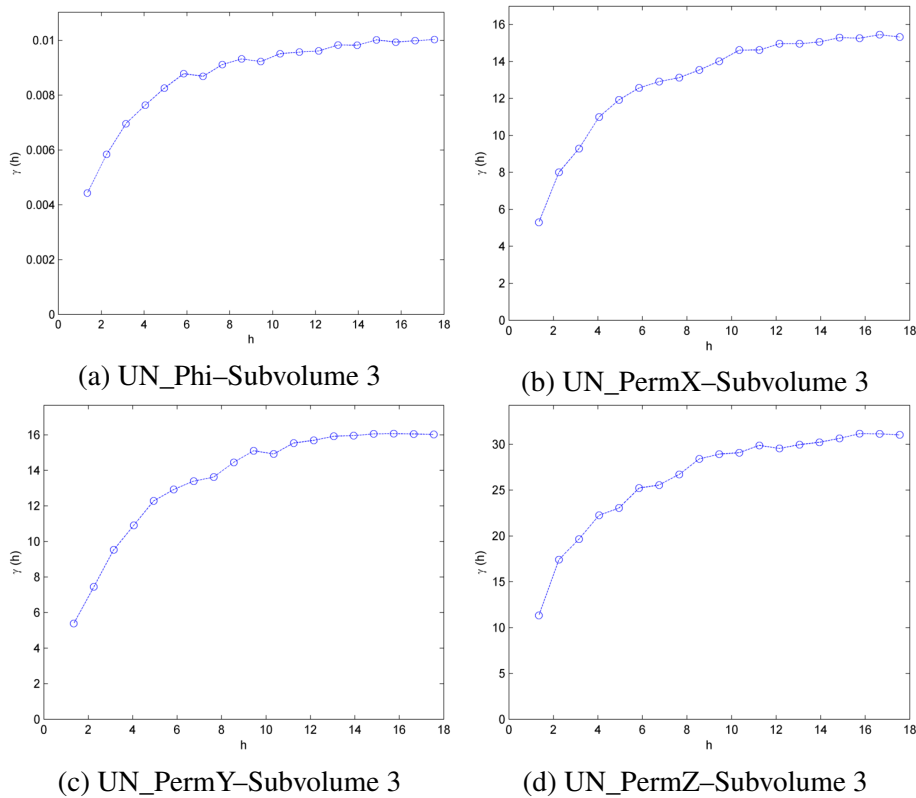


Fig. 4.40 3D variograms of the third (elongated towards Y–direction) subvolume (X:1–30, Y:131–200, Z:11–40) for porosity and permeability of the Upper Ness formation.

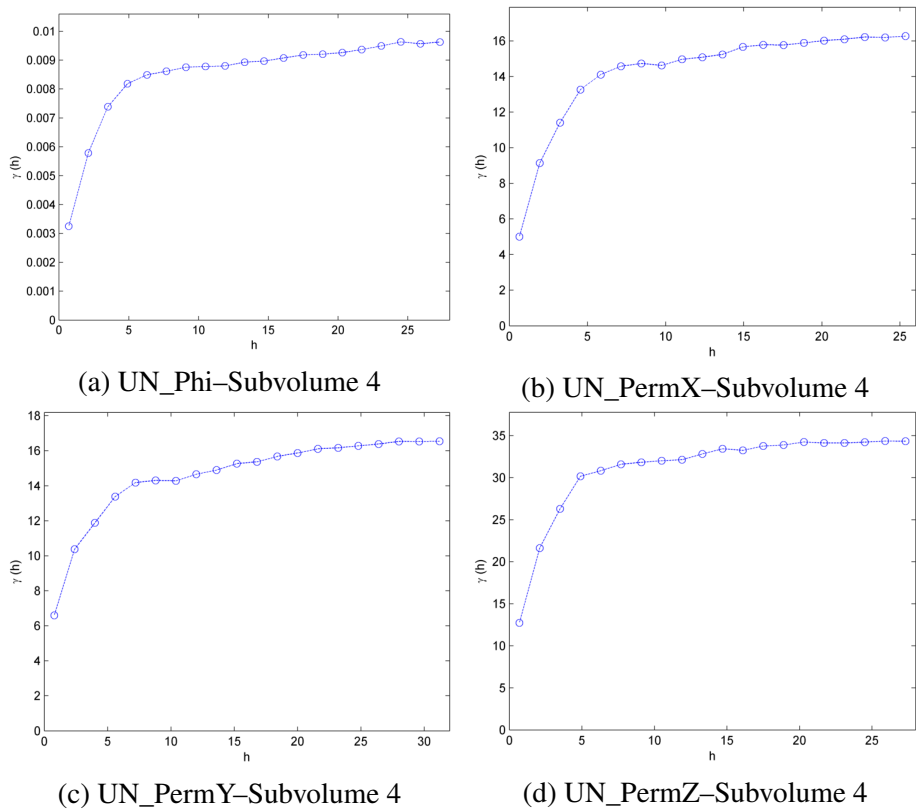


Fig. 4.41 3D variograms of the fourth (elongated towards Z–direction) subvolume (X:36–55, Y:131–200, Z:1–50) for porosity and permeability of the Upper Ness formation.

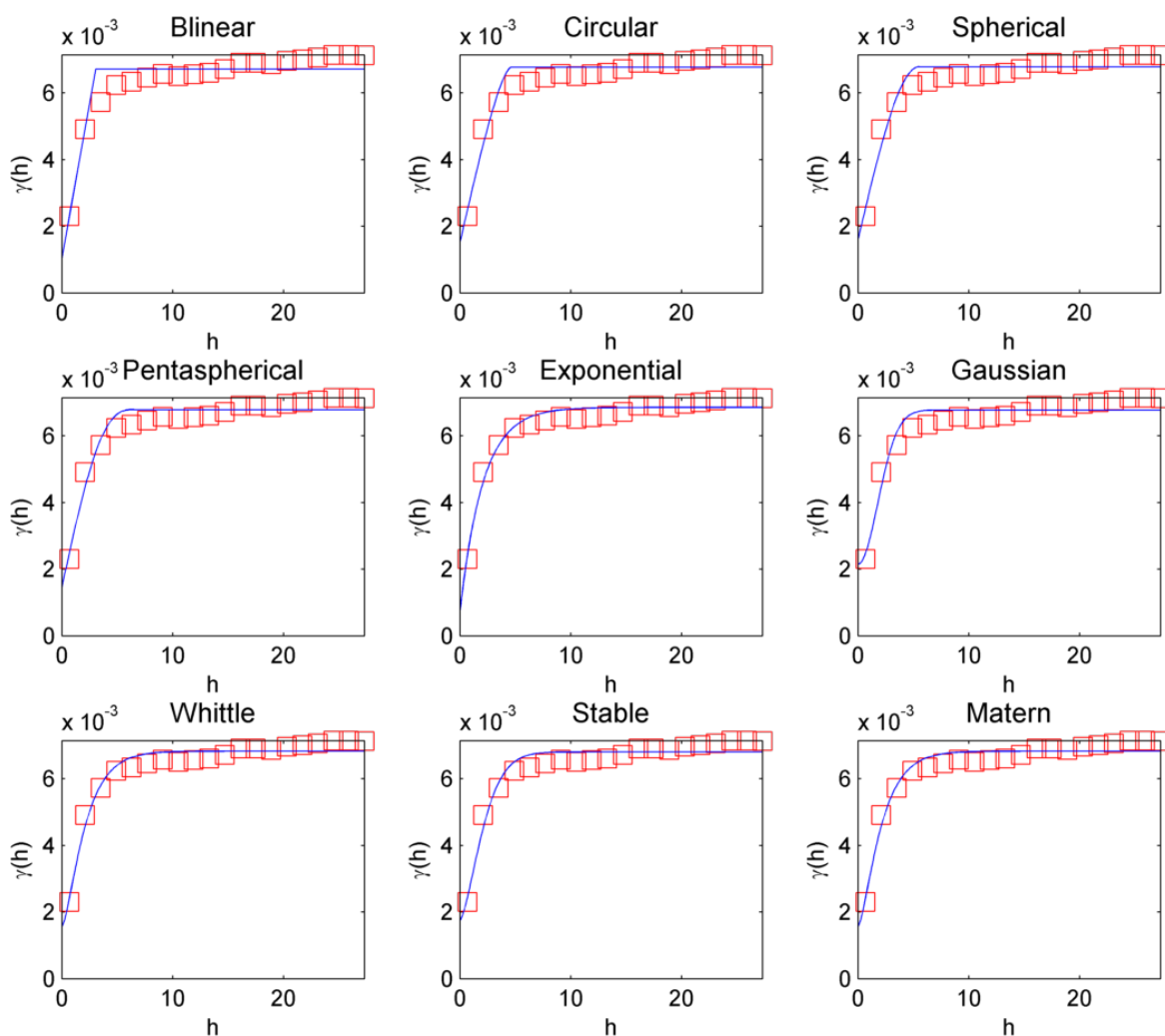


Fig. 4.42 Different theoretical variogram models fitted to the 3D variogram of the first Subvolume of porosity for Tarbert formation. Exponential model is the best fit as justified in Table 4.1. Squares represent the experimental data and solid line represents the theoretical model.

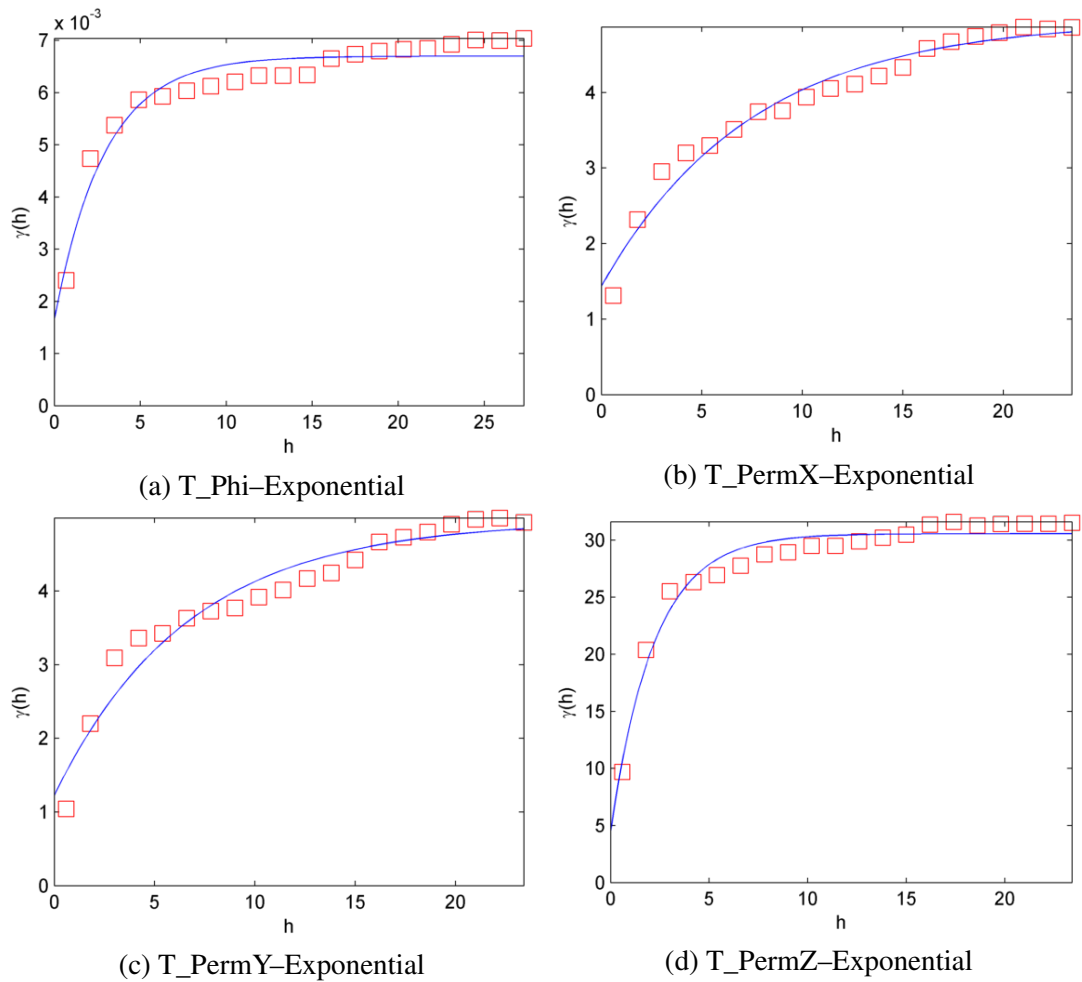


Fig. 4.43 Experimental variograms fitted to theoretical models, for the first Subvolume of porosity and permeability for Tarbert formation. Modelling parameters are presented in Table 4.2. Squares represent the experimental data and solid line represents the theoretical model.

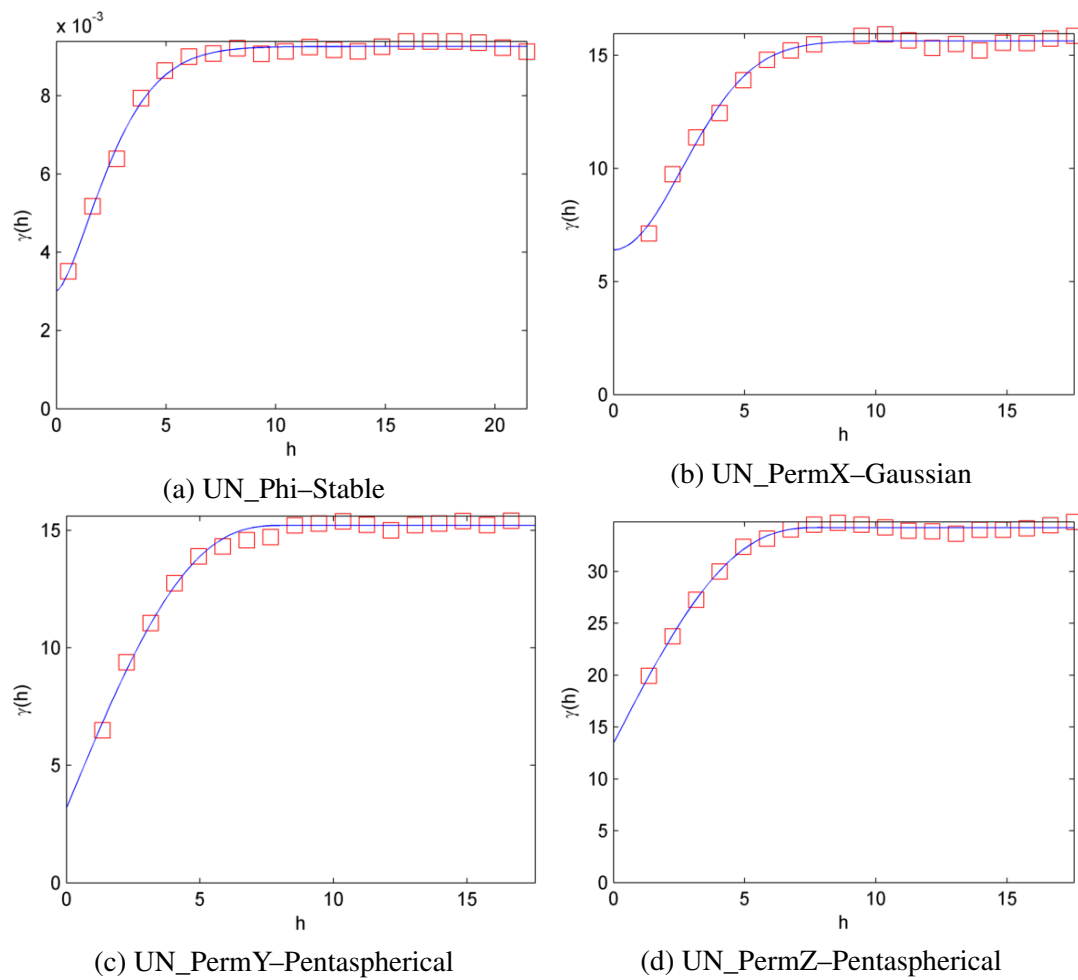


Fig. 4.44 Experimental variograms fitted to theoretical models, for the first Subvolume of porosity and permeability for Upper Ness formation. Modelling parameters are presented in Table 4.4. Squares represent the experimental data and solid line represents the theoretical model.

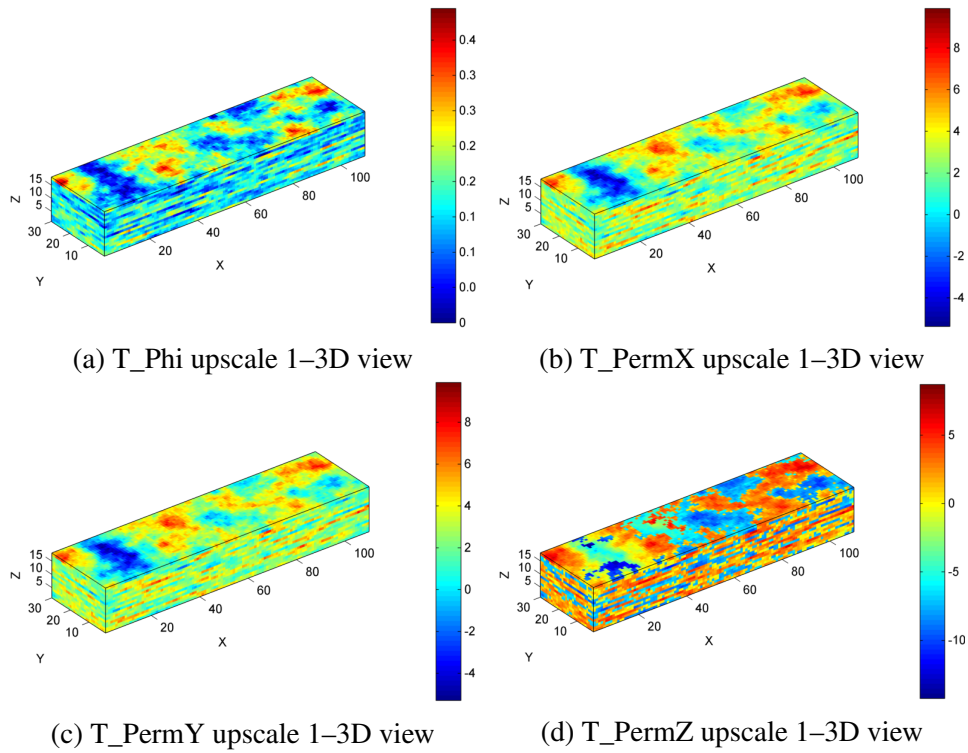


Fig. 4.45 3D images of porosity and permeability of the Tarbert formation after the first iteration of upscaling.

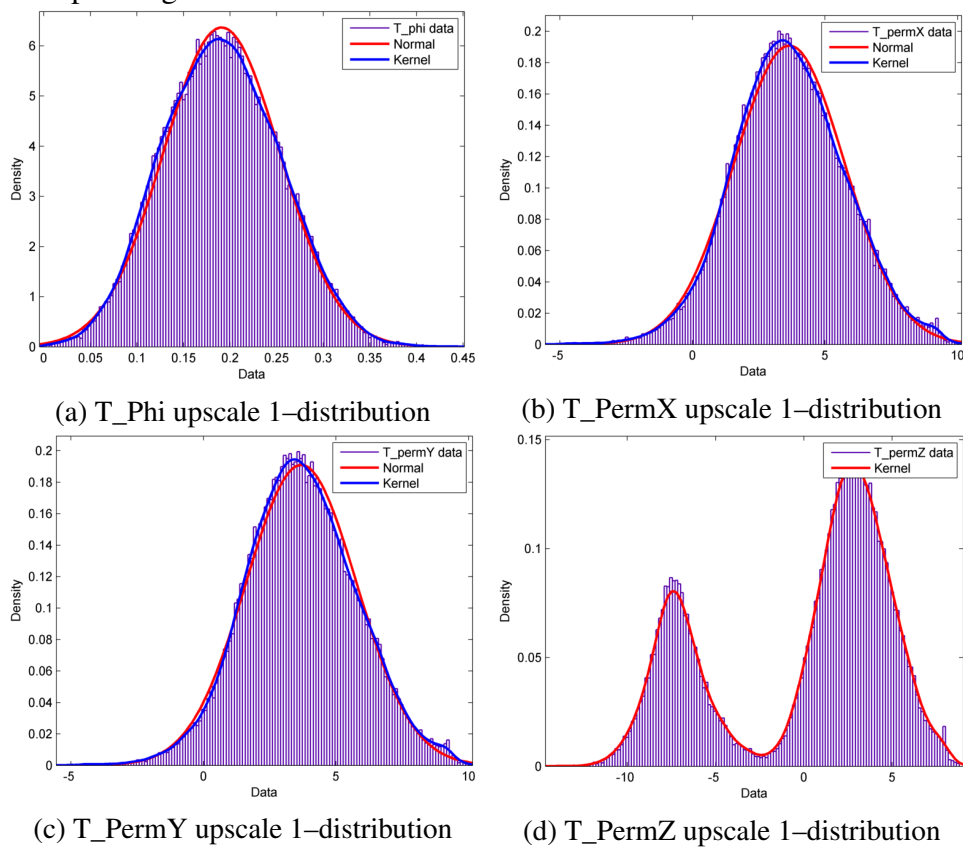


Fig. 4.46 Distribution of porosity and permeability data of the Tarbert formation after the first iteration of upscaling.

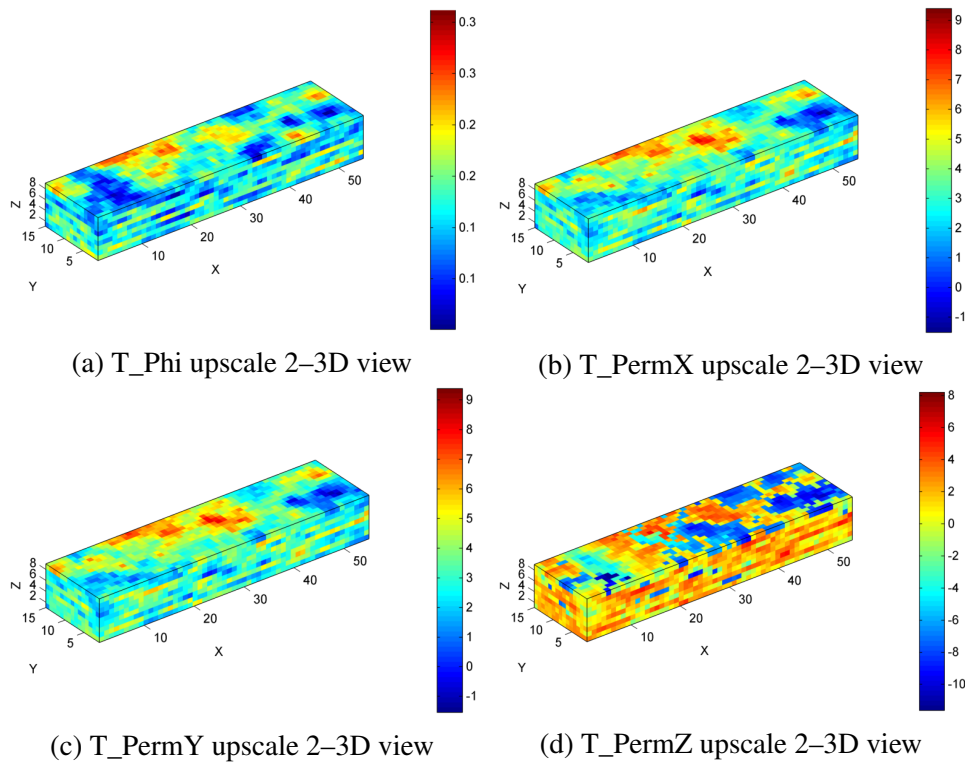


Fig. 4.47 3D images of porosity and permeability of the Tarbert formation after the second iteration of upscaling.

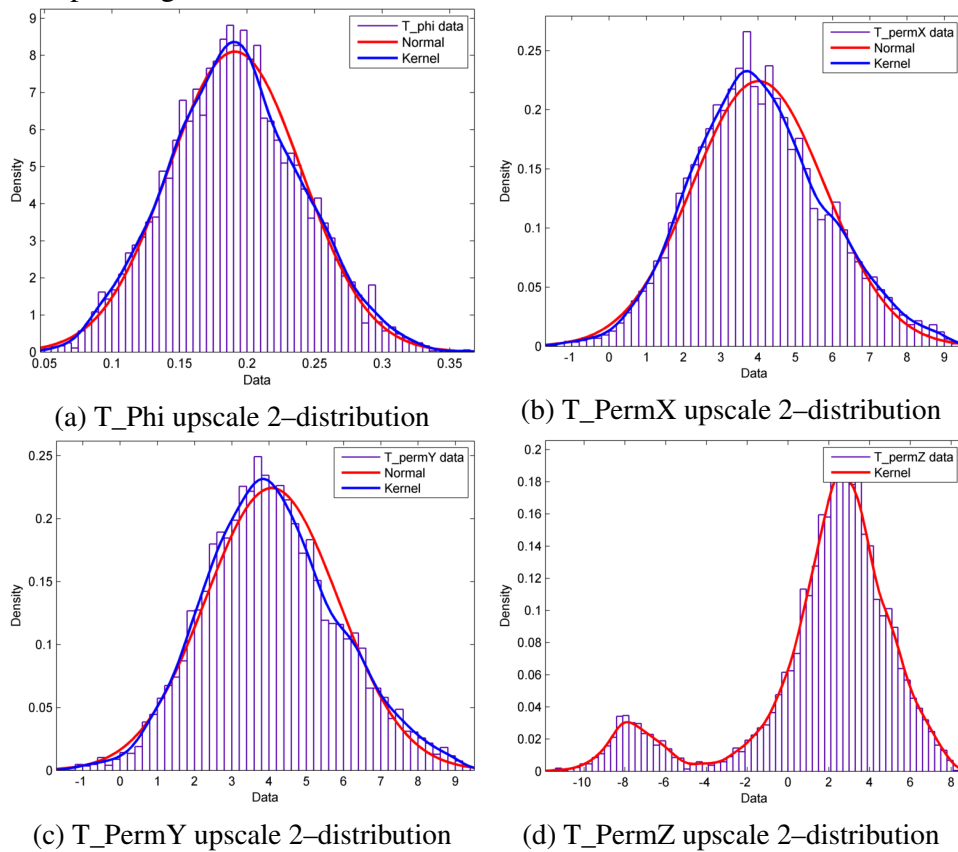


Fig. 4.48 Distribution of porosity and permeability data of the Tarbert formation after the second iteration of upscaling.

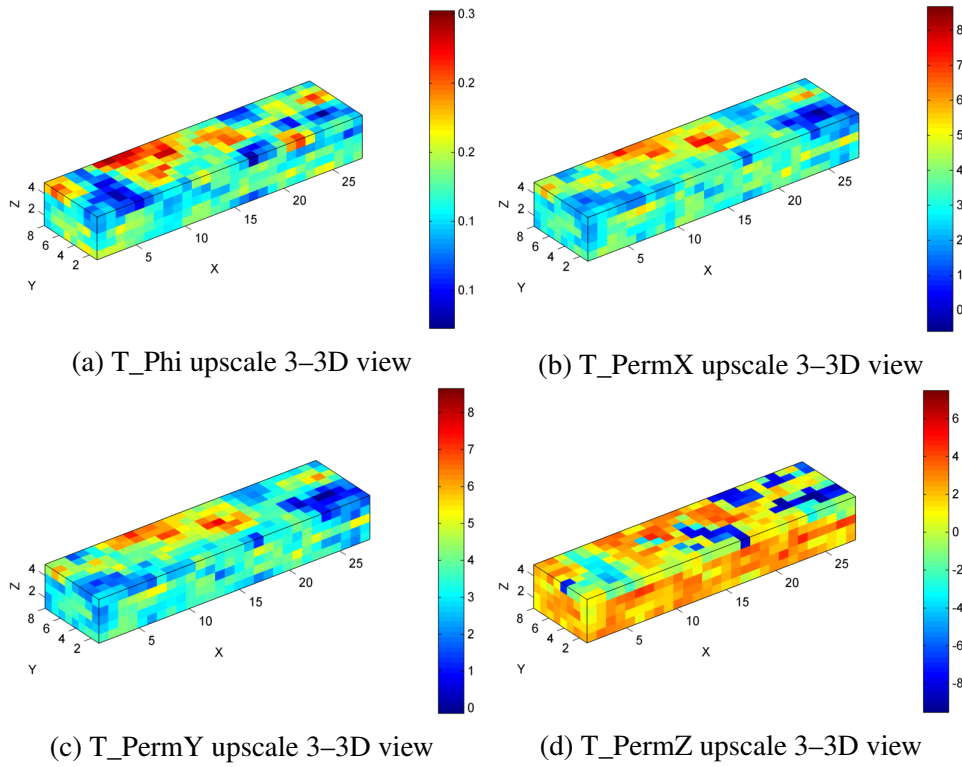


Fig. 4.49 3D images of porosity and permeability of the Tarbert formation after the third iteration of upscaling.

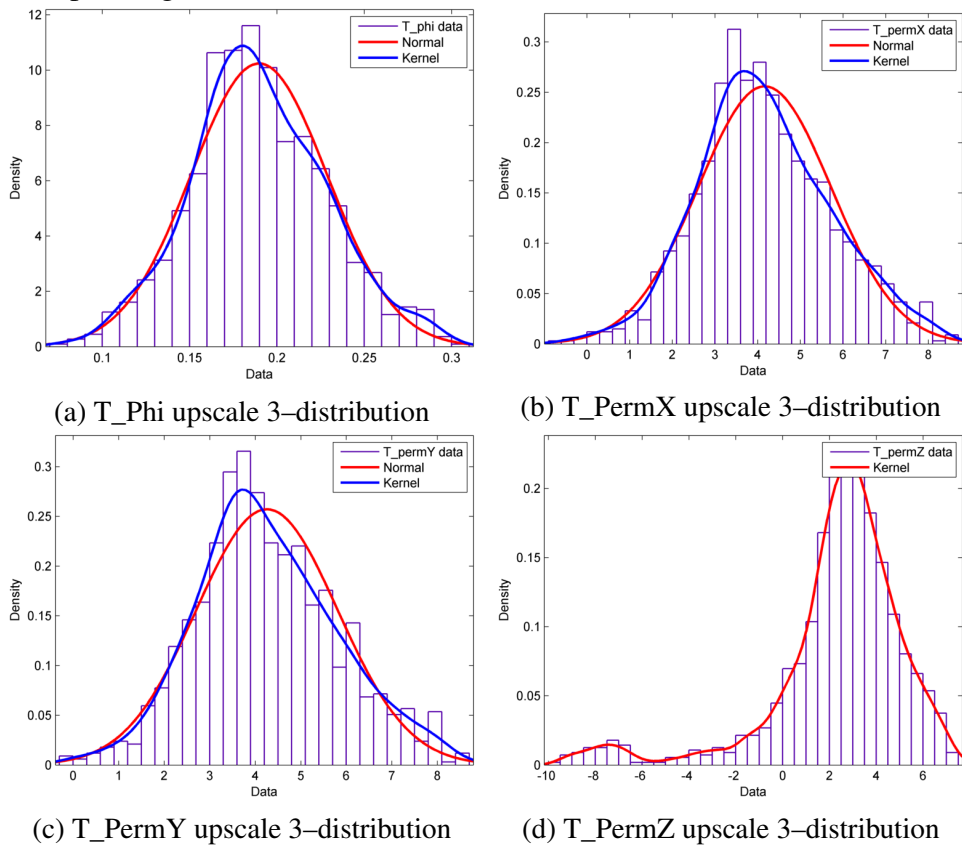


Fig. 4.50 Distribution of porosity and permeability data of the Tarbert formation after the third iteration of upscaling.

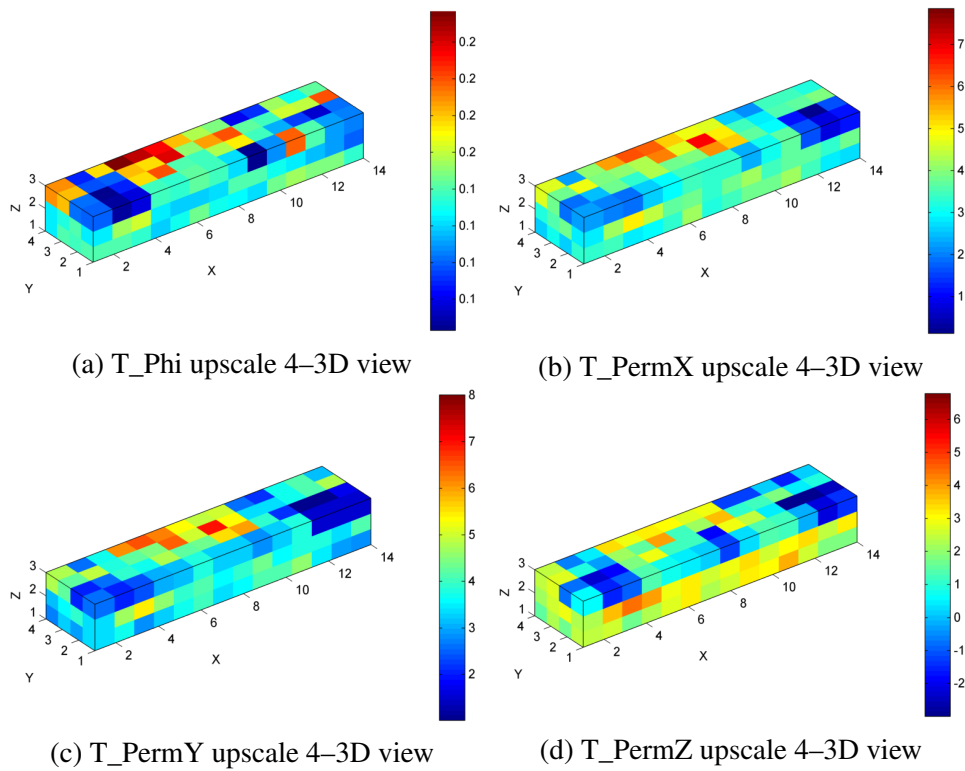


Fig. 4.51 3D images of porosity and permeability of the Tarbert formation after the fourth iteration of upscaling.

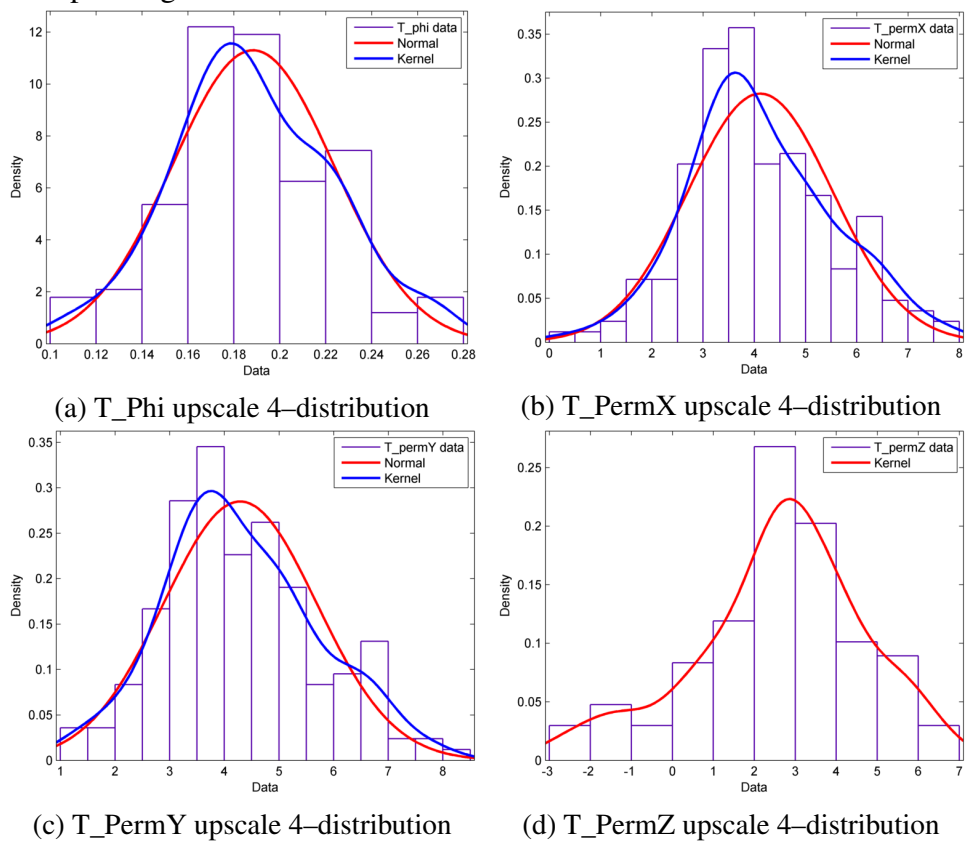


Fig. 4.52 Distribution of porosity and permeability data of the Tarbert formation after the fourth iteration of upscaling.

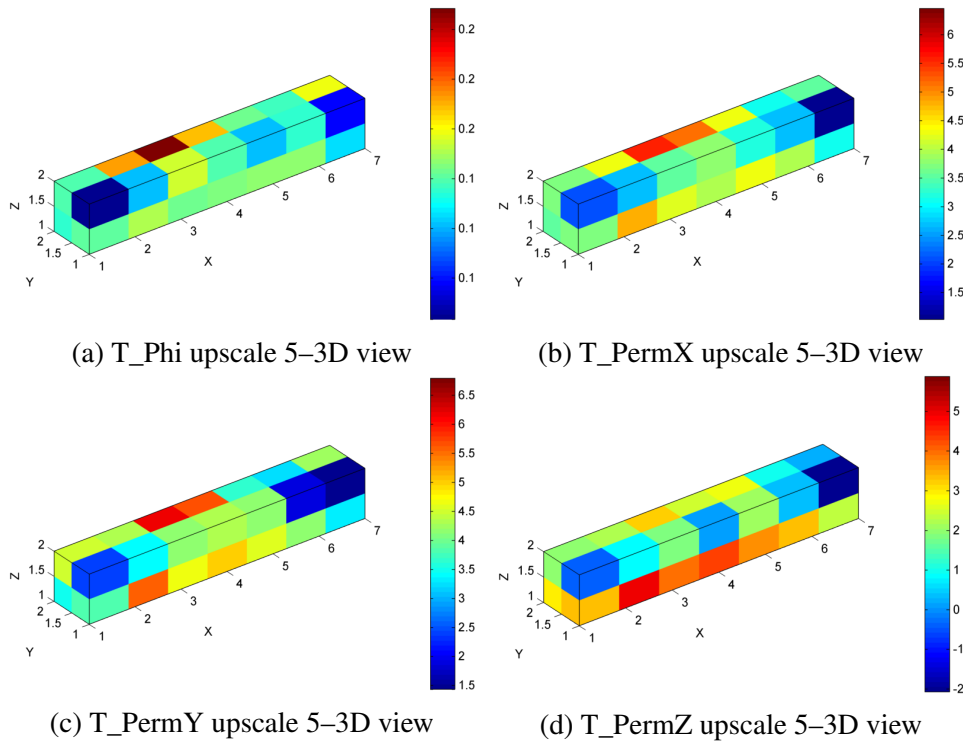


Fig. 4.53 3D images of porosity and permeability of the Tarbert formation after the fifth iteration of upscaling.

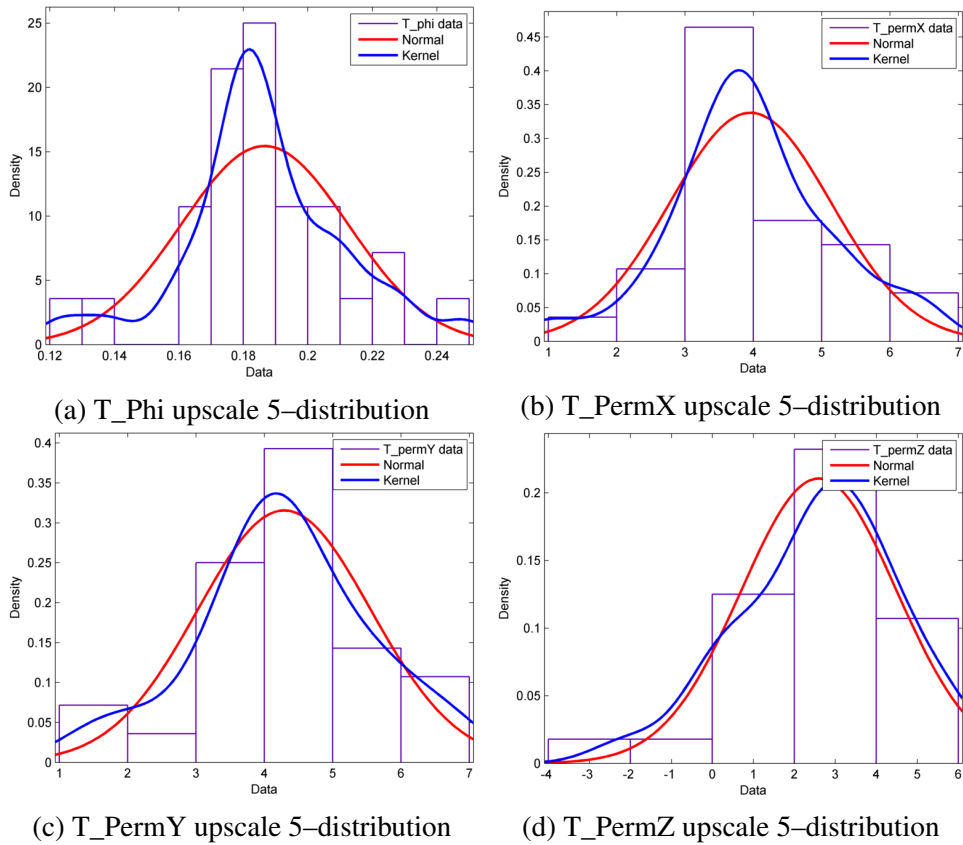


Fig. 4.54 Distribution of porosity and permeability data of the Tarbert formation after the fifth iteration of upscaling.

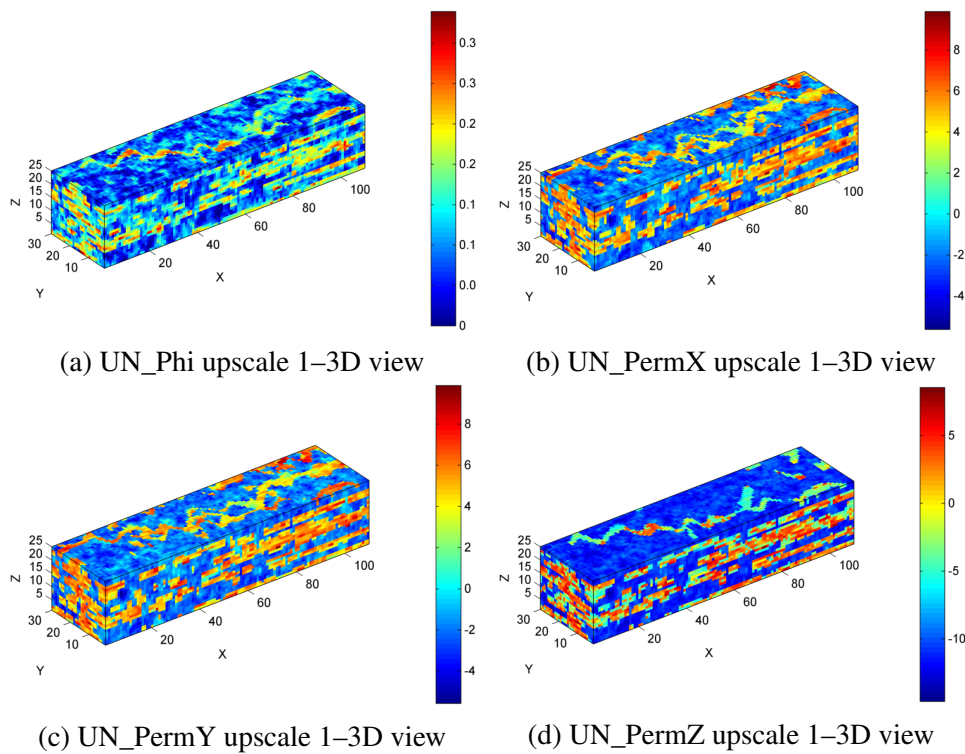


Fig. 4.55 3D images of porosity and permeability of the Upper Ness formation after the first iteration of upscaling.

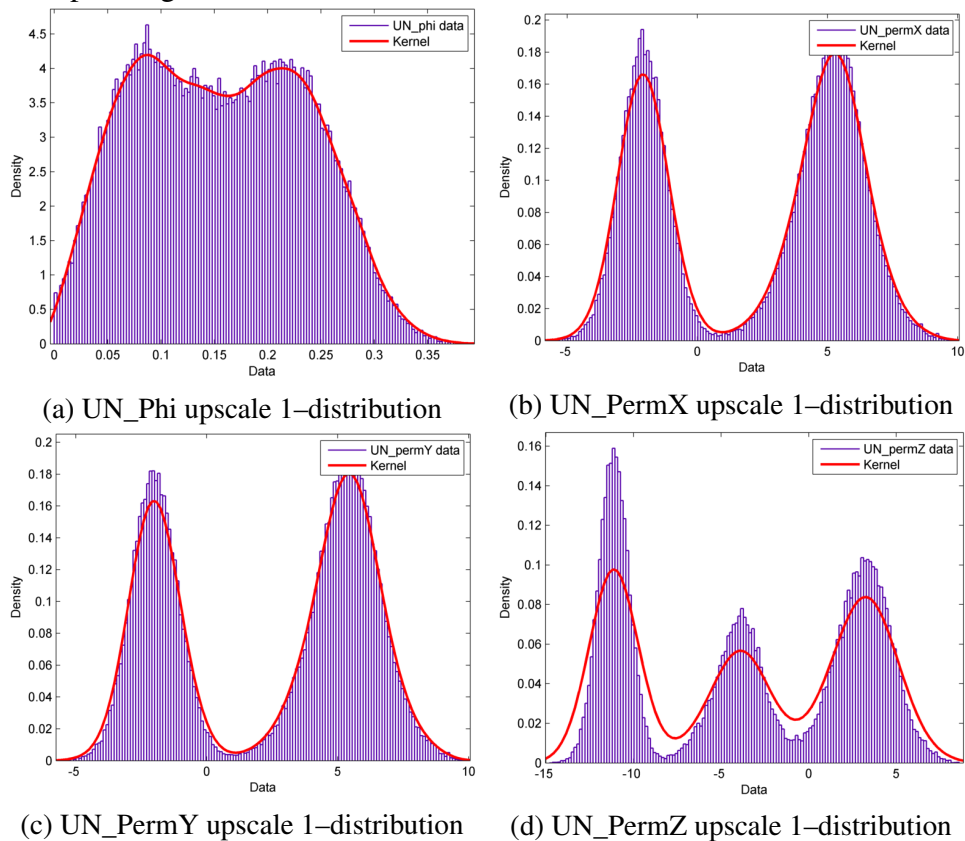


Fig. 4.56 Distribution of porosity and permeability data of the Upper Ness formation after the first iteration of upscaling.

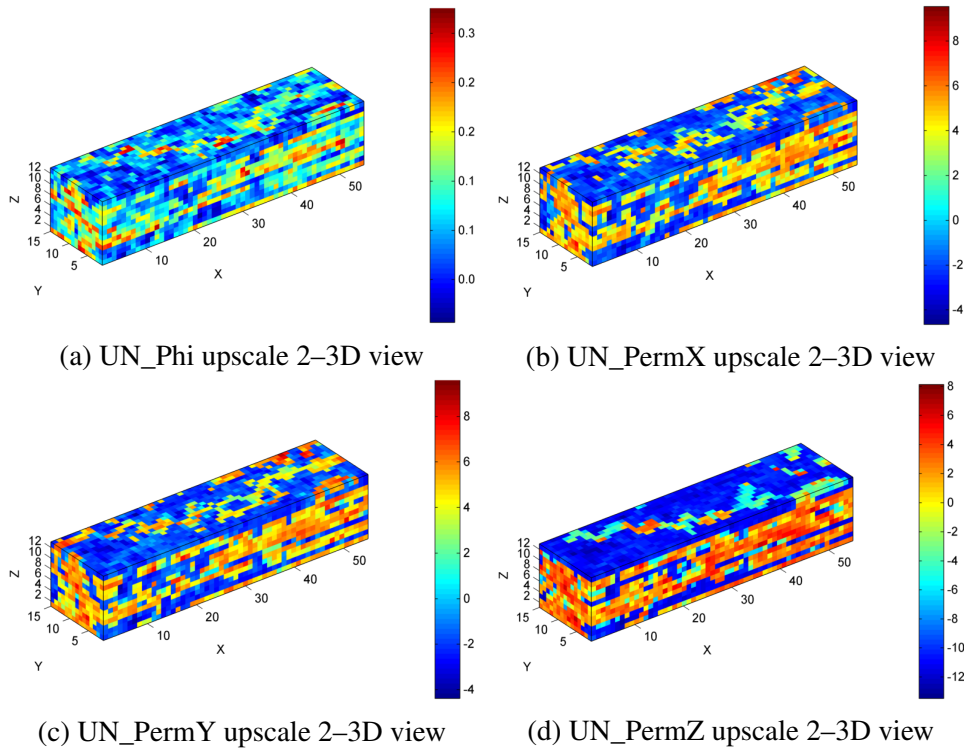


Fig. 4.57 3D images of porosity and permeability of the Upper Ness formation after the second iteration of upscaling.

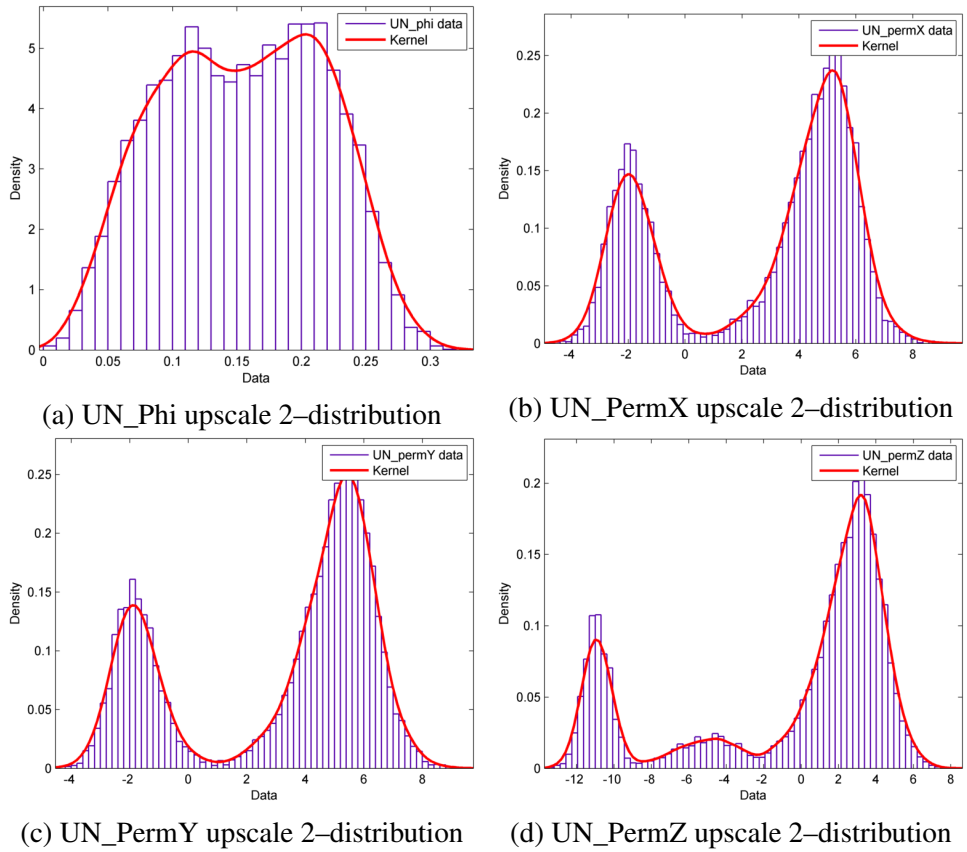


Fig. 4.58 Distribution of porosity and permeability data of the Upper Ness formation after the second iteration of upscaling.

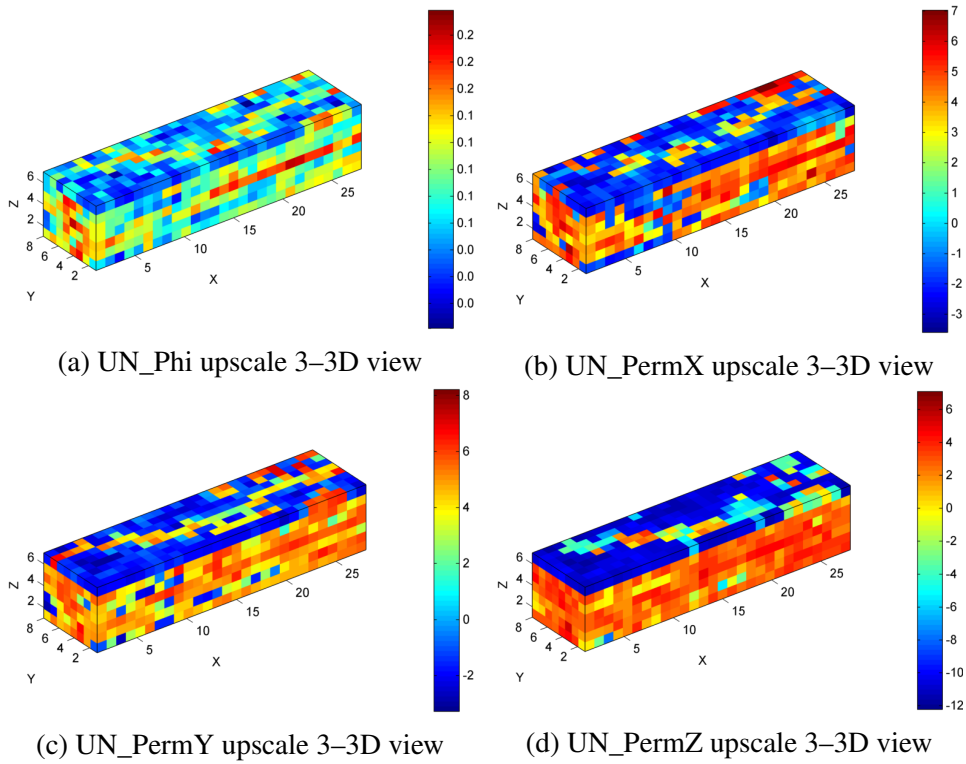


Fig. 4.59 3D images of porosity and permeability of the Upper Ness formation after the third iteration of upscaling.

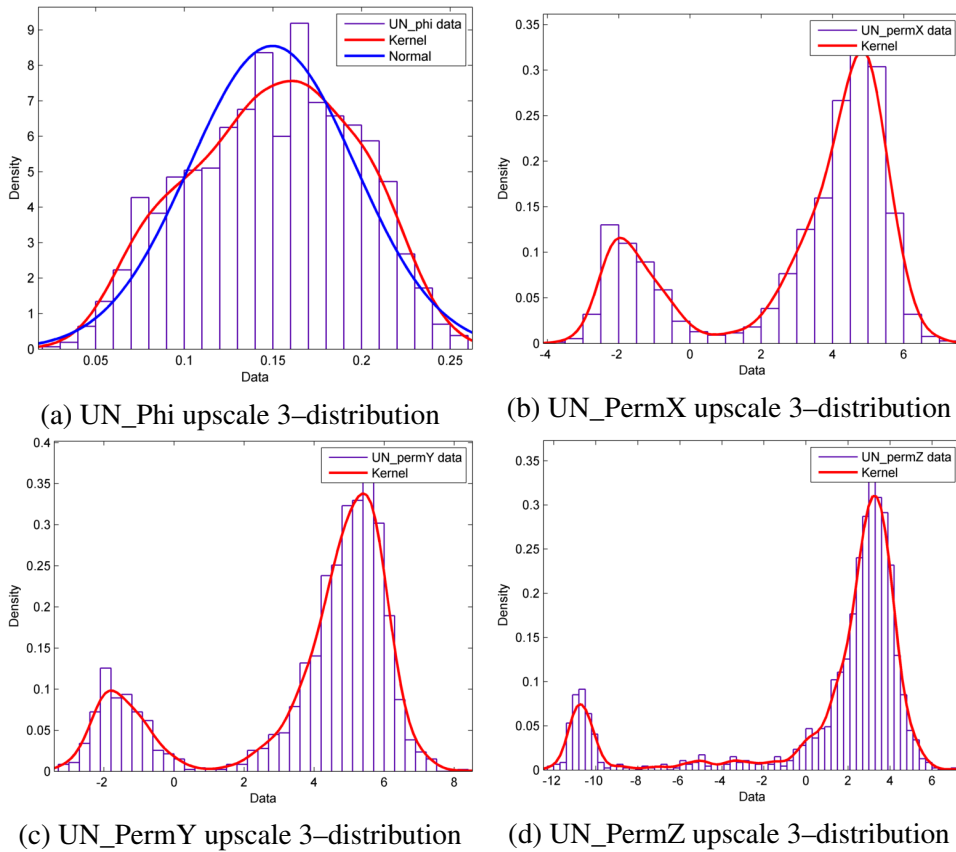


Fig. 4.60 Distribution of porosity and permeability data of the Upper Ness formation after the third iteration of upscaling.

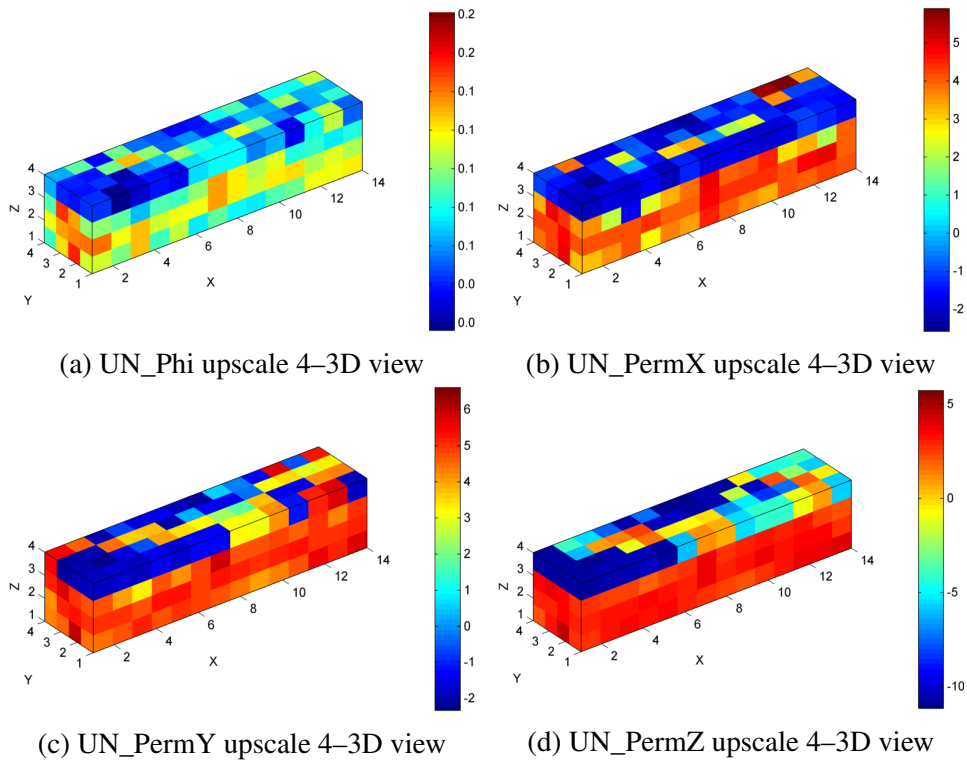


Fig. 4.61 3D images of porosity and permeability of the Upper Ness formation after the fourth iteration of upscaling.

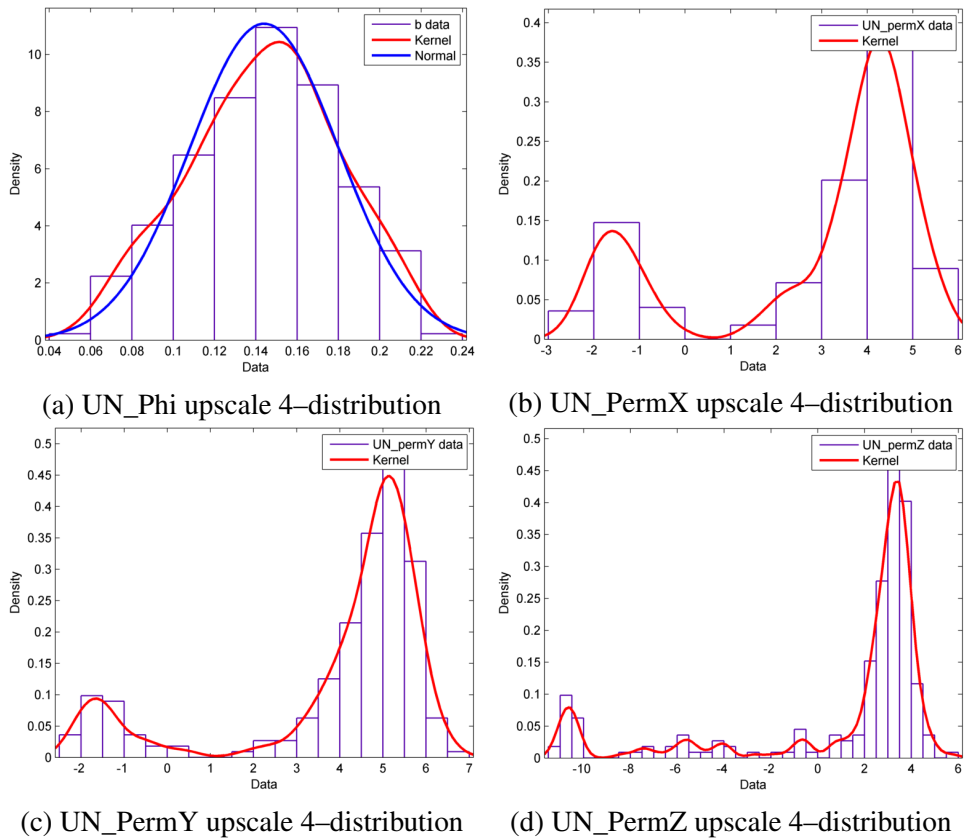


Fig. 4.62 Distribution of porosity and permeability data of the Upper Ness formation after the fourth iteration of upscaling.

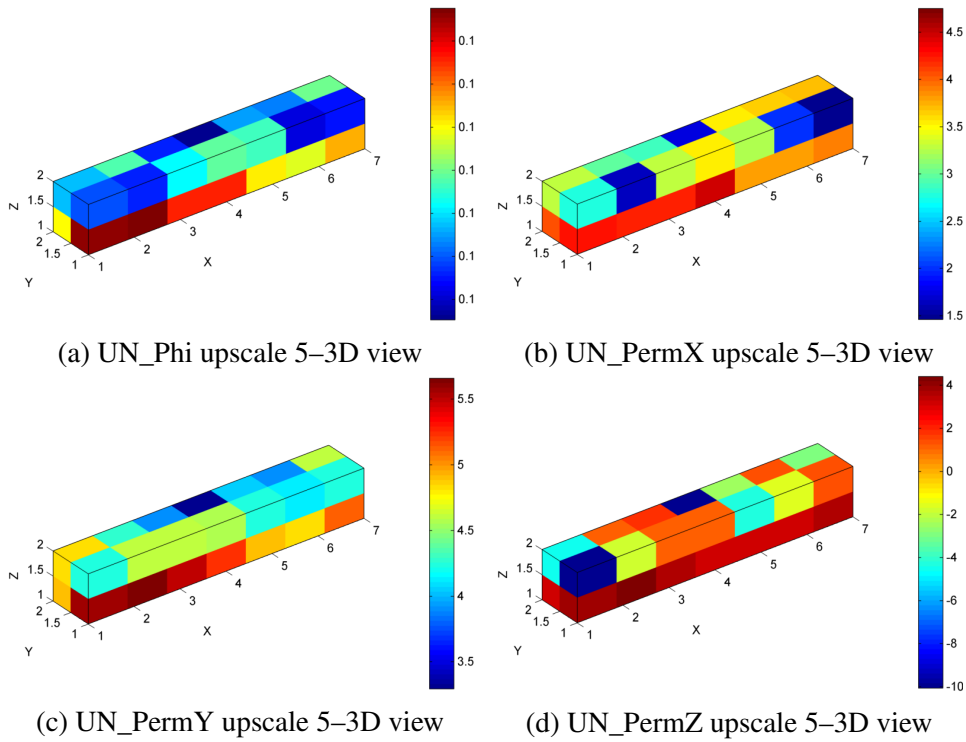


Fig. 4.63 3D images of porosity and permeability of the Upper Ness formation after the fifth iteration of upscaling.

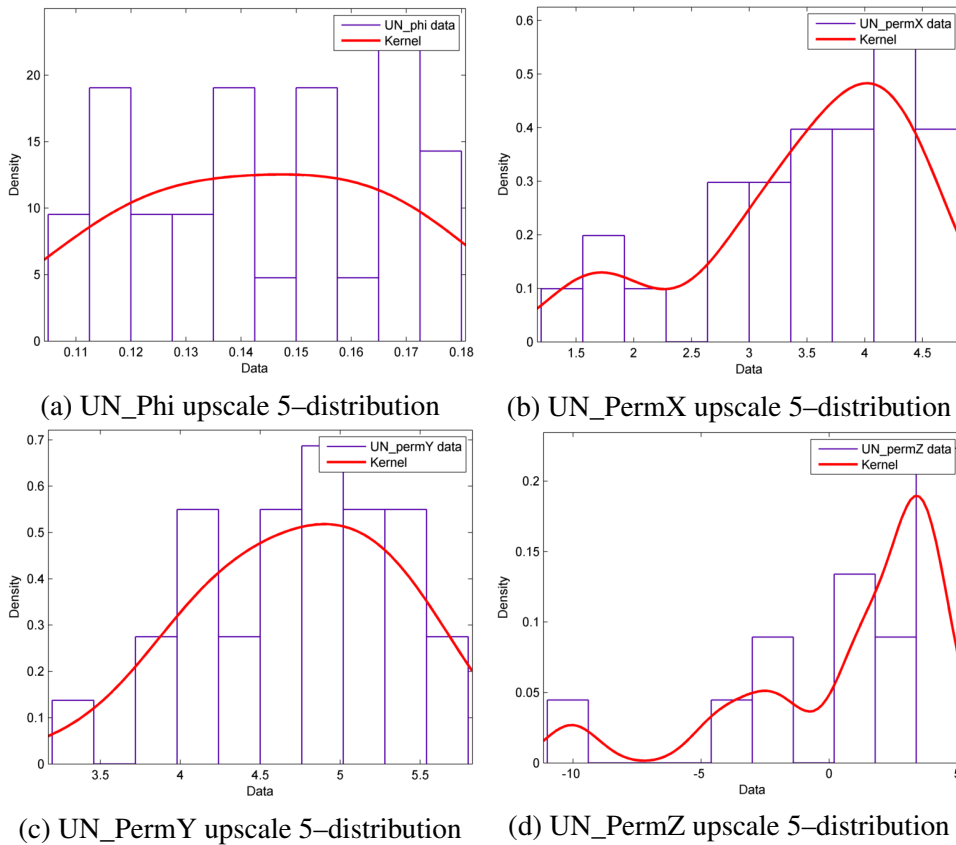


Fig. 4.64 Distribution of porosity and permeability data of the Upper Ness formation after the fifth iteration of upscaling.

Chapter 5

Conclusions & Discussion

The goal of this thesis was the implementation of geostatistical methods in order to analyse the porosity and permeability data of the 10th SPE benchmark reservoir model and derive conclusions about the behaviour and spatial correlation of these data, as well as the implications and requirements associated with geostatistical analysis.

Concerning the spatial structure and behaviour of the data, each formation displayed distinct behaviour. For the top Tarbert formation, porosity was normally, while permeability on X and Y directions was lognormally distributed. Furthermore, after applying logarithm to the data, permeability on Z direction was bimodally distributed. The lower part of the model, namely the Upper Ness formation, constituted of permeable anastomosed channels laid on a non-permeable background, which resulted in a bimodal distribution of porosity. Moreover, after applying logarithm to the data, permeability on X and Y directions followed a bimodal, while permeability on Z direction followed a trimodal distribution. It was realized that the effect of layering during sedimentation resulted in the additional distribution peak for vertical permeability, for both the Tarbert and the Upper Ness formation. Furthermore, the heterogeneity and anisotropy on both parts of the model was recognizable in all studied layers. Finally, porosity and permeability displayed a medium to strong and positive correlation for both formations.

Geostatistical analysis of both formations provided valuable results, confirming the aforementioned observations about heterogeneity and anisotropy of the model through the anisotropic variograms. It was realized by the directional, anisotropic and omnidirectional variograms that random and uncorrelated data, expressed by the nugget, were not significantly numerous. However for the 3D variograms the nugget was relatively increased, sometimes even greater than one third of the sill. Moreover, correlation range was not too great, something that can be justified by high heterogeneity. The variogram fitting procedure led mainly to the conclusion that the Tarbert formation could be mostly modelled by an

Exponential theoretical variogram, while the proper variogram model for the Upper Ness formation varied, with the most frequent being the Pentaspherical. It was also realized that the modelled range never exceeded a value of nine fine grid cells and in addition, that porosity reached the sill in smaller ranges than permeability. Last but not least, permeability along the two principal horizontal directions displayed almost identical behaviour for most conducted tests.

Several observations were made concerning the variogram analysis procedure itself. It was realized that the nugget decreased, while variogram smoothness increased, when reducing the sampling domain of the variogram. Also, increasing the maximum lag distance would cause an increase to the resulting nugget. The number of lag distance bins, into which the maximum distance was split, affected only the smoothness of the curve, but not the values. Due to anisotropy, heterogeneity and layering, increasing the thickness or height of the sampling domain would result in increasing variability and thus an increased nugget. However, specifically for the Upper Ness formation, sampling domains closer to the top displayed reduced variability relatively to the lower levels. This is explained by the structure of the anastomosed channel system. With increasing height, the channels cover increasingly less area of each layer, thus reducing relative variability. Furthermore, variance was increased along the width, compared to the length of the model. On the contrary, increasing the number of considered points along the length of the model would generally improve the total image of the variogram. Even though permeability was studied upon applying logarithm, it was realized that variogram plots were identical either with or without the logarithm.

Finally, upscaling provided interesting results as well. First and foremost, it was realized that each successive iteration significantly decreased the resolution of the model, reducing the total number of grid cells about eight times. This is a remarkable observation, since it proves the benefits of upscaling to flow simulation. Also, since the method depended on the direction of successive averaging, the final outcome could also vary, depending on the decided combination of averaging directions. A total of eight iterations were required to obtain a single equivalent value for the whole formation, while after the fifth iteration, each property was represented by a linear arrangement of blocks. Even from the first iteration, the grid resolution reduction was obvious, while after the third iteration the resemblance to the original data was minimum.

Variogram analysis turned out to be a flexible method to quantify and evaluate the spatial correlation of a formation or more generally a 3D model. As a sequel to this study, kriging could be implemented using the derived fit variogram models in order to reproduce the 3D reservoir model, followed by proper validation in order to evaluate the accuracy of the applied kriging methods, as well as the uncertainty introduced by each intermediate step. An

additional suggestion could be to use the upscaled models in flow simulations, in order to compare the results between each different degree of upscaling. These results could be also compared with the results of the 10th SPE Comparative Solution Project.

References

- Thorsten Agemar, Rüdiger Schellschmidt, and Rüdiger Schulz. Subsurface temperature distribution in Germany. *Geothermics*, 44:65–77, 2012. ISSN 03756505. doi: 10.1016/j.geothermics.2012.07.002. URL <http://dx.doi.org/10.1016/j.geothermics.2012.07.002>.
- Vasiliki D Agou. *Geostatistical Study of Precipitation on the Island of Crete*. Master dissertation, Technical University of Crete, 2016.
- José A Almeida. *Use of Geostatistical Models to Improve Reservoir Description and Flow Simulation in Heterogeneous Oil Fields*. Phd dissertation, Universidade Tecnica De Lisboa Instituto Superior Tecnico, 1999.
- Hakimeh Amanipoor. The Application of Geostatistical Methods to Prepare the 3D Petrophysical Model of Oil Reservoir. *Open Journal of Geology*, 03(01):7–18, 2013. ISSN 2161-7570. doi: 10.4236/ojg.2013.31002. URL <http://www.scirp.org/journal/PaperDownload.aspx?DOI=10.4236/ojg.2013.31002>.
- Alfredo H.-S. Ang and Wilson H. Tang. *Probability Concepts in Engineering Planning and Design, vol. 1*. Wiley, New York, 1975. ISBN 0-471-03200-X.
- Lawrence M Anovitz and David R Cole. Characterization and Analysis of Porosity and Pore Structures. *Reviews in Mineralogy and Geochemistry*, 80:61–164, 2015. ISSN 1529-6466. doi: 10.2138/rmg.2015.80.04.
- C. Ayan, Nick Colley, G. Cowan, E. Ezekwe, M. Wannell, Peter Goode, Frank Halford, Jeffrey Joseph, a. Mongini, and J. Pop. Measuring permeability anisotropy: The latest approach. *Oilfield Review*, 6(4):24–35, 1994. ISSN 09231730. URL http://199.6.139.141/media/services/resources/oilfieldreview/ors94/1094/p24_35.pdf.
- A. Azzalini and A. Capitanio. Statistical applications of the multivariate skew normal distribution. *Journal of the Royal Statistical Society: Series B (Statistical Methodology)*, 61(3):579–602, aug 1999. ISSN 1369-7412. doi: 10.1111/1467-9868.00194. URL <http://doi.wiley.com/10.1111/1467-9868.00194>.
- Tayfun Babadagli. Effective permeability estimation for 2-D fractal permeability fields. *Mathematical Geology*, 38(1):33–50, 2006. ISSN 08828121. doi: 10.1007/s11004-005-9002-z.
- Nalan Basturk, Lennart Hoogerheide, Mireille Schaap, Peter De Knijf, and Herman K. van Dijk. A Bayesian test for multimodality with applications to DNA and economic data. In *International Society for Bayesian Analysis World Meeting, ISBA 2014*, Rotterdam, 2012. Erasmus School of Economics. URL <https://bayesian.org/abstracts/8672>.

- Jacob Bear. *Dynamics of Fluids in Porous Media*. American Elsevier Publishing Company, New York, 1972. ISBN 0-486-65675-6.
- Geoff Bohling. Introduction to Geostatistics and Variogram Analysis. *Earth*, (October):1–20, 2005. ISSN <null>. doi: 10.1162/0162287054769931.
- C. F. M. Bos and PUNQ project team. Production forecasting with UNcertainty Quantification, PUNQ-2, Final Report. Technical report, Netherlands Organization for Applied Scientific Research TNO, Delft, 1999. URL <https://www.fault-analysis-group.ucd.ie/Projects/PUNQ.html>.
- Steven L. Bryant, Peter R. King, and David W. Mellor. Network model evaluation of permeability and spatial correlation in a real random sphere packing. *Transport in Porous Media*, 11(1):53–70, 1993. ISSN 01693913. doi: 10.1007/BF00614635.
- James J Butler. Hydrogeological Methods for Estimation of Spatial Variations in Hydraulic Conductivity. *Hydrogeophysics*, pages 23–58, 2005. doi: 10.1007/1-4020-3102-5.
- M.A. Christie and M.J. Blunt. Tenth SPE Comparative Solution Project: A Comparison of Upscaling Techniques. *SPE Reservoir Evaluation & Engineering*, 4(4):308–317, 2001. ISSN 1094-6470. doi: 10.2118/72469-PA.
- Diana Dell’Arciprete, Riccardo Bersezio, Fabrizio Felletti, Mauro Giudici, Alessandro Comunian, and Philippe Renard. Comparison of three geostatistical methods for hydrofacies simulation: A test on alluvial sediments. *Hydrogeology Journal*, 20(2):299–311, 2011. ISSN 14312174. doi: 10.1007/s10040-011-0808-0.
- Alexandre J. Desbarats. Numerical Estimation of Effective Permeability in Sand-Shale Formations. *Water Resources Research*, 23(2):273–286, 1987. ISSN 19447973. doi: 10.1029/WR023i002p00273.
- Yadolah Dodge. *The Oxford Dictionary of Statistical Terms*. Oxford University Press, Oxford, 2006. ISBN 9780199206131.
- Ahmed Elgammal, Ramani Duraiswami, David Harwood, and Larry S. Davis. Background and foreground modeling using nonparametric kernel density estimation for visual surveillance. *Proceedings of the IEEE*, 90(7):1151–1162, 2002. ISSN 00189219. doi: 10.1109/JPROC.2002.801448.
- C L Farmer. Upscaling: a review. *International Journal for Numerical Methods in Fluids*, 40(1-2):63–78, sep 2002. ISSN 0271-2091. doi: 10.1002/fld.267. URL <http://doi.wiley.com/10.1002/fld.267>.
- William Feller. *An Introduction to Probability Theory and Its Applications, Vol 1*. Wiley, third edition, 1968. ISBN 978-0471257080.
- Johan Galtung. *Theory and Methods of Social Research*. Allen & Unwin, London, 1968. ISBN 9780043000175.
- K. W. Glennie. *Petroleum Geology of the North Sea*. Blackwell Science Ltd, Oxford, UK, jun 1998. ISBN 9781444313413. doi: 10.1002/9781444313413. URL <http://doi.wiley.com/10.1002/9781444313413>.

- Emmanuel Gringarten and Clayton V Deutsch. Methodology for Variogram Interpretation and Modeling for Improved Reservoir Characterization. *Centre for Computational Geostatistics*, pages 1–33, 1999. doi: 10.2523/56654-MS. URL <http://www.spe.org/elibrary/servlet/spepreview?id=00056654>.
- Be Hansen. Lecture notes on nonparametrics. *Lecture notes*, 2009. URL <http://www.ssc.wisc.edu/~bhansen/718/NonParametrics1.pdf>.
- W. K. Hastings. Monte Carlo sampling methods using Markov chains and their applications. *Biometrika*, 57(1):97–109, 1970. ISSN 0006-3444. doi: 10.1093/biomet/57.1.97. URL <http://biomet.oxfordjournals.org/cgi/doi/10.1093/biomet/57.1.97>.
- Michiel Hazewinkel. *Encyclopaedia of Mathematics*. Springer, Netherlands, 1 edition, 1994. ISBN 978-1-55608-010-4.
- Dionissios T. Hristopulos. Dionissios T. Hristopulos, 2011. URL <http://www.mred.tuc.gr/home/hristopulos/dionisi.htm>.
- M. A. Ioannidis, M. J. Kwiecien, and I. Chatzis. Statistical analysis of the porous microstructure as a method for estimating reservoir permeability. *Journal of Petroleum Science and Engineering*, 16(4):251–261, 1996. ISSN 09204105. doi: 10.1016/S0920-4105(96)00044-7.
- Edward H. Isaaks and R. Mohan Srivastava. *An Introduction to Applied Geostatistics*. Oxford University Press, New York, 1989. ISBN 978-0195050134.
- J W Jennings, S C Ruppel, and W B Ward. Geostatistical Analysis of Permeability Data and Modeling of Fluid-Flow Effects in Carbonate Outcrops. *SPE Reservoir Evaluation & Engineering*, 3(December 1998):293–303, 2000. ISSN 1094-6470. doi: 10.2118/65370-PA.
- Mohammad Reza Kamali, Azadeh Omidvar, and Ezatallah Kazemzadeh. 3D Geostatistical Modeling and Uncertainty Analysis in a Carbonate Reservoir, SW Iran. *Journal of Geological Research*, 2013:1–7, 2013. ISSN 1687-8833. doi: 10.1155/2013/687947. URL <http://www.hindawi.com/journals/jgr/2013/687947/>.
- J. F. Kenney and E. S. Keeping. *Mathematics of Statistics*, volume Part 1. Van Norstrand Company, New Jersey, third edition, 1962. URL <http://books.google.fr/books?id=UdILAAAAMAAJ>.
- Larry W. Lake, Herbert B. Carroll, Thomas C. Wesson, and Tex.) International Reservoir Characterization Technical Conference (2nd : 1989 : Dallas. *Reservoir characterization II*. Academic Press, 1991. ISBN 9780124340664.
- Alberto Leon-Garcia. *Probability, Statistics, and Random Processes for Electrical Engineering*. Upper Saddle River, third edition, 2008. ISBN 9780131471221.
- M.C. Leverett. Capillary Behavior in Porous Solids. *Transactions of the AIME*, 142(01): 152–169, 1941. ISSN 0081-1696. doi: 10.2118/941152-G. URL <http://www.onepetro.org/doi/10.2118/941152-G>.

- O. Lia, H. Omre, H. Tjelmeland, L. Holden, and T. Egeland. Uncertainties in Reservoir Production Forecasts. *AAPG Bulletin*, 1997.
- A. C. Liakopoulos. Darcy's Coefficient of Permeability As Symmetric Tensor of Second Rank. *International Association of Scientific Hydrology. Bulletin*, 10(3):41–48, 1965. ISSN 0020-6024. doi: 10.1080/02626666509493405. URL <http://www.tandfonline.com/doi/abs/10.1080/02626666509493405>.
- Eric Ludlam. Sliceomatic, 2001. URL https://www.mathworks.com/matlabcentral/fileexchange/764-sliceomatic,MATLAB_Central_File_Exchange.
- Aidan Lyon. Why are normal distributions normal? *British Journal for the Philosophy of Science*, 65(3):621–649, 2014. ISSN 14643537. doi: 10.1093/bjps/axs046.
- Jianjun Ma. Review of permeability evolution model for fractured porous media. *Journal of Rock Mechanics and Geotechnical Engineering*, 7(3):351–357, 2015. ISSN 16747755. doi: 10.1016/j.jrmge.2014.12.003.
- Lonnie Magee. R 2 Measures Based on Wald and Likelihood Ratio Joint Significance Tests. *The American Statistician*, 44(3):250, aug 1990. ISSN 00031305. doi: 10.2307/2685352. URL <http://www.jstor.org/stable/2685352?origin=crossref>.
- K. Mahmud, G. Mariethoz, A. Baker, and A. Sharma. Integrating multiple scales of hydraulic conductivity measurements in training image-based stochastic models. *Water Resources Research*, 51(1):465–480, 2015. ISSN 19447973. doi: 10.1002/2014WR016150. URL <http://doi.wiley.com/10.1002/2014WR016150>.
- Hernán a. Makse, Shlomo Havlin, Plamen Ch. Ivanov, Peter R. King, Sona Prakash, and H. Eugene Stanley. Pattern formation in sedimentary rocks: Connectivity, permeability, and spatial correlations. *Physica A: Statistical Mechanics and its Applications*, 233(3-4): 587–605, 1996. ISSN 03784371. doi: 10.1016/S0378-4371(96)00246-4.
- Gregoire Mariethoz, Philippe Renard, and Julien Straubhaar. The Direct Sampling method to perform multiple-point geostatistical simulations. *Water Resources Research*, 46(11): 1–14, 2010. ISSN 00431397. doi: 10.1029/2008WR007621.
- M. Masihi, P. A. Gago, and P. R. King. Estimation of the Effective Permeability of Heterogeneous Porous Media by Using Percolation Concepts. *Transport in Porous Media*, 114(1):169–199, 2016. ISSN 15731634. doi: 10.1007/s11242-016-0732-9. URL ["http://dx.doi.org/10.1007/s11242-016-0732-9](http://dx.doi.org/10.1007/s11242-016-0732-9).
- Carl McDaniel and Roger Gates. *Marketing Research*. Wiley, ninth edition, 2012. ISBN 978-1118112717.
- Clyde H. Moore and William J. Wade. *Carbonate Reservoirs Porosity and Diagenesis in a Sequence Stratigraphic Framework*. Elsevier, second edition, 2013. ISBN 978-0-444-53831-4. URL <https://www.elsevier.com/books/carbonate-reservoirs/moore/978-0-444-53831-4#>.
- Benoit Noetinger, Andre Haas, and Reservoir Helios Group. Permeability Averaging for Well Tests in 3D Stochastic Reservoir Models. pages 919–925, 1996. doi: <http://dx.doi.org/10.2118/36653-MS>. URL <https://www.onepetro.org/conference-paper/SPE-36653-MS>.

- Ricardo A. Olea. A Practical Primer on Geostatistics. *U.S. Geological Survey*, page 346, 2009. ISSN 2009–1103. URL <http://pubs.usgs.gov/of/2009/1103/>.
- Dean S. Oliver. The Averaging Process in Permeability Estimation From Well-Test Data. *SPE Form. Eval.*, 5(3):319–324, 1990. ISSN 0885-923X. doi: 10.2118/19845-PA.
- Evangelos K. Paleologos, Shlomo P. Neuman, and Daniel Tartakovsky. Effective Hydraulic Conductivity of Bounded, Strongly Heterogeneous Porous Media. *Water Resources Research*, 32(5):1333–1341, may 1996. ISSN 00431397. doi: 10.1029/95WR02712. URL <http://doi.wiley.com/10.1029/95WR02712>.
- Emanuel Parzen. On Estimation of a Probability Density Function and Mode. *The Annals of Mathematical Statistics*, 33(3):1065–1076, 1962.
- PetroWiki. Comparison of permeability estimation models, 2015a. URL http://petrowiki.org/Comparison_of_permeability_estimation_models.
- PetroWiki. Single phase permeability, 2015b. URL http://petrowiki.org/Single_phase_permeability.
- PetroWiki. Geostatistical conditional simulation, 2016a. URL http://petrowiki.org/Geostatistical_conditional_simulation.
- PetroWiki. Geostatistics, 2016b. URL <http://petrowiki.org/Geostatistics>.
- PetroWiki. Relative permeability models, 2016c. URL http://petrowiki.org/Relative_permeability_models.
- Michael J. Pyrcz and Clayton V. Deutsch. *Geostatistical Reservoir Modeling*. Oxford University press, Oxford [etc.], second edition, 2014. ISBN 9780199731442.
- Alejandro Quintela-Del-Rio and Graciela Estevez-Perez. Nonparametric Kernel Distribution Function Estimation with kerdieft : An R Package for Bandwidth Choice and Applications. *Journal of Statistical Software*, 50(8), 2012. ISSN 1548-7660. doi: <http://dx.doi.org/10.18637/jss.v050.i08>.
- P. Renard, G. Le Loc’h, E. Ledoux, and G. De Marsily. Simplified Renormalization: A New Quick Upscaling Technique. pages 89–100. 1997. doi: 10.1007/978-94-017-1675-8_8. URL http://link.springer.com/10.1007/978-94-017-1675-8_8.
- Ph. Renard and G. de Marsily. Calculating equivalent permeability: a review. *Advances in Water Resources*, 20(5-6):253–278, 1997. ISSN 03091708. doi: 10.1016/S0309-1708(96)00050-4. URL <http://linkinghub.elsevier.com/retrieve/pii/S0309170896000504>.
- Deborah J. Rumsey. *Statistics For Dummies*. Wiley, Indianapolis, second edition, 2016. ISBN 978-1-119-29352-1.
- Mohsen Saemi, Morteza Ahmadi, and Ali Yazdian Varjani. Design of neural networks using genetic algorithm for the permeability estimation of the reservoir. *Journal of Petroleum Science and Engineering*, 59(1-2):97–105, 2007. ISSN 09204105. doi: 10.1016/j.petrol.2007.03.007.

- George Saratsis. *Coupled Geostatistical Analysis with Tunelling Modelling (in Greek)*. Master dissertation, Technical University of Crete, 2004.
- Wolfgang Schwanghart. Experimental (Semi-) Variogram, 2008. URL <https://www.mathworks.com/matlabcentral/fileexchange/20355-experimental--semi---variogram>, MATLAB_Central_File_Exchange.
- Wolfgang Schwanghart. Variogramfit, 2009. URL <https://www.mathworks.com/matlabcentral/fileexchange/25948-variogramfit>, MATLAB_Central_File_Exchange.
- B. W. Silverman. *Density estimation for statistics and data analysis*. Chapman and Hall, London, 1986. ISBN 0412246201. doi: 10.2307/2347507. URL http://books.google.com/books?hl=en&lr=&id=e-xsrjsL7WkC&oi=fnd&pg=PR9&dq=Density+Estimation+for+Statistics+and+Data+Analysis&ots=ivSomp7D_q&sig=XfZFIEyzmSO4nm54dgq22EiW9iA.
- SPE. SPE Comparative Solution Project-description of model 2, 2000. URL <http://www.spe.org/web/csp//datasets/set02.htm>.
- Staios. Staios, 2000. URL <http://www.staios.com/Staios/>.
- James J. P. Stewart. Optimization of parameters for semiempirical methods II. Applications. *Journal of Computational Chemistry*, 10(2):221–264, mar 1989. ISSN 0192-8651. doi: 10.1002/jcc.540100209. URL <http://doi.wiley.com/10.1002/jcc.540100209>.
- M. L. Sweet, C. J. Blewden, A. M. Carter, and C. A. Mills. Modeling Heterogeneity in a Low-Permeability Gas Reservoir Using Geostatistical Techniques, Hyde Field, Southern North Sea. *AAPG Bulletin*, 80(11):1719–1735, 1996. ISSN 01491423. doi: 10.1306/64EDA14A-1724-11D7-8645000102C1865D.
- Anita Torabi, Haakon Fossen, and Behzad Alaei. Application of spatial correlation functions in permeability estimation of deformation bands in porous rocks. *Journal of Geophysical Research: Solid Earth*, 113(8):1–10, 2008. ISSN 21699356. doi: 10.1029/2007JB005455.
- Erik Vanmarcke. *Random Fields: Analysis and Synthesis*. World Scientific Publishing Company, Singapore, 2010. ISBN 978-9812563538.
- J Vollset and a G Dore. A revised Triassic and Jurassic lithostratigraphic nomenclature for the Norwegian North Sea, 1984.
- Christian Walck. Hand-book on Statistical Distributions for experimentalists. *Hand-book on Statistical Distributions for experimentalists*, (September):26–35, 2007. ISSN <null>. URL <http://www.stat.rice.edu/~dobelman/textfiles/DistributionsHandbook.pdf>.
- Wikipedia. Porosity, 2016. URL <https://en.wikipedia.org/wiki/Porosity>.
- George Xiroudakis. *Geotechnical Characterization of Rock Mass Based on Geostatistical Analysis of Data from Borehole Samples and Tunnel Boring Machines (TBM)(in Greek)*. Master dissertation, Technical University of Crete, 2007.

- Ling Xu, Timothy Hanson, Edward J. Bedrick, and Carla Restrepo. Hypothesis Tests on Mixture Model Components with Applications in Ecology and Agriculture. *Journal of Agricultural, Biological, and Environmental Statistics*, 15(3):308–326, sep 2010. ISSN 1085-7117. doi: 10.1007/s13253-010-0020-z. URL <http://link.springer.com/10.1007/s13253-010-0020-z>.
- Jeffrey Yarus and Richard Chambers. Practical Geostatistics - An Armchair Overview for Petroleum Reservoir Engineers. *Journal of Petroleum Technology*, 58(11):78–87, 2006. ISSN 0149-2136. doi: 10.2118/103357-MS.
- Feng Zhu. A nonparametric analysis of the shape dynamics of the US personal income distribution: 1962-2000. (184), 2005. URL <http://papers.ssrn.com/abstract=845708>.

Appendix A

Calculation Algorithms

The utilized algorithms for statistical analysis and construction of the different variograms, as well as the algorithm for upscaling are presented in the following sections. All algorithms were developed and run in *Matlab* environment.

Loading the Data

The datasets obtained from the 10th SPE Comparative Solution Project website (SPE, 2000) contain porosity data in the form a 187000-by-6 array and permeability data in the form a 561000-by-6 array. The latter array contains the permeability datasets for all three directions, thus they have to be split up first. The procedure required to load the data is the following:

```
1 load('spe_perm.dat'); %load permeability dataset
2 load('spe_phi.dat'); %load porosity dataset
3
4 %Separate the 3 datasets of permeability
5 permX=spe_perm(1:187000,:);
6 permY=spe_perm(187001:374000,:);
7 permZ=spe_perm(374001:end,:);
8
9 %Reshape to the model's dimensions(60x220x85) and flip the vertical
10 %direction so that Tarbert formation goes on top.
11 permX=reshape(permX',60,220,85); %Reshape to the model's dimensions
12 permX=flipdim(permX,3); %flip vertical direction
13 permY=reshape(permY',60,220,85);
14 permY=flipdim(permY,3);
15 permZ=reshape(permZ',60,220,85);
16 permZ=flipdim(permZ,3);
```

```

17 phi=reshape(spe_phi',60,220,85);
18 phi=flipdim(phi,3);
19
20 %Separate the Tarbert and Upper Ness formations in different datasets.
21 T_phi=phi(:,:,51:85);
22 T_permX=permX(:,:,51:85);
23 T_permY=permY(:,:,51:85);
24 T_permZ=permZ(:,:,51:85);
25 UN_phi=phi(:,:,1:50);
26 UN_permX=permX(:,:,1:50);
27 UN_permY=permY(:,:,1:50);
28 UN_permZ=permZ(:,:,1:50);

```

Visualisation & Statistical Analysis

The visualisation of the data is achieved using the program *Slice-o-Matic* (Ludlam, 2001). Subsequently, in order to carry out the statistical analysis, the required moments were calculated using the following commands:

```

1 a=load(T_phi); %load the studied dataset
2
3 %Visualisation of the data
4 sliceomatic(a) %for porosity
5 sliceomatic(log(a)) %for permeability
6
7 %Statistical Analysis
8 b=reshape(a,1,[]); %reshape to vector
9 log_val=log(b); %apply logarithm to permeability (for distribution fitting)
10 MIN=min(b)
11 MAX=max(b)
12 Mean=mean(b)
13 Median=median(b)
14 Mode=mode(b)
15 Variance=var(b)
16 Skew=skewness(b)
17 Kurt=kurtosis(b)
18 Size=size(b)
19 Num_elements=numel(b)
20 dfittool %launch Matlab's Distribution Fitting Tool
21 sliceomatic(a) %visualise porosity data
22 sliceomatic(log(a)) %visualise permeability data

```

Directional Variogram

In order to derive and combine the numerous directional variograms into the so called *variogram cloud*, as well as the mean variograms, the following code was used in combination with the program *Experimental (Semi-) Variogram* (Schwanghart, 2008):

```

1 function [val,dist,num,meanval]=variogram_cloud(A,direction,m,c,r);
2 % This script will acquire (c*r) core samples on a set direction and
3 % create a variogram cloud.
4 %
5 %Define the initial prerequisites
6 %   A: the dataset under study
7 %   direction: 'X'(width) or 'Y'(length) or 'Z'(elevation)
8 %   m: the maximum number of grid cells in the required direction
9 %   c: number of vertical samples (columns)
10 %   r: number of horizontal samples (rows)
11 %
12 x=(1:1:m)'; %Define the distance vector (variable x of variogram.m script)
13 % Obtain a core sample and reshape into column vector (variable
14 % y of variogram.m script). (i-1) & (j-1) change the
15 % matrix rows and columns.
16 for j=1:r
17   for i=1:c
18     if strcmp(direction,'Y')
19       y=reshape(A(3+round((size(A,1)-3)/c)*(i-1),:,3+...
20         round((size(A,3)-3)/r)*(j-1)),[],1);
21     elseif strcmp(direction,'X')
22       y=reshape(A(:,3+round((size(A,2)-3)/c)*(i-1),3+...
23         round((size(A,3)-3)/r)*(j-1)),[],1);
24     elseif strcmp(direction,'Z')
25       y=reshape(A(3+round((size(A,1)-3)/c)*(i-1),3+...
26         round((size(A,2)-3)/r)*(j-1),:),[],1);
27     end
28     variogram(x,y); %Experimental (Semi-) Variogram program
29     val(1:20,(j-1)*c+i)=ans.val; %Store the val-values
30     dist(1:20,(j-1)*c+i)=ans.distance; %Store the distance- values
31   end
32 end
33 %Replace all the Not-a-Numbers (NaN)
34 NaNs=find(isnan(val(:,1))); %Find and exclude NaNs from distance vector
35 for i=1:size(NaN,1)
36   val(NaN(i),:)=(val(NaN(i)-1,:)+val(NaN(i)+1,:))/2;

```

```

37 end
38 %Store the mean values
39 for i=1:size(dist,1);
40     meanval(i)=mean(val(i,:));
41 end
42 %Plot the Variogram Cloud
43 for i=1:100
44     plot(dist(:,i),val(:,i),'g')
45     hold on;
46     title('Normal Vertical Axis')
47     hold on;
48     plot(dist(:,1),meanval,'k','LineWidth',1.2) %Plot mean variogram
49     xlabel('h');
50     ylabel('\gamma (h)');
51 end
52 end

```

3D variogram

Although the 3D variogram was calculated by the program *Experimental (Semi-) Variogram* (Schwanghart, 2008), data had to be prepared in order to meet the required input formulation as such:

```

1 function [coord,values,corecrd,coreval]=td_variogram(A,elements,nc)
2 % Prepare the data for the 3D variogram
3 %   A=the array under study
4 %   elements='all' for all elements, 'cores' for a number of sample cores
5 %   nc=number of cores
6 %
7 %Assign individual point coordinates to each line of the matrix (x y z)
8 coord=zeros(numel(A),3);
9 n=0;
10 for i=1:size(A,1);
11     for j=1:size(A,2);
12         for k=1:size(A,3);
13             n=n+1; %Go to the next line for each iteration
14             coord(n,:)=[i j k];
15         end
16     end
17 end
18 %Assign the corresponding attribute values to a column vector

```

```

19 values=zeros(numel(A),1);
20 for i=1:numel(A)
21     values(i)=A(coord(i,1),coord(i,2),coord(i,3));
22 end
23 %Decide whether to use all the elements or only limited core samples
24 if strcmp(elements, 'cores')
25     a=size(coord,1)/size(A,3);
26     b=round(a/(nc+0.1*nc)); %Divide the matrix into groups of size(A,3).
27     %Add a 10% margin so the code will not crash.
28     corecrd=zeros(nc*size(A,3),3);
29     coreval=zeros(nc*size(A,3),1);
30     for i=1:nc
31         for j=1:size(A,3)
32             %Core coordinates
33             corecrd((i-1)*size(A,3)+j,:)=coord(b*size(A,3)*i+j,:);
34         end
35     end
36     for i=1:size(corecrd,1)
37         %Corresponding core values
38         coreval(i)=A(corecrd(i,1),corecrd(i,2),corecrd(i,3));
39     end
40 elseif strcmp(elements, 'all')
41 end

```

Variogram Fitting

The variogram fitting, following the 3D variogram construction, was executed using the program *Variogramfit* (Schwanghart, 2009). The required nugget, sill, range and Coefficient of Determination were obtained in the following manner:

```

1 %Only a specific subvolume of the formation property is used.
2 [coord, values]=td_variogram(T_phi(6:25,21:90,11:30), 'all', 100);
3
4 %Experimental (Semi-) Variogram program
5 variogram(coord, values, 'plotit', false, 'maxdist', 28, 'subsample', 2000);
6 h=ans.distance; % store lag distances
7 gammaexp=ans.val; % store gamma values
8
9 %Store range(a), sill(c), nugget(n) and output structure
10 %array(S) resulting from the fitting.
11 [a c n S]=variogramfit(h, gammaexp, [], [], [], 'solver', 'fminsearchbnd', ...

```

```

12     'nugget',0,'plotit',true,'model','bilinear');
13 Rsq=S.Rs; %Coefficient of Determination - R^2

```

Upscaling

In order to implement the upscaling procedure described in Chapter 2, the following code was used:

```

1 function [UP,lower_bound,upper_bound]=upscaling(UP,flow_dir,iterations)
2 % Simplified Renormalization (in 3D) according to Renard et al. (1997).
3 % A: the studied model (3D array)
4 % flow_dir (flow direction): 'X'-width, 'Y'-length, 'Z'-height,
5 %                               'poro' for POROSITY(only arithmetic averages)
6 % iterations: number of iterations. Ultimately one single value is obtained,
7 %               equal to the equivalent effective permeability.
8 % First average for X, then for Y, then for Z and iterate.
9 % IMPORTANT: Permeability data is used without logarithm.
10 %
11 %Define Wiener bounds (only for equivalent values)
12 lower_bound=harmmean(reshape(UP,[],1));
13 upper_bound=mean(reshape(UP,[],1));
14 % Comence upscaling
15 for n=1:iterations;
16     % average along X axis (width)
17     U1=zeros(ceil(size(UP,1)/2),size(UP,2)/2,size(UP,3)/2); %preallocate memory
18     for k=1:size(UP,3);
19         for j=1:size(UP,2);
20             for i=1:ceil(size(UP,1)/2);
21                 if i==ceil(size(UP,1)/2); %i is the last one
22                     if mod(size(UP,1),2)==1 %size is odd
23                         U1(i,j,k)=UP(2*i-1,j,k);
24                     else %size is even
25                         if strcmp(flow_dir, 'X')
26                             U1(i,j,k)=harmmean([UP(2*i-1,j,k) UP(2*i,j,k)]);
27                         else
28                             U1(i,j,k)=mean([UP(2*i-1,j,k) UP(2*i,j,k)]);
29                         end
30                     end
31                 else %i is not the last one
32                     if strcmp(flow_dir, 'X')
33                         U1(i,j,k)=harmmean([UP(2*i-1,j,k) UP(2*i,j,k)]);

```

```

34         else
35             U1(i,j,k)=mean([UP(2*i-1,j,k) UP(2*i,j,k)]);
36         end
37     end
38 end
39 end
40 end
41 % average along Y axis (length)
42 U2=zeros(size(UP,1)/2,ceil(size(UP,2)/2),size(UP,3)/2);
43 for k=1:size(UP,3);
44     for j=1:ceil(size(UP,2)/2);
45         for i=1:size(U1,1);
46             if j==ceil(size(UP,2)/2); %j is the last one
47                 if mod(size(UP,2),2)==1 %size is odd
48                     U2(i,j,k)=U1(i,2*j-1,k);
49                 else %size is even
50                     if strcmp(flow_dir, 'Y')
51                         U2(i,j,k)=harmmean([U1(i,2*j-1,k) U1(i,2*j,k)]);
52                     else
53                         U2(i,j,k)=mean([U1(i,2*j-1,k) U1(i,2*j,k)]);
54                     end
55                 end
56             else %j is not the last one
57                 if strcmp(flow_dir, 'Y')
58                     U2(i,j,k)=harmmean([U1(i,2*j-1,k) U1(i,2*j,k)]);
59                 else
60                     U2(i,j,k)=mean([U1(i,2*j-1,k) U1(i,2*j,k)]);
61                 end
62             end
63         end
64     end
65 end
66 % average along Z axis
67 U=zeros(size(UP,1)/2,size(UP,2)/2,ceil(size(UP,3)/2));
68 for k=1:ceil(size(UP,3)/2);
69     for j=1:size(U2,2);
70         for i=1:size(U2,1);
71             if k==ceil(size(UP,3)/2); %k is the last one
72                 if mod(size(UP,3),2)==1 %size is odd
73                     U(i,j,k)=U2(i,j,2*k-1);
74                 else %size is even
75                     if strcmp(flow_dir, 'Z')
76                         U(i,j,k)=harmmean([U2(i,j,2*k-1) U2(i,j,2*k)]);
77                     else

```

```
78             U(i,j,k)=mean([U2(i,j,2*k-1) U2(i,j,2*k)]);
79         end
80     end
81     else %k is not the last one
82         U(i,j,k)=mean([U2(i,j,2*k-1) U2(i,j,2*k)]);
83     end
84 end
85 end
86 end
87 UP=U; %rename the array in order to rerun the iterations
88 end
```